

Study of Deformation and Fracture Behaviour of Alloy 617

By

ADITYA NARAYAN SINGH

Enrolment No.: ENGG02201404001

**Indira Gandhi Centre for Atomic Research,
Kalpakkam, Tamil Nadu 603102, India**

*A thesis submitted to the
Board of Studies in Engineering Sciences
In partial fulfillment of requirements
for the Degree of*

DOCTOR OF PHILOSOPHY

of

**HOMI BHABHA NATIONAL INSTITUTE
Mumbai, India**




August, 2017


Homi Bhabha National Institute

Recommendations of the Viva Voce Committee

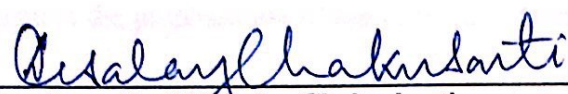
As members of the Viva Voce Committee, we certify that we have read the dissertation prepared by Aditya Narayan Singh entitled "Study of Deformation and Fracture Behaviour of Alloy 617" and recommend that it may be accepted as fulfilling the thesis requirement for the award of Degree of Doctor of Philosophy.


Chairman - Dr. K. Velusamy

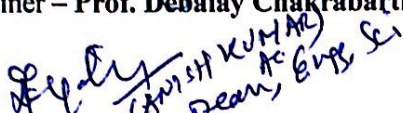
27/11/2019
Date:


Guide / Convener - Prof. Aniruddha Moitra

27. 11. 2019
Date:


Examiner - Prof. Debalay Chakrabarti

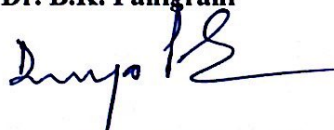
27/11/2019
Date:


Member 1- Dr. S. Saroja

27/11/2019
Date:

Member 2- Dr. B.K. Panigrahi

Date:




27/11/19

Final approval and acceptance of this thesis is contingent upon the candidate's submission of the final copies of the thesis to HBNI.

I hereby certify that I have read this thesis prepared under my direction and recommend that it may be accepted as fulfilling the thesis requirement.

Date: 27.11.2019

Place: Kalpakkam


Dr. Aniruddha Moitra
(Guide)

STATEMENT BY AUTHOR

This dissertation has been submitted in partial fulfillment of requirements for an advanced degree at Homi Bhabha National Institute (HBNI) and is deposited in the library to be made available to borrowers under the rules of the HBNI.

Brief quotations from this dissertation are allowable without special permission, provided that accurate acknowledgement of the source is made. Requests for permission for extended quotation from or reproduction of this manuscript in whole or in part may be granted by the Competent Authority of HBNI when in his or her judgment the proposed use of the material is in the interests of scholarship. In all other instances, however, permission must be obtained from the author.



(Aditya Narayan Singh)

DECLARATION

I, hereby declare that the investigation presented in the thesis entitled “Study of Deformation and Fracture Behaviour of Alloy 617” submitted to Homi Bhabha National Institute (HBNI), Mumbai, India for the award of Doctor of Philosophy in Engineering Sciences is the record of work has been carried out by me under the guidance of Prof. Dr. Aniruddha Moitra. The work is original and has not been submitted earlier as a whole or in part for a degree/diploma at this or any other Institution/University.



(ADITYA NARAYAN SINGH)

List of Publications arising from the thesis

Publications in Journals

1. “Study of aging-induced degradation of fracture resistance of Alloy 617 towards high-temperature applications”, **Aditya Narayan Singh**, A. Moitra, Pragna Bhaskar, G. Sasikala, Arup Dasgupta, A. K. Bhaduri, *Metall. Mater. Trans. A*, **2017**, 48, 3269–3278.
2. “Effect of thermal aging on microstructure, hardness, tensile and impact properties of Alloy 617”, **Aditya Narayan Singh**, A. Moitra, Pragna Bhaskar, G. Sasikala, Arup Dasgupta, A. K. Bhaduri, *Mater. Sci. Eng. A*, **2018**, 710, 47-56.
3. “A Study of Tensile Flow and Work-Hardening Behavior of Alloy 617” **Aditya Narayan Singh**, A. Moitra, Pragna Bhaskar, Arup Dasgupta, G. Sasikala, A. K. Bhaduri, *J. Mater. Eng. Perform.*, **2018**, 27, 3812–3823.

Conference Proceedings:

1. “Evolution of microstructure and its influence on mechanical properties in thermally aged Alloy 617”, **Aditya Narayan Singh**, A. Moitra, P. Bhaskar, G. Sasikala, Arup Dasgupta, A. K. Bhaduri, *EMSI Conf. Proc.*, **2017**, 25-28.

Conference Presentations:

1. “Study of Aging Induced Degradation of Fracture Resistance for Alloy 617” , **Aditya Narayan Singh**, A. Moitra, P. Bhaskar, G. Sasikala, Arup Dasgupta, A. K. Bhaduri, in Proceedings of International Conference on Metals and Materials Research (ICMR-2016), IISc, Bangalore, 20th - 22nd June, **2016**, 68-69.
2. “Effect of long term thermal exposure on microstructure evolution and mechanical properties of alloy 617”, **Aditya Narayan Singh**, A. Moitra, P. Bhaskar, G. Sasikala, Arup Dasgupta, A. K. Bhaduri, in Proceedings of International Conference on Electron Microscope Society of India (EMSI-2016), IIT (BHU), Varanasi, 02nd - 4th June, **2016**.
3. “Evolution of microstructure and its influence on mechanical properties in thermally aged Alloy 617”, **Aditya Narayan Singh**, A. Moitra, P. Bhaskar, G. Sasikala, Arup Dasgupta, A. K. Bhaduri, International Conference on Electron Microscope Society of India (EMSI-2017), IIT M, Chennai, 17th – 19th July, **2017**.

Other Publications (not included in the Thesis):

1. “Positron annihilation spectroscopy in tomorrow’s material defect studies”,
Aditya Narayan Singh, *Appl. Spectrosc. Rev.*, **2016**, *51*, 359–378.

Reports:

1. “Ageing induced degradation of fracture resistance of Alloy 617”, IGC Annual Report-**2016**, 109.
2. “Alloy 617: The Avenue of Tomorrow’s Advanced Ultra Supercritical Thermal Power Plant”, IGC Newsletter-**2018**, *116*, 15-18.

Workshop/Training

1. Bringing The Nanoworld Together (BTNT-2015) Oxford Instruments”, 2015 IIT M, Chennai, 3rd - 4th Nov, **2015**.
2. How to Write a Quality Technical Paper and Where to Publish within IEEE”, 2015, IIT M, Chennai, 20th Aug, **2015**.



(ADITYA NARAYAN SINGH)

Epigraph

". . . . from there I came

who taught me in all meanderings

to discover a way out

to reach there again..."

Dedicated to

Dr. A.P.J. Abdul Kalam, whose life changed millions of

Life on the Earth

A space for

My Bade Papa, My Parents, My Brothers, My Teachers, My Friends

&

My Wife

ACKNOWLEDGEMENTS

It would not have been possible for me to prepare my doctoral thesis without the help, guidance, and support of some wonderful people, who shaped my ideas and helped in my research during the tenure of Doctor of Philosophy.

Firstly, I would like to extend my deep sense of gratitude to my research advisor Dr. Aniruddha Moitra, who has significantly influenced my intellectual and personal growth during this great period of my life. His ideology towards research “*research is being true to yourself*” has been the ground on which I have worked in my Ph.D. duration and will be working throughout my entire span of life on the earth. He has been a tremendous source of inspiration and encouragement, and his efforts have guided me to the place where I am now. His stimulating discussions, constructive criticisms, and tutelage have put me always on my toes. My passion for fine research kindled by him would be commemorated forever in my heart.

My special thanks to the present Director IGCAR Dr. A. K. Bhaduri, for his unforgettable support during my odd times of research career in IGCAR. His exemplary decision-making ability and strong technical knowledge of the subject of my Ph.D. research topic has benefitted me on many occasions. I have been additionally benefited by having him as my co-author for my all Ph.D. papers. His trust in me and my work have motivated me to work incessantly to better my work day by day.

I extend my sincere thanks to Dr. G. Amrendra Director, MMG for giving support in my research work.

I deeply express my thanks to Dr. M. Sai Baba, former Director, RMG and Convener, Engineering Sciences Standing Committee, for providing pleasant accommodation and encouragement.

I owe my sincere thanks to Dr. G. Sasikala, former Dean, HBNI-IGCAR campus for the technical support, quick paper corrections, and for her innumerable

suggestion which made my papers stand in top international journals of metallurgy. I also extend my sincere thanks to Dr. Anish Kumar, Dean, HBNI-IGCAR campus for making this thesis possible to reach the podium of defense.

I sincerely owe my thanks to the honorable doctoral committee members Dr. K. Velusamy (Chairman), Dr. S. Saroja (Member), and Dr. B.K. Panigrahi (Member) for their gregarious suggestions and constant support.

Technical contributions from Dr. Arup Dasgupta, Pragna Bhaskar, and Dr. R. Mythili from MCG, IGCAR for TEM analysis is duly acknowledged. Due is also to Shri S. A. Krishnan and Dr. Sathyanarayanan for their technical support in my research. I take this opportunity to thank Mr. Balakrishnan, Mrs. Srividhya, Ms. Paneerselvam, and all staff of MMS section in MDTD, IGCAR.

I would sincerely place my thanks to the Department of Atomic Energy, Govt. of India, for their financial assistance. I owe my sincere thanks to Homi Bhabha National Institute for accepting this work to award the Ph.D. degree. I am also spellbound to the reviewers and examiners for their time and considerations.

Good friends are special gifts to a human being. I take this stage to say a small thanks to my very-special senior Mr. Shashwat Swain for his brotherly help and giving me moral support during my hickups in research in IGCAR. I thank my batch mates and friend, V. Shiva who helped me for all those days of my long one-month bed rest due to severe back pain. I also can't forget sharing evening tea with my batchmates Balaji, Chandan, Nagendra, Siva, Rohith, Abhilash, Manmath Kumar Dash, Sahoo, Poddar, Jagapati, Prashant, Raghvendran, Saikumaran, Anuj, and Ronit. I extend my sincere thanks to my seniors Vikas, Shivang, and Chandan for their help and support throughout my Ph.D. work. I am very much thankful to my roommate Veeru for giving me invaluable support and encouragement to pursue my Ph.D. in IGCAR.

Each word of my thesis acknowledges the undaunted support of my mother, Smt. Geeta Singh for her love and care she has shown toward a notorious person like me. Her insatiable zeal toward science has helped me explore different paths of science and technology. My father, Shree Babban Singh, has always been a source of motivation for all my good works in life. His simplicity of expressing even the most critical aspects most simply has mesmerized me at many a time. The reflection of which can be found in my thesis as well. My brothers Ashish and Anand have always been my motivation and friends of my all odd times in my life. Their shoulders were always there for me when I failed in my attempts in the journey of my life. I am indebted to the new chapter of my life, Nivedita, my wife for her support and care while writing this thesis. Her love, care, and uncomplaining nature gave me full concentration on my research.

I am also very thankful to distinguished Prof. Kwang Soo Kim, Korean National Honor Scientist and my current supervisor for his suggestions during the revision of this thesis.

Penultimate, yet importantly - how I can forget from where I came, what is that force doing all these, and what for I am delving - It is my admiration and deepest gratitude to this unbound "Nature" from whom I am learning the essence of life and its very cause. I thank the almighty for giving me such a wonderful life to live in Dr. Kalam's age. An era of the space technology revolution in India, an era that motivated the youth to explore the unexplored path and chase their dreams. He will remain a great source of inspiration to me and the entire humanity.

(Aditya Narayan Singh)

CONTENTS

| | Page No. |
|--|-------------|
| SYNOPSIS | i |
| LIST OF FIGURES | vii |
| LIST OF TABLES | xiii |
| LIST OF ABBREVIATIONS | xiii |
| LIST OF NOMENCLATURES | xv |
| | |
| CHAPTER 1 INTRODUCTION | |
| 1.1 Introduction | 1 |
| 1.2 High-temperature Thermal Power Plant: The Need of the Day | 4 |
| 1.3 Supercritical Technology/Carbon Capture Technology | 5 |
| 1.4 Material Property Required for Advanced Ultra-Supercritical Thermal Power Plants | 7 |
| 1.4.1 Required Mechanical Property | 8 |
| 1.4.2 Microstructural Property | 9 |
| 1.5 Qualification of Alloy 617 for Advanced Ultra-Supercritical Thermal power plants | 9 |
| 1.5.1 Developing Advanced Ultra-Supercritical Thermal Power Plants Technology Indigenously – A Necessity | 11 |
| 1.5.2 Alloy 617: The backbone of Indian Advanced Ultra-Super Critical Thermal Power Plants Programme | 11 |
| 1.6 The Scope of Advanced Ultra-Supercritical Thermal Power Plants and Clean Coal Technologies in India | 12 |
| 1.7 Objective and Scope of the Present Thesis Work | 12 |
| | |
| CHAPTER 2 Literature Survey on Microstructure, Fracture, and Deformation Properties of Alloy 617 | |
| 2.1 Introduction | 14 |

| | | |
|---|--|----|
| 2.2 | Need for the Present Study | 22 |
| CHAPTER 3 Experimental Techniques to Evaluate the Microstructure, Fracture and Deformation Properties of Alloy 617 | | |
| 3.1 | Introduction | 24 |
| 3.2 | Materials Selection, Properties, and Their Composition | |
| 3.2.1 | Alloy 617 | 25 |
| 3.2.2 | Chemical composition of Alloy 617 | 26 |
| 3.3 | Methods of Specimen Preparation for Different Studies | 27 |
| 3.4 | Grain Boundary Characterization Using Light Microscope | 30 |
| 3.5 | Structural and Morphological Characterization | 31 |
| 3.5.1 | Scanning and Transmission Electron Microscopy | 32 |
| 3.5.1.1 | Scanning Electron Microscopy/Energy Dispersive X-Ray Spectroscopy | 33 |
| 3.5.1.2 | Transmission Electron Microscope (TEM) | 35 |
| 3.6 | Mechanical Characterization | |
| 3.6.1 | Vickers Hardness Testing | 37 |
| 3.6.2 | Tensile Testing Machine | 39 |
| 3.6.3 | Charpy Impact Testing Machine | 41 |
| 3.6.4 | Instrumented Drop Weight Testing Machine | 42 |
| 3.7 | Summary | 43 |
| CHAPTER 4 Study of Microstructural Evolution for As-received and Aged Alloy 617 | | |
| 4.1 | Introduction | 44 |
| 4.2 | Optical Metallographic Studies of As-received and Aged Alloys | 45 |
| 4.3 | Morphological Characterization of Alloy 617 for High-temperature Application | 52 |

| | | |
|-----|---|----|
| 4.4 | Quantifying the Precipitates of Alloy 617 | 57 |
| 4.5 | TEM Study of As-received and Aged Alloy 617 | 58 |
| 4.6 | Summary | 68 |

CHAPTER 5 Study of Tensile Deformation Behaviour of As-received and Aged Alloy 617

| | | |
|---------|---|----|
| 5.1 | Introduction | 70 |
| 5.2 | Hardness of As-received and Aged Alloy 617 | 71 |
| 5.3 | Tensile Properties of As received and Aged Alloy 617 | 73 |
| 5.4 | Work Hardening Analysis of the As-Received and Aged Alloy 617 | |
| 5.4.1 | Analytical Framework for Work Hardening Analysis | 79 |
| 5.4.2 | Flow Relationships of Alloy 617 | 82 |
| 5.4.2.1 | Variations of Work Hardening Parameter with Aging Durations | 85 |
| 5.4.2.2 | Variations of instantaneous work hardening rate with stress and aging duration | 88 |
| 5.4.3 | The fundamental interplay of precipitate-matrix interface and its influence on work hardening | 91 |
| 5.5 | Insights into the deformation mechanism | 92 |
| 5.6 | Summary | 96 |

CHAPTER 6 Study of Fracture Resistance of As-received and Aged Alloy 617

| | | |
|-----|---|-----|
| 6.1 | Introduction | 98 |
| 6.2 | Materials and Methodology | 99 |
| 6.3 | Results from Charpy Impact Testing | 100 |
| 6.4 | Fractography of Charpy tested specimens | 102 |
| 6.5 | Peering Fracture Through the Shear Lip Formations | 108 |

| | | |
|-------------------|---|-----|
| 6.6 | Nature and Compositional Morphology of Precipitates on Fracture Surface | 110 |
| 6.7 | Estimation of J -R curve from Charpy V-notch Impact energy | |
| 6.7.1 | Introduction | 118 |
| 6.7.2 | Experimental Procedure | 118 |
| 6.7.3 | Methodology for Estimation of J -R curve from Charpy V-notch Impact energy | 119 |
| 6.7.4 | Interpretation of J -R curve | 122 |
| 6.7.5 | Validation of J -R curve from instrumented Charpy System | 124 |
| 6.8 | Summary | 126 |
| CHAPTER 7 | Brief Summary of Thesis and Scope for Future Work | |
| 7.1 | Introduction | 129 |
| 7.2 | Scope for Future Work | 132 |
| REFERENCES | | |

SYNOPSIS

Foreword

Alloy 617 is one of the candidate materials for high-temperature applications owing to its high-temperature strength, reasonable microstructural stability, corrosion, and oxidation resistance. However, the anticipated microstructural evolution during its exposure at a higher temperature for longer durations is still a matter of concern for the designers as the microstructure of this alloy strongly influences its deformation characteristics and fracture resistance. The availability of deformation and fracture resistance data on Alloy 617 especially after high-temperature aging is scanty in literature. Thus, this thesis work is undertaken in the hope of gaining some information as to the nature of the Alloy 617 and has been aimed to fill up some gaps in this arena towards ensuring component integrity in the high-temperature domain.

Chapter 1: Introduction:

Chapter 1 provides a brief outline of the current high-temperature trending materials, including its pros and cons, mechanical properties, the significance of high-temperature stability leading to the greater applicability, and acceptability of the alloys over other contemporary alloys. The present status and developments in understanding the microstructural evolution for different aging conditions and their applications are also introduced along with the discussions of solid solution strengthening allied with contribution offered by the precipitation hardening is also briefed. The possibilities of strengthening by carbide precipitates are given a shade of light. The effect of microstructure on mechanical properties viz: Charpy, hardness, and tensile are also given adequate space.

Chapter 2: Literature Survey on Microstructure, Fracture, and Deformation properties of Alloy 617:

This chapter introduces the developmental aspects of materials for high-temperature applications to curb global greenhouse emission and global warming. This chapter will also throw light on global warming and the urgency to upgrade thermal power plants to next-generation power plants. Description of the existing high-temperature material and transition from current to advanced ultra-supercritical thermal power plants technology with the emphasis on Ni-based superalloy is included. An overview of the material selected for high-temperature applications in advanced ultra-supercritical thermal power plant technology has also been presented. This chapter also reviews the material properties for high-temperature applications. A series of literature surveys from the past to up to date published literature on Alloy 617 material and their enabling features for applications are also covered in this chapter. A detailed survey of Ni-based superalloy has also given adequate space. In this chapter, initially, the issues about the microstructural stability of other high-temperature materials have been discussed. The detailed published literature in this direction has been studied and the salient features are highlighted in the thesis. Extensive literature data in the direction correlating the microstructural changes with the creep, fatigue or creep crack growth during aging at high-temperatures, often pointing to severe deterioration as compared to the as-received material can be found, and is well documented in the thesis as well. However, the literature data on the aging-induced microstructural changes leading to fracture of this alloy is scanty. Guo *et al.* have reported a significant drop in fracture resistance even after a short aging treatment of 300 hours at 1033 K (760 °C). A similar observation has been reported by Nanstad *et al.*, where a 36 % degradation of fracture energy was observed just after 200 hours of aging at 1023 K (750 °C). Though the results have been attributed to the coarsening and redistribution of the precipitates, an unequivocal conclusion correlating the microstructural evolution and fracture resistance degradation is yet to be evolved. These results indicate that there is an urgent need to

evaluate the extent of degradation of fracture resistance due to the coarsening of γ' and also in terms of the aging-induced microstructural evolution of the Alloy 617 after a long-time aging treatment at high-temperature.

Chapter 3: Experimental Techniques to Evaluate the Microstructure, Fracture, and Deformation properties of Alloy 617:

This chapter describes in detail the experimental techniques to characterize the Alloy 617. The major tools and techniques used for the thesis towards preliminary as well as advanced characterization required for morphological, structural, and elemental analysis of the material have been discussed. For the as-received alloy, the samples were mechanically polished to mirror finish and then etched with a solution of Aqua-regia (3HCL:1HNO₃). For aged specimens, following the mechanical polishing, the samples were electro-etched with an optimized solution mixture of 60 % HNO₃ and 40 % H₂O, at room temperature, using 1.5 V for etching times varying from 5 to 120 seconds. Grain sizes and their distribution have been studied with Leica software. The fractographic analysis of the failed specimen has been carried out by scanning electron microscopy. The sub-microscopic structure like fine precipitates; their morphology, and distributions have been studied extensively using the transmission electron microscope and is well documented in the thesis.

Chapter 4: Study of Microstructural Evolution in As-received and Aged Alloy 617:

A detailed microstructural characterization of Alloy 617 has been accomplished both in as-received and aged condition. The overall grain size distribution during the entire aging duration remains almost constant. Though a slight shift in frequency distribution is distinctly seen to occur during 10000 - 20000 hours but this seems to be a marginal shift. The grain boundary serrations are seen to disappear during the aging. The duplex nature of grain size distribution has also been less prominent in the aged material. The prominent feature of this alloy is its propensity to release precipitates

even for the aging duration of 1000 hours. The aging-induced precipitates can be categorized into two major types namely $M_{23}C_6$ and γ' , i.e. $Ni_3(Ti, Al)$ with traces of Ni_3Si . Further, where the γ' has been precipitated randomly (within the grain and also in the boundaries), the $M_{23}C_6$ has been precipitated mainly in the grain boundaries. Titanium carbonitrides $Ti(C, N)$ precipitates are mainly seen inside the grains. TEM investigation of this material has brought out significant information regarding aging-induced microstructural changes in the material. As-received material shows only Mo-rich and Cr-rich precipitates and no sign of γ' phase. Aging caused an evolution of γ' precipitates but with morphology rarely changed over the entire span of aging. Though a slight coarsening can be seen over periods of aging, this change is insignificant.

Chapter 5: Study of Tensile Deformation Behaviour of As-received and Aged Alloy 617:

This chapter brings forth a detailed study of the effect of thermal aging on the hardness, tensile, and work hardening behaviour of Alloy 617 and their correlation with microstructure. Thermal aging of Alloy 617 is accompanied by precipitation of γ' precipitates, which strongly influences the hardness and tensile properties of this alloy after different aging durations. The anomalous decrease in yield stress between 5000- and 10000-hours aging duration is attributed to the ease of dislocation movement in this regime owing to the combined effect of coarsening of γ' precipitates and the rise in stacking fault energy. The absence of annealing twins in the aged specimens indicates toward an aging-induced increase of stacking fault energy. Alloy 617 exhibits three distinct stages of work hardening in the plot of θ vs. σ for all the four heat treated conditions. 1) An initial transient stage (TS), where θ decreases rapidly 2) the stage II where either θ marginally rises or remains constant, and 3) stage III where θ gradually decreases. The stage II work hardening rate increases till 5000 hours aging condition and then drops suddenly till 10000 hours and a marginal increase till 20000 hours. This

behaviour in work hardening rate observed at different aging durations is ascribed to spontaneous evolution of fine γ' ($\text{Ni}_3(\text{Ti, Al})$) precipitates in the matrix during 5000- and 10000-hours aging treatments.

Chapter 6: Study of Fracture Resistance of Aged Alloy 617:

The analysis of our experimental results confirm that the impact energy of this alloy has been severely degraded due to aging. The fractographic observations also reveal a change of fracture mode from predominantly ductile nature to predominantly intergranular cracking as the aging time increases from 1000 to 20000 hours. It is well known that the impact energy at room temperature of any material, as determined by conventional Charpy test, consists of two components: (a) energy required for crack initiation and (b) energy required for crack propagation. The inherent microstructural features significantly influence both of these components to fracture energy. Where the crack initiation energy is generally affected by nature, size, and shape of the precipitates which are being evolved during the aging at high-temperature for this material, the crack propagations energy are often controlled by the grain size distribution and the grain boundary strength. Additionally, the strength of the matrix often plays a crucial role, as it is generally argued that a stronger matrix keeps a propagating crack sharper, thus demanding less energy to propagate. The inverse behavior of strength and toughness in conventional structural materials corroborates with this idea. Further, where the γ' has been precipitated randomly (within the grain and also in boundaries), the M_{23}C_6 has been precipitated mainly in the grain boundaries. From these observations, this can be argued that the γ' is basically contributing to increasing the strength of the matrix, which in turn is leading to the lower fracture energy of the material by making the crack propagation process easier. Contrary to this, the role of M_{23}C_6 is more towards the crack initiation energy. It is well established that the crystal structure of the M_{23}C_6 is different from that of the FCC matrix of Alloy 617.

So these precipitates will act as a barrier to the dislocation motion, which is a precursor for any crack initiation process. Further, the effect of these carbides on crack initiation would be enhanced as they became coarser during aging and their preferential segregation to the grain boundaries. This, in turn, has made the grain boundary an easy source of crack initiation and, thus, promoting the intergranular fracture in this material.

Dynamic J -R curves for as received and different aging conditions have been inferred from the Charpy energy using an analytical-empirical approach, as available in the literature. The J -R curve of Alloy 617 shows a drastic decrease after the aging time of 1000 hours. Further aging durations result in a progressive decrease of J -R curve but to a much smaller degree. Valid crack initiation J values have been obtained for both as-received and in all aged conditions of Alloy 617. They show the same trend as the J -R curve. A substantial section on the validation of the J -R curves from instrumented Charpy impact testing system using load-displacement curve is also given due space.

Chapter 7: Brief Summary and Conclusions from the Thesis and Scope of Future Work:

This chapter summarizes the major findings from this entire thesis work. These mainly cover the effect of microstructural variations on the deformation and fracture resistance of Alloy 617 during its exposures at high-temperature for longer duration. This chapter also outlines the existing gap areas filled with the findings of thesis and the also present a road map for the future work.

LIST OF FIGURES

| Figure No. | Title of the Figure | Page No. |
|------------|--|----------|
| 1.1 | Scenario of global Greenhouse Gas Emissions. | 3 |
| 1.2 | World scenario of coal reservoirs. | 3 |
| 1.3 | Energy profile of various countries from 2010-2035. | 4 |
| 1.4 | Indicative CO ₂ emission reduction pathways. | 5 |
| 1.5 | Progress in various stages of thermal power plants. | 7 |
| 1.6 | Schematics of header used in thermal power plants. | 7 |
| 2.1 | Time-temperature-transformation (TTT) diagram for long term aging of Alloy 617. | 21 |
| 3.1 | Schematic representations of Alloy 617 tubes in as-received condition with notch orientation of the Charpy-V notch specimens used. | 26 |
| 3.2 | Important elements in the make-up of Ni-based alloys. | 27 |
| 3.3 | Schematic representation of miniaturized flat tensile specimen (dimensions in mm). | 28 |
| 3.4 | The standard V-notch Charpy specimen in compliance with ASTM E-23 standards (All dimensions are in mm). | 28 |
| 3.5 | Advanced TEM sample preparation facility at MMG, IGCAR. | 30 |
| 3.6 | Actual image of light microscope facility at MMG, IGCAR. | 30 |
| 3.7 | (a) Schematic representation of the several interactions occurs in a material due to the incidence of high energy electron beam; (b) Block diagram of a FESEM showing the major components of the system. | 33 |
| 3.8 | The highly simplified working diagram showing two basic operations of the TEM imaging system involving diffraction mode where the DP was projected onto the viewing screen (left side), and image mode where the images were projected onto the viewing screen (right side). | 36 |
| 3.9 | The actual mage of TEM facility at MMG, IGCAR. | 37 |
| 3.10 | Hardness measurement facility in IGCAR. | 39 |
| 3.11 | Tensile test facility at IGCAR. | 40 |
| 3.12 | Charpy Impact toughness facility at IGCAR. | 41 |
| 3.13 | Instrumented Charpy accelerated drop weight testing facility at IGCAR. | 43 |
| 4.1 | Schematic diagram of grain boundaries in polycrystals showing different orientation of the adjacent grains along with the triple point boundaries. | 46 |
| 4.2 | Microstructure of Alloy 617 obtained at 100X: (a) as-received alloy; (b) Frequency distribution of grain size in Alloy 617 vs ASTM number for as-received alloy. | 47 |

| Figure No. | Title of the Figure | Page No. |
|-------------------|---|-----------------|
| 4.3 | Microstructure of Alloy 617 obtained at 100X for specimens aged at 1023 K (750 °C): (a) 1000 h; (b) Frequency distribution of grain size in Alloy 617 vs ASTM number for 1000 h aged alloy. | 48 |
| 4.4 | Microstructure of Alloy 617 obtained at 100X for specimens aged at 1023 K (750 °C): (a) 5000 h; (b) Frequency distribution of grain size in Alloy 617 vs ASTM number for 5000 h aged alloy. | 49 |
| 4.5 | Microstructure of Alloy 617 obtained at 100X for specimens aged at 1023 K (750 °C). (a) 10000 h; (b) Frequency distribution of grain size in Alloy 617 vs ASTM number for 10000 h aged alloy. | 49 |
| 4.6 | Microstructure of Alloy 617 obtained at 100X for specimens aged at 1023 K (750 °C). (a) 20000 h; (b) Frequency distribution of grain size in Alloy 617 vs ASTM number for 20000 h aged alloy. | 50 |
| 4.7 | Comparing the frequency distribution of different aged specimens vs. ASTM grain size number. | 51 |
| 4.8 | SEM images unveiling the effect of aging duration on precipitate evolution in Alloy 617: (a) SEM micrograph of as-received alloy; (b) the EDS results of A point in (a); the EDS results of B point in (a). | 53 |
| 4.9 | SEM images unveiling the effect of aging duration on precipitate evolution in Alloy 617: (a) SEM micrograph of 1000 h aged alloy; (b) the EDS spectrum corresponding to Cr ₂₃ C ₆ . | 54 |
| 4.10 | SEM images unveiling the effect of aging duration on precipitate evolution in Alloy 617: (a) SEM micrograph of 5000 h aged alloy; (b) the EDS spectrum corresponding to Ti(C, N). | 55 |
| 4.11 | SEM images unveiling the effect of aging duration on precipitate evolution in Alloy 617: (a) SEM micrograph of 10000 h aged alloy; (b) the EDS spectrum corresponding to Cr ₂₃ C ₆ . | 56 |
| 4.12 | SEM images unveiling the effect of aging duration on precipitate evolution in Alloy 617: (a) SEM micrograph of 20000 h aged alloy; (b) the EDS spectrum corresponding to Cr ₂₃ C ₆ . | 57 |
| 4.13 | (a) Bright-field TEM image of as-received Alloy 617 showing M ₂ C carbide in Alloy 617 (b) SAED pattern correspond to M ₂ C type (zone axis [432]); (c) The corresponding EDS spectrum confirms Mo and Ti rich precipitates. | 59 |
| 4.14 | (a) Bright-field TEM image of as-received Alloy 617 showing M ₂₃ C ₆ carbides (b) SAED pattern correspond to M ₂₃ C ₆ type (zone axis [011]); (c) The corresponding EDS spectrum confirms M ₂₃ C ₆ type to be rich in (Cr, Mo) ₂₃ C ₆ . | 60 |

| Figure No. | Title of the Figure | Page No. |
|------------|---|----------|
| 4.15 | Bright-field TEM images and SAED pattern of γ' precipitate in Alloy 617 aged at 1023 K: (a) TEM image after 1000 h of aging showing spherical precipitates of γ' phase commonly known as $\text{Ni}_3(\text{Ti, Al})$; (b) SAED pattern correspond to γ' phase (zone axis $[0\ 1\ 1]$); (c) The corresponding EDS spectrum confirms γ' phase to be rich in Ni, Ti, Al, and they correspond to $\text{Ni}_3(\text{Ti, Al})$. | 61 |
| 4.16 | Bright-field TEM images and SAED pattern of Coherent γ' precipitate and M_{23}C_6 in Alloy 617 aged at 1023 K: (a) TEM image after 5000 h of aging showing spherical precipitates of γ' phase commonly known as $\text{Ni}_3(\text{Ti, Al})$ and M_{23}C_6 ; (b) SAED pattern correspond to γ' phase (zone axis $[0\ 1\ 1]$); (c) The corresponding EDS spectrum confirms γ' phase to be rich in Ni, Al, and Ti and they correspond to $\text{Ni}_3(\text{Ti, Al})$ and M_{23}C_6 to be rich in Cr, Mo and they correspond to $(\text{Cr, Mo})_{23}\text{C}_6$. | 62 |
| 4.17 | Bright-field TEM images and SAED pattern of γ' precipitate in Alloy 617 aged at 1023 K: (a) TEM image after 10000 h of aging showing spherical precipitates of γ' ; (b) SAED pattern correspond to γ' phase (zone axis $[0\ 1\ 1]$); (c) The corresponding EDS spectrum confirms γ' phase to be rich in Ni, Al, and Ti and they correspond to $\text{Ni}_3(\text{Ti, Al})$. | 63 |
| 4.18 | Bright-field TEM image and SAED pattern of Alloy 617 aged at 1023 K for 10000 h: (a) Bright field TEM image showing precipitates of size 80-100 nm (b) SAED pattern confirming that they correspond to M_{23}C_6 ; (c) The corresponding EDS spectrum confirms M_{23}C_6 to be rich in Cr, Mo and they corresponds to $(\text{Cr, Mo})_{23}\text{C}_6$. | 64 |
| 4.19 | Bright-field TEM image and SAED pattern of Alloy 617 aged at 1023 K for 10000 h: (a) Bright field TEM image showing precipitates of size ~ 110 -120 nm (b) Corresponding SAED pattern (c) The corresponding EDS spectrum confirms precipitates to be rich in Ni and Si and they correspond to $\text{Ni}_3(\text{Si})$. | 66 |
| 4.20 | (a) Bright-field image of alloy 617 aged for 20000 h showing $\text{Ni}_3(\text{Ti, Al})$ and M_{23}C_6 precipitates in a gamma matrix. (b) SADP for matrix, $\text{Ni}_3(\text{Ti, Al})$ and M_{23}C_6 along the zone axis $[013]$; (c) EDS spectra indicate $\text{Ni}_3(\text{Ti, Al})$; (d) EDS spectra indicate Cr rich M_{23}C_6 . | 67 |
| 4.21 | (a) Bright-field image of alloy 617 aged for 20000 h showing unidentified finer precipitates; (b) EDS spectrum indicating they are Mo-rich phase. | 68 |
| 5.1 | Profile of Hardness of the Alloy 617 with aging time. | 73 |

| Figure No. | Title of the Figure | Page No. |
|------------|--|----------|
| 5.2 | Schematic representation of miniaturized tensile specimen (dimensions in mm). | 73 |
| 5.3 | Tensile curves for Alloy 617 (a) Showing the variations in Engineering Stress-Strain curve for different aged conditions (b) True Stress-Strain plot from yield point (YP) to ultimate tensile strength (UTS) for different conditions of aging duration. | 74 |
| 5.4 | (a) Variation of yield strength with aging duration; (b) Variation of % of elongation with aging durations. | 75 |
| 5.5 | (a) TEM image after 1000 h of aging showing spherical precipitates of γ' phase commonly known as $\text{Ni}_3(\text{Ti, Al})$; (b) corresponding SAED pattern for γ' precipitates; (c) The corresponding EDS spectrum confirms γ' phase to be rich in Ni, Ti, Al, and they correspond to $\text{Ni}_3(\text{Ti, Al})$. | 77 |
| 5.6 | True stress (σ)–true plastic strain (ϵ_p) for Alloy 617 at strain rate of $3 \times 10^{-3} \text{ s}^{-1}$ for different aged conditions are superimposed. | 81 |
| 5.7 | Best fit for different flow relationships true stress (σ)–true plastic strain (ϵ_p) for Alloy 617 at strain rate of $3 \times 10^{-3} \text{ s}^{-1}$ for different aged conditions at 1023 K ; (a) as-received; (b) 1000 h; (c) 5000 h; (d) 10000 h; (e) 20000 h. | 84 |
| 5.8 | Variation of Ludwigson equation parameters (a) K_1 ; (b) K_2 ; (c) n_1 ; (d) n_2 with aging treatment of Alloy 617. | 86 |
| 5.9 | Variation of Swift equation parameters (a) K_s (b) x_0 and (c) n_s with aging treatment of Alloy 617. | 87 |
| 5.10 | Variation of Ludwik equation parameters (a) K_{l1} ; (b) K_L ; and (c) n_l with aging treatment of Alloy 617. | 88 |
| 5.11 | Variations of instantaneous work hardening rate θ vs σ for different aged conditions for Alloy 617; (a) as-received; (b) 1000h; (c) 5000 h; (d) 10000 h; (e) 20000 h; (f) Combined plot of θ vs σ for all aged samples. | 89 |
| 5.12 | Variations of instantaneous work hardening rate $\theta \times (\sigma - \sigma_y) \times 10^6$ vs. $(\sigma - \sigma_y)$ for different aged conditions for Alloy 617. | 91 |
| 5.13 | Deformed micrographs of the Alloy 617 in aging conditions for 1000 and 20000 h at strain rate of $3 \times 10^{-3} \text{ s}^{-1}$. (a) The presence of sufficient amounts of fibrous dimples is a major characteristic of ductile deformation mechanism; (b) extensive amounts of slip bands in 20000 h aged sample is an indication that the this material has a strong tendency for the planar slip and do not favor the cross slip tendency; (c) TEM image shows the presence of nano-twins as formed in 1000 h aged sample; (d) TEM images of 20000 h deformed samples clearly shows extensive precipitations. These extensive precipitations and grain deformations explains the enhanced capability of extended tensile elongation in this material. | 95 |

| Figure No. | Title of the Figure | Page No. |
|-------------------|---|-----------------|
| 5.14 | The elemental mapping of the fractured tensile samples. (a) The EDS spectrum of 1000 h indicates that precipitates are rich in Cr and minimal in Mo-rich; (b) The elemental mapping of 20000 hours tensile tested sample indicates that there has been substantial rise in the Cr and Mo-rich phase in the precipitates. The intense peaks of Cr and Mo in (b) is an indication that these elements are widely distributed in the matrix. | 96 |
| 6.1 | Schematic representation of a Charpy impact specimen with given dimensions in mm. | 100 |
| 6.2 | Effects of thermal aging on the variation of Charpy impact energy for the Alloy 617. (a) Charpy energy profile of alloy 617 aged at various conditions; (b) % Charpy energy of the aged conditions. | 101 |
| 6.3 | SEM fractographs of failed as-received Alloys 617 during Charpy impact test (a) Near to notch tip; (b) Middle of the specimen; (c) Far end of notch tip. | 103 |
| 6.4 | SEM fractographs of failed specimen unveiling the effect of aging duration on Charpy impact test for the sample aged at 1023 K for 1000 h (a) Near to notch tip; (b) Middle of the specimen; (c) Far end of notch tip. | 103 |
| 6.5 | SEM fractographs of failed specimen unveiling the effect of aging duration on Charpy impact test for the sample aged at 1023 K for 5000 h (a) Near to notch tip; (b) Middle of the specimen; (c) Far end of notch tip. | 104 |
| 6.6 | SEM fractographs of failed specimen unveiling the effect of aging duration on Charpy impact test for the sample aged at 1023 K for 10000 h; (a) Near to notch tip (b) Middle of the specimen; (c) Far end of notch tip. | 105 |
| 6.7 | SEM fractographs of failed specimen unveiling the effect of aging duration on Charpy impact test for the sample aged at 1023 K for 20000 h (a) Near to notch tip; (b) Middle of the specimen; (c) Far end of notch tip. | 106 |
| 6.8 | Graphical representation of % fibrous vs. various aging durations in Alloy 617. Area (μm^2) shown in the graph is a pictorial representation of the data obtained from table 6.1. | 108 |
| 6.9 | Shear-lip formation observed during various Charpy tested specimens of Alloy 617: (a) As-received; (b) 1000 h; (c) 5000 h; (d) 10000 h; (e) 20000 h; (f) the arrow indicates direction of crack propagation and dashed area represents the formation of shear lip. | 110 |
| 6.10 | (a) SEM image of as-received alloy; (b-f) SEM 2D element maps of the elements extracted from EDX spectra. | 111 |
| 6.11 | (a) SEM image of 1000 hours aged alloy; (b-d) SEM 2D element maps of the elements extracted from EDX spectra. | 112 |

| Figure No. | Title of the Figure | Page No. |
|-------------------|---|-----------------|
| 6.12 | (a) SEM image of 5000 hours aged alloy; (b-f) SEM 2D element maps of the elements extracted from EDX spectra. | 113 |
| 6.13 | (a) SEM image of 10000 hours aged alloy; (b-f) SEM 2D element maps of the elements extracted from EDX spectra. | 115 |
| 6.14 | (a) SEM image of 20000 hours aged alloy; (b-f) SEM 2D element maps of the elements extracted from EDX spectra. | 116 |
| 6.15 | <i>J</i> -R curves for as-received and aged conditions of Alloy 617. | 123 |
| 6.16 | Load-displacement curves for as-received and aged condition of Alloy 617 obtained from instrumented Charpy impact testing system. | 124 |
| 6.17 | <i>J</i> -R curves for as-received and aged condition of Alloy 617 obtained from instrumented Charpy impact testing system. | 126 |

LIST OF TABLES

| Table No. | Title of the Table | Page No. |
|------------------|--|-----------------|
| 3.1 | The chemical composition (Wt. %) of Alloy 617 employed in this study. | 27 |
| 4.1 | Quantified precipitates of the indigenous Alloy 617 in the different heat-treated conditions. | 58 |
| 4.2 | Local (wt pct) composition variation of elements in the matrix and around $M_{23}C_6$ (10000 hour aged). | 65 |
| 5.1 | Tensile properties of the indigenous Alloy 617 in the different heat-treated conditions tested at ambient temperature. | 74 |
| 5.2 | Values of χ^2 for different flow relationships fitted for the different heat-treated conditions tested at ambient temperature. (All the values have been round off to one decimal place). | 82 |
| 6.1 | Area considered for the energy from impact tests of as-received and aged conditions of Alloy 617. | 107 |
| 6.2 | Charpy energy from impact tests of as-received and aged conditions of Alloy 617. | 119 |
| 6.3 | KV, Ag, Δa_m , UTS, and crack initiation J values for as-received and aged conditions of Alloy 617. | 123 |
| 6.4 | Results of instrumented testing system for Alloy 617 in its as-received and aged conditions. | 125 |

LIST OF ABBREVIATIONS

| | |
|-------|--|
| ASTM: | American Society for Testing and Materials |
| BSE: | Back Scattered Electron |
| CCD: | Charge Coupled Device |
| cm: | centimeter |
| CRT: | Cathode Ray Tube |
| CTOA: | Crack Tip Opening Angle |
| CTOD: | Crack Tip Opening Displacement |
| CVN: | Charpy V-notch |
| DPH: | Diamond Pyramid Hardness |

| | |
|-----------|--|
| DPs: | Diffraction Pattern |
| EDAX/EDS: | Energy Dispersive Analysis of X-ray/Energy Dispersive Spectroscopy |
| El: | Elongation |
| FCC: | Face Centered Cubic |
| FEM: | Finite Element Method |
| FETEM: | Field-Emission Transmission Electron Microscope |
| GB: | Grain boundary |
| HEDE: | Hydrogen Enhanced Decohesion |
| HELE: | High Efficiency Low Emission |
| HELP: | Hydrogen Enhanced Localized Plasticity |
| HRTEM: | High-Resolution Transmission Electron Microscope |
| HTC: | High-Temperature Corrosion |
| HV: | Vickers hardness |
| J: | Joules |
| keV.: | Kilo electron volt |
| L–M: | Levenberg–Marquardt |
| LM: | Light Microscope |
| mm: | millimeter |
| nm: | Nanometer |
| SAED: | Selected Area Electron Diffraction |
| SEM: | Scanning Electron Microscope |
| SFE: | Stacking Fault Energy |
| STEM: | Scanning Transmission Electron Microscope |
| TEM: | Transmission Electron Microscopy |
| TS: | Transient Stage |
| UTM: | Universal Testing Machine |

UTS: Ultimate Tensile Strength

YS: Yield Stress

LIST OF NOMENCLATURES

J J-integral

R Elastic-plastic crack growth resistance

Δa Crack extension

Δa_m Crack extension at maximum load

C and p Material dependent constant

a_0 Initial crack length

B specimen thickness

W specimen width

b_o ligament length

W_t Total fracture energy

W_{mp} Plastic part of W_m

A_g Uniform fracture strain

KV Charpy fracture energy

R_m Ultimate tensile strength

J_0 J_0 is obtained by the intersection of the linear extrapolation of the J - R curve from the range $\Delta a > \Delta a_m$ to the intersection with the blunting line

$J_{0.2}$ J at $\Delta a=0.2$

$J_{0.2t}$ J at a distance of 0.2 mm from the intersection with the blunting line

1

Introduction

This chapter introduces the material prospects for advanced ultra-supercritical thermal power plants programme in India, towards meeting the spiraling energy demand in the country. The advantage of using advanced ultra-supercritical thermal power plant is to scale up their energy conversion efficiency and reduce intimidating global warming by reducing CO₂ emissions. A complete overview of the inception of advanced ultra-supercritical thermal power plants programme across the globe and selection of Alloy 617 as the candidate material for the high-temperature component is discussed in detail. Various stages of plant operating temperature and the challenges involved in the development of materials for high-temperature applications are briefly outlined. The primary focus of this chapter is on identifying the candidate material for the successful operation of the advanced high-temperature thermal power plants.

1.1 Introduction

OVER the past several decades, fossil fuels, and particularly coal, have enjoyed a major share in the growing economy and is primarily the nerves and veins of the energy demand. As coal is a widely dispersed and relatively low-cost energy resource, it is used exhaustively around the world: at present, almost two-thirds of coal demand in the energy sector is for electricity generation. But the growing reliance on coal to meet the rising demand for energy presents a major threat to a low-carbon future [1]. Since the inception of coal-fired power plants, they are continually weaving the fabrics of global warming by emitting greenhouse gases to the environment. A recent scenario of the extents of greenhouse gas emission from different sources, as estimated by the United

States of America [1], is given in Fig. 1.1. In this era of the 21st century, where the development status of the nation is determined by the human development index (HDI), which is indeed a measure of per capita energy consumption, the world thrives for more and more electrical energy consumption. It is natural that the coal-fired power plants are under immense pressure to increase energy conversion efficiency and scale down their greenhouse gas emissions to address the growing international concern against global warming. The challenge to meet the energy needs, which is well set to double up over approaching few decades [2] coupled with the concern of dwindling coal reservoirs across the globe (Fig. 1.2), places the development of high-temperature performance materials at the forefront of materials research. As per the philosophy of obtaining high efficiency [3, 4] from thermal power plants, the maximum temperature should be as high as possible, and rejection temperature should be as low as possible. This requisite drives modern research toward developing superalloys for energy systems and sub-systems to be satisfactorily operable at a very high steam temperature and pressure. As the power plant efficiency and reduction in greenhouse gases like carbon (CO₂) emissions are directly related to plant operating temperature, very high-temperature thermal and the power plant is the need of the hour.

The benefit that coal-fired thermal power plants attain in terms of its high efficiency with increasing pressure and temperature is soon poised due to decreasing creep strength and thermal expansion at high-temperature, whereas the increased pressure causes leakage of fluid flows and deformation of structures. As a result, accomplishing a high-temperature and high-pressure steam cycle requires significant breakthroughs regarding the material- and mechanical-design technology.

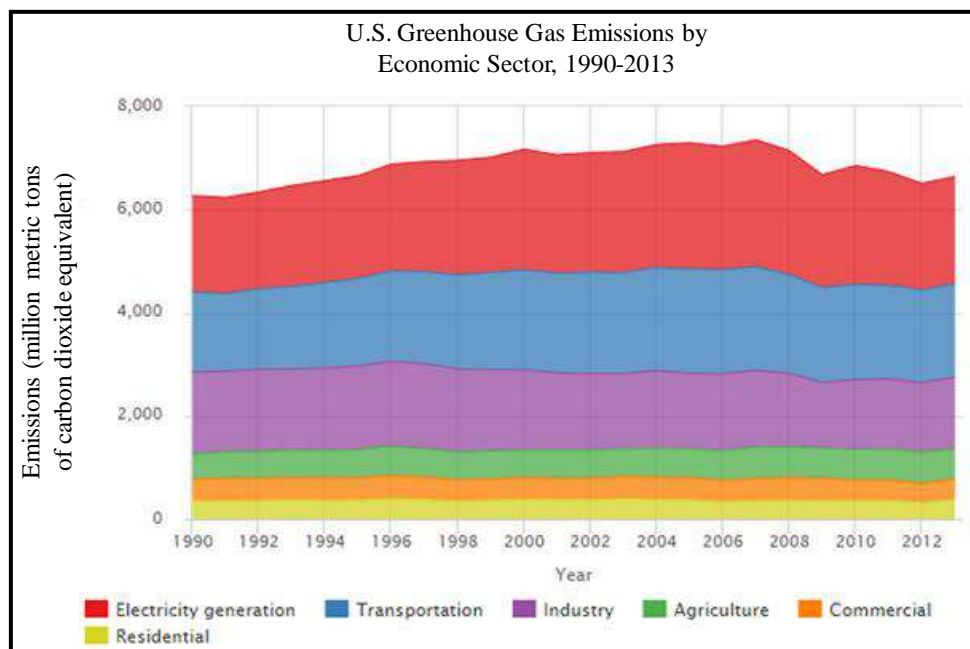


Fig. 1.1 — Scenario of global Greenhouse Gas Emissions (Source: Photo: U.S. EPA's Inventory of U.S. Greenhouse Gas Emissions and Sinks: 1990–2013).

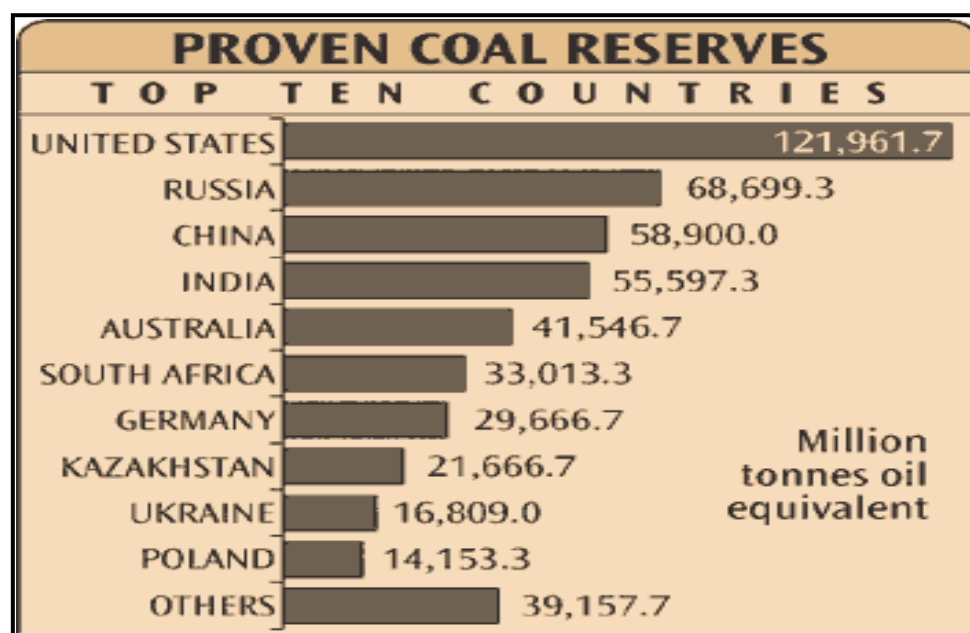


Fig. 1.2 — World scenario of Coal reservoirs (Source: <http://earthtrends.wri.org>).

As per the World energy outlook released on 12th November 2012, the global energy demand for various countries is represented in Fig. 1.3.

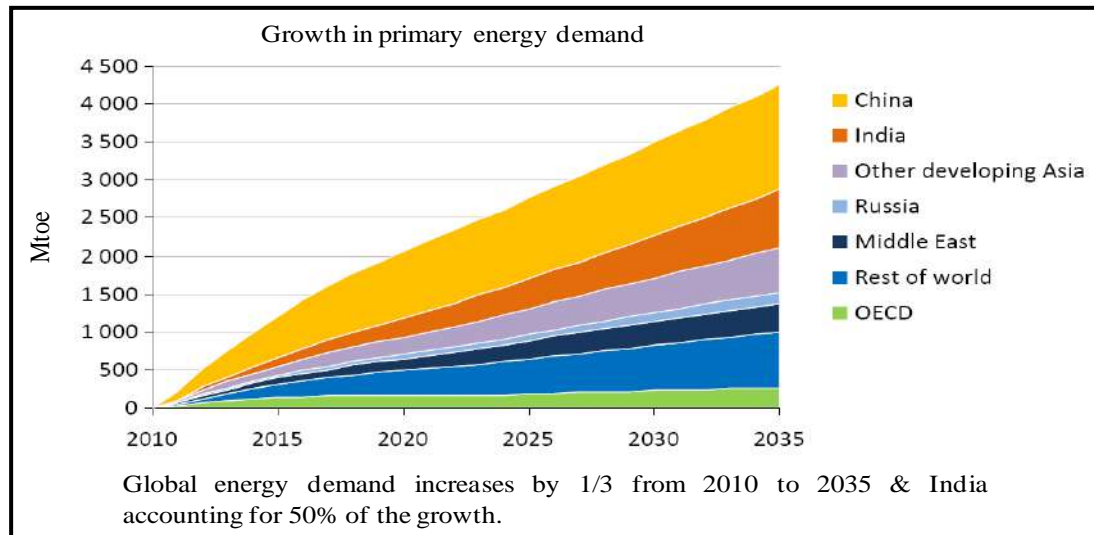


Fig. 1.3 — Energy profile of various countries from 2010-2035 (Source: World Energy Outlook Report 2012 and India).

1.2 High-Temperature Thermal Power Plants: The Need of the Day

High-temperature thermal power plants could breathe a new life into the traditional coal-fired power plants by operating at a high-temperature range of supercritical and ultra-supercritical capable enough to achieve an energy conversion efficiency of 40 and 43 pct (%), respectively. Wherein the traditional thermal power plant releases 1100 g CO₂/KWh, the state of the art technology known as *green and clean technology/carbon capture technology/high-efficiency low emission (HELE)* [5] releases only 660 g CO₂/kWh. The aim of deploying HELE technologies is twofold: to increase energy conversion efficiencies and reduce CO₂ emissions. The application of high-temperature and pressure in the advanced thermal power plants (Fig. 1.4) not only improves the CO₂ reduction but also improves the energy conversion efficiency.

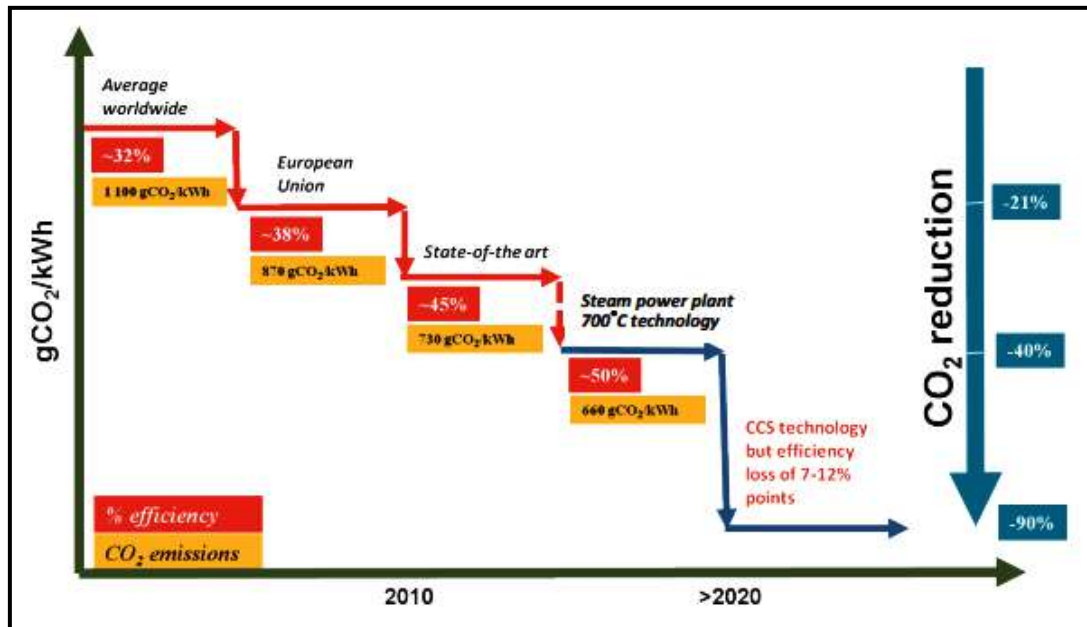


Fig. 1.4 — Indicative CO₂ emission reduction pathways (Source: Adapted from VGB Power tech, 2012).

Power plants operating at high-temperature and pressure have several benefits as follows:

- ✓ It reduces the CO₂ emissions,
- ✓ Raises energy conversion efficiency,
- ✓ It lowers global warming,
- ✓ Helps in sustainable development,
- ✓ Imposes less pressure on coal reservoirs,
- ✓ Clean and pure air increases the standard of living,
- ✓ Reduces transportation expenses,
- ✓ Ultimately leading to the economic growth of the country.

1.3 Supercritical Technology/Carbon Capture Technology

The discovery of new alloys has often brought dramatic changes in human civilization [6, 7]. For instance, the Sumerians discovery of Bronze alloys (an intimate mixing of

Cu and Zn). Societies that used this alloy merely dominated their neighbors. Years later, the ancestor of steel was born by the intimate mixing of iron in heated charcoal. Yet, only with the inventions of the steam engines, the bulk productions of steel begin. Thousand years of practice and recent technical understandings culminated in the development of super resistant and super ductile alloys. Today, high-temperature materials are going through similar revolutions, though at a much higher pace.

It is evident from Fig. 1.4 that increasing the steam temperature more than 973 K (700 °C) (often referred to as the advanced ultra-supercritical range) will solve the afforested issues of global warming and energy efficiency in one go [8]. To this end, the selection of proper materials for high-temperature piping system possessing long-term microstructural stability and with inherent resistance to mechanical deformation [9-11], and high-temperature corrosion resistance is a major technological challenge for researchers in India and across the globe. In this endeavor, where the conventional high-temperature materials like ferritic-martensitic steels (P91, P92) fall short of these requirements [12, 13], other high-temperature material needs to be investigated. The use of Ni-based superalloys [14-17] are showing potentials owing to their better creep rupture life [18], excellent oxidation, and corrosion resistance [19, 20] even in the advanced ultra-supercritical conditions of 973 K to 1033 K (700 °C to 760 °C) and under high pressures of 35 MPa [21]. Amongst Ni-based superalloys, Alloy 617 is one of the forerunners and the leading candidate piping materials for high-temperature applications and are likely to be used in advanced ultra-supercritical thermal power plants with operating temperature regime of 973 K to 1033 K (700 °C to 760 °C) and pressure as high as of 35 MPa [21-23] in the next generation thermal power plants. A schematic representation of the evolution of different generations of power plants with operating specifications is shown in Fig. 1.5.

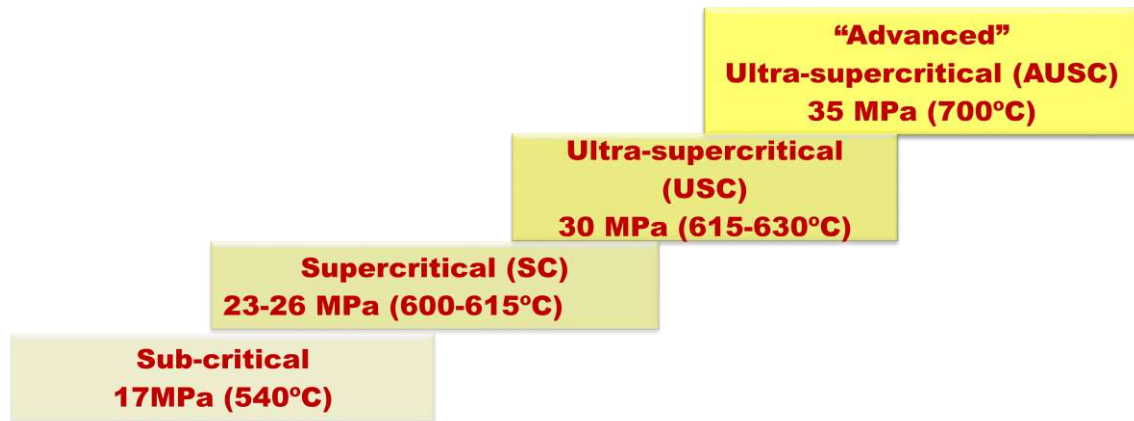


Fig. 1.5 — Progress in various stages of the thermal power plants.

1.4 Material Property Required for Advanced Ultra-Supercritical Thermal Power Plants

The critical components of boilers for the advanced ultra-supercritical thermal power plants ($> 973\text{ K}$) technology are: the walls membrane, furnace wall [24], the ultimate super-heater and re-heater stages, boiler tubes (hot sections), in- and outlet headers (extremely hot sections) as well as the thick-walled components, most importantly the high-pressure outlet headers, and the piping to the turbine (Fig. 1.6).



Fig. 1.6 — Schematics of the header used in thermal power plants.

As discussed above in the previous sections, the realization of advanced ultra-supercritical thermal power plants is associated with the development of stronger high-temperature performer materials capable of operating under high stresses at high values of temperatures and associated pressure. The use of high-temperature ferritic steels is actually limited to 873 - 893 K (600 - 620 °C) steam temperature. Having successfully developed the new alloys for operating temperatures close to ~ 923 K (650 °C), the major intrinsic limiting factor in using these alloys is their susceptibility to oxidation on the steam side where the temperature is extremely high. Therefore the candidate materials for the boiler components, which are being investigated intensively at the moment, are Alloy 617, Alloy 263, Alloy 740, and Alloy 800.

1.4.1 Required Mechanical Property

There exist significant differences in the physical and mechanical properties of the austenitic Ni-alloys and traditional high-temperature materials viz: ferritic steels (P91, P92), commonly used in coal-fired power plants. These differences not only have an impact on the metal forming process but also on the component behaviour under high-stress field with implication on the design, i.e. on the critical wall thickness requirement. In general, Ni-based alloys show a higher thermal expansion coefficient, but a lower thermal conductivity in contrast to ferritic steels. During start-up and shut-down of the power plant, thermal stresses caused by temperature gradients, especially in thick-walled parts will eventually appear in the form of stress.

The above-mentioned differences in thermal conductivity as well as in thermal expansion will lead to higher cyclic stresses in Ni-based alloys. Therefore, extra care must be given to component design considering the specific characteristics of the given materials to maintain the structural integrity of the component during the in-service conditions.

1.4.2 Microstructural Property

There exist an intimate relationship with the microstructure and mechanical properties of the materials [25]. The microstructural constituents like grain size, precipitate variants, and their evolution during the service condition influence the mechanical properties of alloys significantly, especially during the service conditions. The degradation of the microstructure can significantly reduce the performance of the material during service conditions. The hierarchical evolution of microstructures [26-28] during service conditions is a natural phenomenon of materials working at high temperatures. This process can be accelerated under the influence of external or internal stresses build during the operation of the power plant. This microstructure evolution can be beneficial or maybe detrimental too, and some time may lead to catastrophic failure. Microstructure stability is one of the major key factors which needs to be judiciously looked into while deciding the material for high-temperature applications. Hence, the role of microstructure can't be overlooked against the selection of materials for high-temperature thermal power plants application.

1.5 Qualification of Alloy 617 for Advanced Ultra-Supercritical Thermal Power Plant

To qualify for the advanced ultra-supercritical thermal power plants, a material should have the following properties:

- ✓ Material should possess excellent microstructural stability at high-temperature.
- ✓ Higher resistance to deformation due to mechanical loads at high-temperature.
- ✓ Reduced oxidation rate at high-temperature.
- ✓ Good heat transfer coefficient.
- ✓ Reasonable thermal expansion coefficient, etc.

Alloy 617 does possess excellent high-temperature stability [12, 22, 29]. Under oxidizing atmosphere, Cr forms a dense oxide film of Cr_2O_3 and thus passivates the layer protecting the alloy from significant environmental degradation [30] by stopping the inward diffusion of gases viz. oxygen and sulfur, etc. and upward diffusion of metals [31]. Al in conjunction with Cr also provides an extra armor and a second defensive mechanism against high-temperature oxidation and hence reduces the oxidation at high-temperature and maintains the grains and grain boundary-free of corrosion [32, 33]. This alloy has been investigated in numerous publicly sponsored and privately financed programmes with regard to its use in ultra-supercritical boilers [34]. Materials development projects for the advanced ultra-supercritical thermal power plants with steam temperatures of 1023 K (700 °C) and above have been performed in order to achieve high efficiency and low CO_2 emissions in Europe, US, Japan, and recently in China and India as well [35]. Based on the gained experience, international, and nationally the material has been tailored to fit the specific purpose of the boilers.

Under the National Mission for the development of advanced ultra-supercritical thermal power plants technology initiated in 2012 [36], this has gained momentum as one of the projects to be taken up on priority. This project is proposed to be executed in two phases. The objective of the first phase would be to undertake R&D on all aspects of advanced ultra-supercritical thermal power plants technology for thermal power plants to improve power plant efficiency, reduce carbon dioxide emissions, and reduce coal consumption per unit of power generated. In the second phase, an 800 MWe advanced ultra-supercritical thermal power plant demonstration power plant will be established based mainly on the technology developed in the first phase [36].

1.5.1 Developing Advanced Ultra-Supercritical Thermal Power Plant Technology Indigenously – A Necessity

In addition to pursuing indigenization efforts in self-reliance in energy, India has been keen and is continually acquiring scientifically proven technologies in power generation and other areas from abroad. While acquiring foreign proven technologies is easier and expeditious to implement, it should be clearly understood that by and large only limited design information and manufacturing techniques are shared with foreign collaborators. This results in perpetual dependence on foreign collaborators and suppliers and in the long run prove more expensive due to the persistent reliance on import of key materials and technologies. For instance, the import content of the technology acquired in the early 80's for 500 MWe sub-critical boiler, turbine generator sets continue to be as high as 30%. In the modern arena, technology acquisition encompasses a high level of mutual business sharing, which raises not only costs but also friction up the technology absorption process, and thus severely affect the indigenization and potential savings of expenses. For supercritical sets of 660 or 800 MWe rating, the import content is currently about 50%, which will gradually decrease with time [36].

1.5.2 Alloy 617: The Backbone of Indian Advanced Ultra-Supercritical Thermal Power Plant Programme

Towards developing advanced ultra-supercritical coal-fired power plants in India, Alloy 617 has grabbed substantial attention from researchers and is nowadays under active considerations of the high-temperature piping material for high-temperature applications in both the thermal and nuclear power plants.

Alloy 617 is a primarily a solid solution strengthened alloy and is believed to draw its exceptionally high strength both from the solid solution (ensured by Co and

Mo) strengthening [37] and from the precipitation strengthening originating from ordered γ' phase ($\text{Ni}_3(\text{Ti}, \text{Al})$) and M_{23}C_6 precipitates. Researchers also have an opinion that the presence of grain boundary carbides also offers a substantial degree of strength to this alloy [38] and this additionally boosts its high-temperature performances. Strengthening via carbides, still continues a ground of open debate and a clear idea can be accepted only when substantial work has been done in this direction. The oxidation resistance [39] is assured by Cr and Al and also has high creep strength [40]. In addition to these properties, this alloy also shows a good fabricability too [34].

1.6 The Scope of Advanced Ultra-Supercritical Thermal Power Plant and Clean Coal Technologies in India

India is a developing nation and hence requires more power generation indigenously to fulfill energy demand in the country. Thus there is an excellent scope for establishing clean coal technology [5] based on advanced ultra-supercritical thermal power plants in the country itself. India advanced ultra-supercritical thermal power plants technology with reduced CO_2 emission and scale-up energy conversion efficiency will certainly create employability too. Hence, looking at one decade down the line, the future of clean and green advanced ultra-supercritical thermal power plants technology is bright within the nation.

1.7 Objective and Scope of the Present Thesis Work

Alloy 617 is one of the candidate materials for high-temperature applications owing to its high-temperature strength, reasonable microstructural stability, corrosion, and oxidation resistance. However, the anticipated microstructural evolution during its exposure at a higher temperature for longer durations is still a matter of concern for the designers as the microstructure of this alloy strongly influences its deformation

characteristics and fracture resistance. The availability of deformation and fracture resistance data on Alloy 617 especially after high-temperature aging is scanty in literature. Thus, it is imperative that major advances in this direction must be made to explore these unexplored paths. This thesis work has been aimed to fill up some gaps in this arena towards ensuring component integrity in the high-temperature domain.

Three major aspects have been envisaged to be addressed in this thesis work plan:

- 1) Evolution of microstructure of Alloy 617 at different aging durations at a particular aging temperature of 750 °C.
- 2) Evaluation of the deformation characteristics of Alloy 617 with respect to the aging-induced microstructural evolution from the as-received to long term aged conditions, using hardness tests, and uni-axial tensile tests.
- 3) Evaluation of fracture resistance of Alloy 617 with respect to the aging-induced microstructural evolution from the as-received to long term aged conditions, using Charpy impact tests and finally establishing a structure-property relationship by generating data for the designers to manufacture better integrity among the components.

Literature Survey on Microstructure, Fracture, and Deformation Properties of Alloy 617

This chapter introduces the developmental aspects of materials for high-temperature applications to counter global greenhouse emissions and global warming. In continuity with chapter 1, this chapter will extend the discussion on global warming and the urgency to upgrade thermal power plants to next-generation power plants. A bird's eye view of the existing high-temperature materials and their transition from current to advanced ultra-supercritical thermal power plants technology with a special emphasis on Ni-based superalloy has been provided. This also includes the materials selected for high-temperature applications in advanced ultra-supercritical thermal power plant technology. A brief overview of the literature on Alloy 617 with respect to its microstructure, fracture, and deformation behaviour has been covered in this section.

2.1 Introduction

The inception of the thermal power plant has brought significant changes in the living standards of human life. Here to quote an English proverb

“Nothing comes free”

best suits to a thermal power plant. The thermal power plant brought energy to the society and raised the human development index (HDI) [41] but along with it also brought hazardous gases viz.: NO_x, SO_x, and CO₂, etc. For the first time, a team of scientists led by Daniel Feldman [42] at Lawrence Berkeley National Laboratory showed a direct link between rising levels of carbon dioxide — or CO₂ — in Earth's atmosphere and how much solar cell increment warms the lower atmosphere. This

finding presents a fundamental theory and describes the reason behind the recent worldwide warming of Earth's climate. It links a measurable share of that warming to human activities that release CO₂ from all the possible sources of CO₂ emissions. These include the burning of *fossil fuels* in thermal power plants (coal, oil, and gas) for heating, power, and transportation. CO₂ is known as a *greenhouse gas*. By that, they inferred that this gas allows the sun's ultra visible light to pass through them. But when that light hits Earth's surface, it can be transformed into heat (*infrared light*). CO₂ now traps that heat appearing in the form of *infrared light* (like a greenhouse window) and holds much of it within the lower atmosphere — right down to Earth's surface [43]. Such findings raise concern toward reducing global warming and putting a check to it as soon as possible to inflate it further. The menacing effect of global warming [44] has raised concern towards the safety of environments and the inhabitants on the planet.

A report from Liisa Antilla published in Global environmental change [45, 46] quoted that

“The [US] continues to be the largest single national source of fossil fuel-related CO₂ emissions reaching an all-time high of 1529 million metric tons of carbon in 2000”.

This report is a clear indication that if emissions from the thermal power plants are not checked, global warming will start playing a detrimental role in the environment. This report also presents that there exists substantial evidence that most of the observed global warming of recent dates over the last 50 years is attributable to extravagant human activities and other scientific bodies agree [47].

A significant step has been taken by major thermal power plant countries to operate their plants at a high-temperature with the advanced ultra-supercritical thermal power plant technology. A successful demonstration of the technology was performed around 1998 by the United States Department of Energy (U.S. DOE). The Ohio Coal

Development Office (OCDO) and Office of Fossil Energy have been thriving toward operating an advanced ultra-supercritical (AUSC thermal power plants) steam boiler and turbine with steam temperatures up to 1033 K (760 °C) and 35 MPa which will reduce CO₂ emissions by > 20 % or even more [21, 48, 49]. A variety of European projects [50] started in 1998 in the direction of AUSC thermal power plant technology aimed at steam temperatures of 923 K (700 °C) and higher to tackle these global warming issues seriously.

In 2001, the U.S. DOE in conjunction with OCDO and cost-share from all the major U.S. boiler and turbine original equipment manufacturers (Alstom, B&W, Foster Wheel, GE, and Riley Power), the three major energy-producing giants joined hand Energy Industries of Ohio (EIO), Electric Power Research Institute (EPRI), and with support from Oak Ridge National Laboratory (ORNL) managed through the National Energy Technology Laboratory (NETL) began an striving research and development project that would lead to higher efficiency of fossil power plants with reduced CO₂ emissions [48, 49]. US programme of AUSC THERMAL POWER PLANTS now being operated in Japan since 2008. Asian countries like China have also started working towards a cleaner and green AUSC thermal power plant technology.

In recent years, India under the umbrella of the National Mission for the Development of AUSC thermal power plants has initiated a significant step toward materials hunt for AUSC thermal power plants technology [36, 51] and had kept it at the forefront of the materials research. In the Indian scenario, the Ni-based superalloy Alloy 617, has been identified as one of the materials for the AUSC thermal power plant technology for ducting, boiler, and turbine components. There has been extensive research going on in the Materials Development and Technology Division (MDTD) of Indira Gandhi Centre for Atomic Research (IGCAR), Kalpakkam on this material. The results are favorable and support the idea of applying Alloy 617 toward high-

temperature application in AUSC thermal power plant technology. These materials are developed indigenously at Mishra Dhatu Nigam Limited (MIDHANI) Hyderabad, India and tested extensively for characterization of material properties. In the preliminary phase of project focus was mainly concentrated on the developing boiler components and after achieving a substantial level of achievement, the turbine components, which are also subjected to advanced ultrahigh-temperature and pressure, are currently under investigation [51].

Achieving a significant increase in coal-fired power plant efficiency requires substantial literature data from the past and the recently published articles. An increase in steam operating conditions demands extensive research and development to find new alloys and technologies capable enough to bear these harsh environments to realize these dreams come true.

Mankins et al. [22] performed a laboratory study on Alloy 617 to determine the effects of thermal exposure with temperature up to 1366 K (1093 °C) on the microstructure and phase stability of this alloy. Understanding the structure-property relationship during high-temperature exposure, microstructures were correlated with mechanical properties. The mechanical property was found to influence by the microstructural variations during the aging treatment directly. The possible phases as a small amount of gamma prime phase (γ') of the form $\text{Ni}_3(\text{Al})$ and M_{23}C_6 were found to exist. The microstructural examination showed that the size and shape of the γ' phase in the alloy is reluctant to aging. To understand the coarsening nature of γ' , it was kept for 10000 hours at 1033 K (760 °C). Surprisingly, they found that γ' being stable without any substantial change in the morphology. The fraction of γ' has been reported to be small, this paper also reports that M_{23}C_6 being discrete in nature, also helps in imparting strengthening [22, 52]. The major findings of this paper are (1) alloy's mechanical

properties is a function of its microstructures and (2) although the amount of γ' is small, it does provide some strengthening at temperatures of 922 K- 1033 K (649 - 760 °C)

This paper gives an idea of how important the microstructures can be in determining the mechanical properties of an alloy applied to the advanced high-temperature thermal power plant. Though this paper could not explore much of what has been explored today concerning the Alloy 617, this seminal work was a door opening to researchers working toward high-temperature materials. This was the first reported paper in the direction to show the existence of γ' and declare that they hardly change their morphology during aging.

Kimball et al. [23] studied the effect of thermal aging on microstructure and mechanical properties. The use of multi-component alloying systems for high-temperature structural component applications requires a deeper understanding of the microstructural changes which generally evolve during thermal exposure at sufficiently high temperatures. Previous studies on this alloy from Mankins revealed that there exists a one-to-one relationship between microstructure and mechanical properties. The Alloy 617 was mainly considered for mechanical property evaluation. The hardness values were measured only up to 8000 hours. The significant finding of this experiment lies in establishing a relationship that aging-induced hardening exists at all temperatures. Moreover, the SEM fractographic images from Charpy tests were available only till 4000 hours, so not much could be explained about fracture behaviour. All aging temperatures produced a decrease in impact strength of the material and the microstructure of as-received shows discontinuous carbides at the grain boundaries.

Kirchhofer et al.[53] studied the precipitation behaviour of the two major high-temperature alloys, one being nickel-based alloys Ni-Cr-22Fe-18Mo (Hastelloy-X) and other Ni-Cr-22Co-12Mo (Inconel 617) under aging conditions. This research paper mostly revolves around finding the type and morphology of the precipitates as a

function of isothermal treatment. The significant findings were not much different than that of Mankins et al. and Kimball et al. but the findings succeeded in establishing a clear time-temperature-precipitation relationship.

Findings from Kihara et al. [54] and other contemporary scientists were different for the same material; eventually, even the precipitates, reduction in strength, and ductility remained a matter of open discussion. To summarize the major outcomes from the experiments conducted on Alloy 617 are:

- The hardness was significantly influenced by the presence of carbides at the grain boundary, which was contrary to the findings of Mankins et al. [22].
- The effect of the tiny amounts of the fine γ' started to get some notice, though this group discarded it. This observation was also contrary to the findings of Mankins et al. [22].

To advance further the study on Alloy 617, Nanstad et al.[55] conducted an experiment toward fracture toughness of 9Cr-1 Mo-V and thermally aged Alloy 617. This experiment provided an overview of Alloy 617 plate, weld joint analysis with tensile, Charpy impact, and fracture toughness tests conducted at temperatures to 1223 K (950 °C). The specimens were aged to 5300 hours. Results of testing for thermal aging up to 5300 hours show a significant drop in Charpy impact energy even at room temperature. Results obtained from Krompholz et al. [56] for un-aged alloy shows a very high fracture toughness from room temperature to about 1023 K (750 °C). This paper provides a basic understanding of the effects of thermal aging on the fracture behaviour of Alloy 617 for 5300 hours aged at 1023 K (750 °C) with Charpy impact energy up to 1173 K (900 °C).

Murakumo et al. [57] studied the creep behaviour of Ni-based single crystal superalloys with various γ' volume fraction. Common superalloys consist of γ' and γ

phases, with a face-centered cubic (FCC) and L1₂ structures, respectively. It was first reported by one of the authors Harada et al. [58, 59] that the creep rupture life was the longest in the vicinity of 65 % γ' . This experimental finding gave a clear idea about the Ni-based alloys that in general, these alloys possess a substantially high creep-rupture lifetime. It shows very less effect of aging durations on the microstructure and thus remains almost unaltered. However, microstructural stability is an essential criterion for high-temperature applications.

Thomas et al. [37] conducted an experiment to understand the influence of grain boundary character on creep void formation in Alloy 617. Creep specimens were fabricated from the plate of Alloy 617 as per the standards followed in ASTM Standard E 139-06. The ratio of the gauge length (16.6 mm) to the diameter of the gauge (4.2 mm) was kept at 4.0. High-temperature creep tests were carried out on the specimens. The creep rates ranged from 8.5×10^{-8} m/second to 2.5×10^{-7} m/second and the temperature was maintained at 0.8 Tmp. The dominant deformation mechanism is expected to be dislocation creep at the stresses applied in these creep tests [25]. The microstructural characteristics in the vicinity of creep voids were analyzed by Orientation Imaging Microscopy (OIM) with the simultaneous acquisition of chemical information by EDS. It was noticed that voids were found to be more prevalent on grain boundaries.

Benz et al. [60] studied the aging behaviour Alloy 617 at two different sets of temperature one at 923 K (650 °C) and other at 1023 K (750 °C) and arrived at a conclusion that precipitation and coarsening kinetics of γ' phase chemically known as (Ni₃ (Ti, Al)) affects the creep properties of Alloy 617 at 1023 K (750 °C). Above this temperature, there is no formation of γ' , and hence many of the physical properties remain unaffected as can be seen from Fig. 2.1. This paper was the first report, which

presented a clear T-T-T diagram and also suggested that the formation of γ' can only be achieved at temperatures close to 1023 K (750 °C) and above which there was a negligible formation of such precipitates.

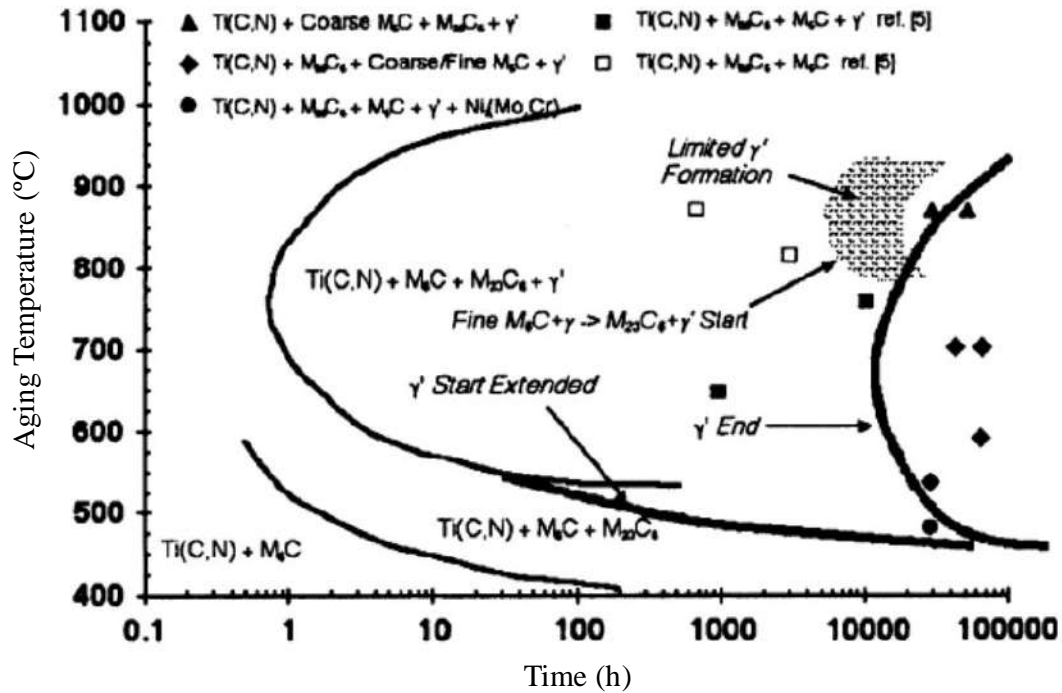


Fig. 2.1 — Time-temperature-transformation (TTT) diagram for long term aging of Alloy 617.

Recently, Vogel et al. [26] studied the evolution of hierarchical microstructures in a Ni-based superalloy. The phase separation of γ' precipitates determines the microstructure and mechanical properties of Ni-based superalloys. This study explains that in the course of aging, disordered γ spheres form inside ordered ($L1_2$) γ' precipitates, undergo a morphological change to plates and finally split the γ' precipitates. The presence of γ particles inside γ' affects coarsening kinetics and increases alloy hardness. It has been observed from this experiment that γ' is supersaturated in the nickel and drives the formation of γ particle. The Lifshitz, Slyozov, and Wagner (LSW) theory predicts coarsening of γ' precipitates with time t , according to $R^3 - R_0^3 = kt$: where R_0 is the average radius at the onset of coarsening and k is a volume fraction dependent rate

constant. According to LSW theory, the predicted radius evolution can be approximated by a $R \propto t^{1/3}$. This finding suggests that γ' can coarsen but the γ' coarsening is greatly suppressed by the formation and growth of γ particles. The point of interest is that the γ' can coarsen, which again deviates from the previous studies and the literature data published so far. This experiment holds a superior position against earlier experiments on the Alloy 617 on account of the fact that the application of the state of the art atom probe tomography (APT) instrument that reveals the presence of γ in γ' and its morphological changes.

2.2 Need for the Present Study

The literature review suggests that the Ni-based alloys are employed for high-temperature applications and are prone to undergo aging-induced degradation, reduction in ductility, strength reduction, and degradation in fracture resistance. The microstructure studies reported in the literature were carried out on various Ni-based materials systems, which may not be relevant to the present application of Alloy 617 for advanced ultra-supercritical thermal power plants. Though some literature studies match to our interest, but they differ widely in the opinion from other literature data. Eventually, their aging conditions are different and are not up to our required operating conditions. Though the reduction in fracture energy results has been attributed to the coarsening and redistribution of the precipitates, an unequivocal conclusion correlating the microstructural evolution and fracture resistance degradation is yet to be evolved. These results indicate that there is an urgent need to evaluate the deformation characteristics and the extent of fracture resistance degradation in terms of the aging-induced microstructural evolution of the Alloy 617 after a longer time aging treatment at high-temperature domain. The present study has made an effort to study the deformation characteristics and fracture resistance of Alloy 617 after aging treatment at

1023 K (750 °C) for different durations up to 20000 hours. The microstructural evolution during aging period and its correlation to the fracture energy also have been addressed.

This study assumes importance as there are not many reports on fracture and deformation behaviour of Alloy 617, especially after long term aging treatments. The present work also attempts to correlate the aging-induced microstructural evolution of Alloy 617 to its deformation characteristics and fracture resistance degradation during the course of aging treatments. This experiment is also conducted to get some insights into the Alloy 617 and bridge the existing varying opinion gap among the various research communities.

3

Experimental Techniques to Evaluate the Microstructure, Fracture, and Deformation Properties of Alloy 617

Materials selection, characterization, and its utilization for suitable applications involve studies and inspection by several complementary experimental techniques. This chapter describes in detail, the experimental techniques to characterize the Alloy 617. The major tools and techniques used for the preliminary as well as advanced characterization required for morphological, structural, and elemental analysis of the material have been discussed.

3.1 Introduction

A brief description of the experimental techniques utilized for the characterization of grain boundary, morphological, elemental, structural, and mechanical studies are discussed in this chapter. Alloy 617 was introduced to us in the solution annealed condition. Aging was further done at 1023 K (750 °C) for various durations. Post-aging, the material was air-cooled, and the fabrication process was accomplished as per the requirements of the tests. Grain boundary characterization was done by a light microscope. Hardness measurements and impact energy were also carried out to better understand the material behaviour toward high-temperature applications. Electron microscopy techniques such as SEM and TEM were used for morphological and structural studies of the as-received and aged alloy.

3.2 Materials Selection, Properties, and Their Composition

3.2.1 Alloy 617

The choice of material for advanced high-temperature thermal power plant applications is preliminary and the most complex procedure. The material selected for advanced high-temperature thermal power plant not only needs good creep strength: a phenomenon generally dominant at high temperature, but also requires an excellent corrosion resistance, a superb thermal microstructures stability, which is indeed a determining parameter for material's properties. Out of the several Ni-based alloys, Alloy 617 is selected as the most promising candidate material for high-temperature performance. Amongst Ni-based superalloys, Alloy 617 is one of the forerunners as the candidate piping materials for high-temperature applications and are likely to be used in a temperature regime of 973 K to 1033 K (700 °C to 760 °C) under high pressures of 35 MPa [21, 22, 61]. Alloy 617 is known to draw its high-temperature (>973 K /700 °C) strength both from the solid solution (ensured by Co and Mo) strengthening [37, 62] and from the precipitation strengthening originating from ordered γ' phase ($\text{Ni}_3(\text{Ti}, \text{Al})$) and M_{23}C_6 precipitates. Cr and Al assure the oxidation resistance [39]. In addition to these properties, this alloy also shows better fabricability.

The Alloy 617 was obtained from MIDHANI in a tubular shape with an outer diameter (OD) of 51.9 mm, a thickness of 11.9 mm, and a length of 700 mm (Fig 3.1). The as-received alloy was cold finished, solution annealed at 1443 K (1170 °C) and water quenched. The specimens were then aged at 1023 K (750 °C) for 1000, 5000, 10000, and 20000 hours, respectively, in a muffle furnace and air-cooled for further experiments.

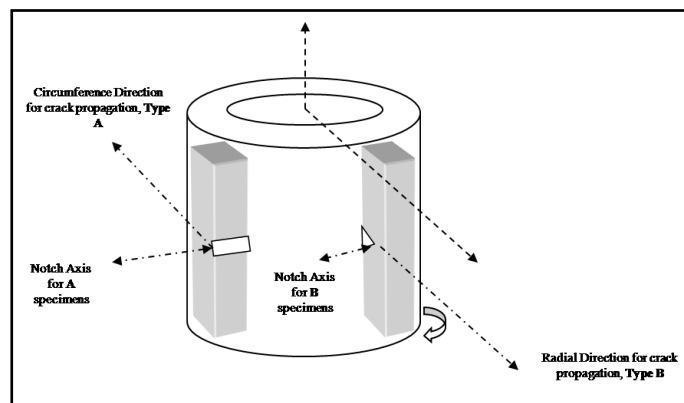


Fig. 3.1 — Schematic representations of Alloy 617 tubes in as-received condition with the notch orientation of the Charpy V-notch specimens used.

3.2.2 The Chemical Composition of Alloy 617

The chemistry of Alloy 617 is shown in Table 3.1 and their relationships with the periodic table are shown in Fig. 3.2. The science behind choosing these elements and their relationship with the periodic table can be grouped into three major classes (see Fig. 3.2). The first class includes elements from V, VI, and VII group of the periodic table (Co, S, Ni, Fe, Cr, Mo, N, and Mn) which prefer to form FCC austenite structure. Second class of elements (Ti, Al) partition to and constitute up the γ' precipitate $\text{Ni}_3(\text{Ti}, \text{Al})$ and are from III, IV, V group. Elements B, C, Si, and Cu hails from II, III, and IV group and constitute a third class that segregates to grain boundaries.

Alloy 617 owes its exceptional high-temperature strength and oxidation resistance via a solid-solution strengthening mechanism [63, 64] (imparted by Cobalt and Molybdenum). This alloy has spectacular corrosion [10] resistance (offered by Chromium) against a wide range of corrosive environments, and it can be easily formed and offers easy fabricability too. The main feature of this intimate mixing of alloying elements is to impart the necessary qualification required at elevated temperatures. When aged at 1023 K (750 °C), the formation of gamma-prime (γ') $\text{Ni}_3(\text{Ti}, \text{Al})$ an intermetallic [65, 66] precipitates imparts additional strength to the alloy. Furthermore, the formation of M_{23}C_6 , M_6C carbides, and $\text{Ti}(\text{C}, \text{N})$ precipitates provide some

additional strength [22] to the alloy making it more suitable to operate at higher temperatures. No signature of closed-packed structures, viz: sigma (σ) [67], chi (χ) or mu (μ) [68, 69] were found after aging for 10000 hours at 1023 K (750 °C). The fine precipitates of Ni₃(Ti, Al) has an ordered face-centered cubic (FCC) structure of the L1₂ (Cu₃Au) type A₃B compounds [70] and has Pearson symbol/Space group as cP4/Pm3m [71], respectively.

Table 3.1. The chemical composition (Wt. %) of Alloy 617 employed in this study.

| Elements | Ni | Cr | Co | Mo | Fe | Mn | Al | C |
|----------|--------|------|-------|-----|-------|-------|-------|--------|
| wt % | Bal. | 22.1 | 11.6 | 9.4 | 0.12 | <0.01 | 1.2 | 0.06 |
| Elements | Cu | Si | S | Ti | N | Nb | Vd | B |
| wt % | < 0.01 | <0.1 | 0.001 | 0.4 | 0.005 | 0.02 | <0.05 | 0.0036 |

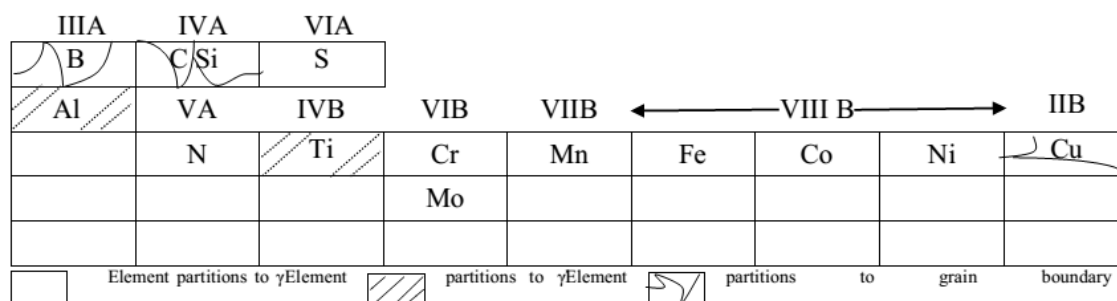


Fig. 3.2 — Important elements in the make-up of Ni-based alloys [72].

3.3 Methods of Specimen Preparation for Different Studies

Flat tensile specimens with dimensions as shown in Fig. 3.3 were machined from the heat-treated blanks as per the standard procedures mentioned in ASTM E8 [73]. Tensile tests at RT using nominal strain rates of $3 \times 10^{-3} \text{s}^{-1}$ were carried out on a floor model Hung Ta-2402 universal testing machine (UTM) and load–elongation-time to fail data were recorded for further analysis.

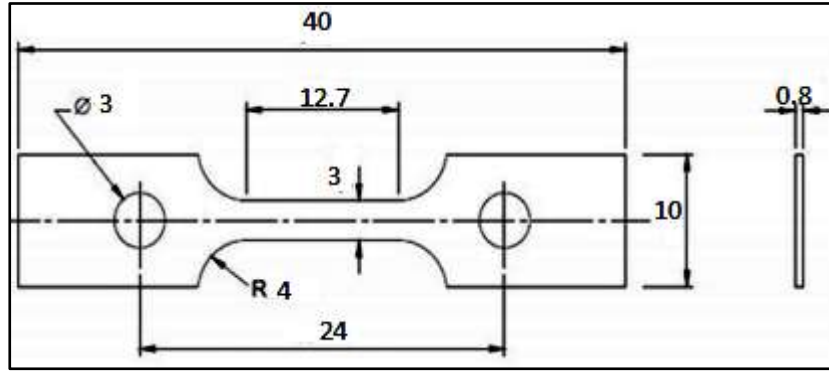


Fig. 3.3 — Schematic representation of miniaturized flat tensile specimen (dimensions in mm).

From the as-received and aged Alloy 617 tubes (as shown in Fig. 3.1), Charpy V-notch specimens (dimensions are shown in Fig. 3.4) were fabricated in conformity with the ASTM E-23 [74]. Towards assessing the notch orientation effect with respect to the wall thickness, two types of specimens with crack path in the circumferential direction (type-A) and with crack path in radial direction (type-B) has been prepared. The schematic of the tube as shown in Fig. 3.1 also shows the notch orientations used in Charpy V-notch specimens.

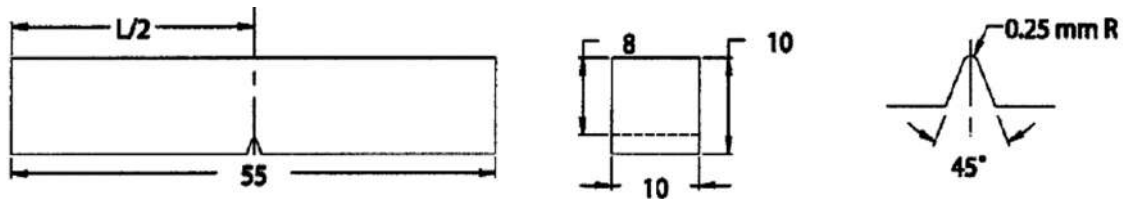


Fig. 3.4 — The standard V-notch Charpy specimen in compliance with ASTM E-23 standards (All dimensions are in mm).

The Charpy impact tests were conducted at the room temperature on a pendulum type Charpy machine with 358 J capacity as per the standard described in ASTM E-23-05 [60].

The sample preparation for the light microscope (LM) characterization is as follows: The Charpy tested specimens were received five in numbers. From the fracture surface, 12 mm was cut for SEM analysis and a further 10 mm was cut for optical

microscopy. The cut specimens were engraved for further investigation. A 10x10 mm² slice was cut out from the far end of the Charpy tested specimen.

Etching: For the as-received alloy, the samples were mechanically polished to a mirror finish and then etched with a solution of Aqua-regia (3HCL:1HNO₃). For aged specimens, following the mechanical polishing, the samples were electro-etched with an optimized solution mixture of 60% HNO₃ and 40% H₂O, at room temperature, using 1.5 V for etching times varying from 5 to 120 seconds.

For SEM analysis the fracture surface was thoroughly rinsed in the ultrasonic bath with acetone for 10 minutes and then dried up completely. Specimens were kept in a seal tight box to avoid any dust contamination on the surface to prevent any artifacts while fractography.

The samples for TEM were prepared as follows: the specimens were cut from the bulk material and mechanically ground to obtain a foil of 80 µm thicknesses, from which disks of 3 mm were preferentially punched. Twin-jet electropolishing was then carried out at a temperature of about 243 K (30 °C) at 15 V, using an electrolytic solution of 20 pct Perchloric acid (HClO₄) in a Struers Tenupol-5®. TEM investigation was carried out in a Philips CM200 analytical transmission electron microscope (ATEM) operating at 200 kV. The identification of phases was carried out by a combination of selected area electron diffraction (SAED) pattern and energy dispersive spectroscopy (EDS) analyses. Advanced TEM sample preparation facility at MMG, IGCAR is shown in Fig. 3.5.



Fig. 3.5 — Advanced TEM sample preparation facility at MMG, IGCAR.

3.4 Grain Boundary Characterization Using Light Microscope

For grain boundary (GB) inspection, a light microscope (LM) Leica DM IRM (Model: TK-C1480BE) was used as shown in Fig. 3.6.



Fig. 3.6 — Actual image of light microscope facility at MMG, IGCAR.

Alloy 617 is characterized using a microstructural and mechanical characterization tool. Microstructural characterization includes Light microscope, SEM/EDS, and TEM characterization, whereas mechanical characterization includes Vickers, Tensile, Charpy impact tester, and Instrumented Charpy machine.

Light microscope (LM) is one of the primitive and the most commonly used instrument for the characterization of a variety of materials from micron to sub-micron level. LM is the conventional and the most familiar device for magnifying a small specimen that cannot be viewed by the naked eye. LM is a simple lens system consisting of an objective lens with a short focal length (few mm), which creates an image of the object in the intermediate image plane. This image, in turn, can be viewed with another lens, the eyepiece, which provides further magnification. Conventional LM still maintains its position as the best, most comfortable, fastest, and the most widely used method of micro-characterization tools before switching over to the advanced microscopy techniques. Light microscope (Leica DM ILM, Germany) model was used for the characterization of the following materials in the thesis:

1. The as-received Alloy 617 after Charpy impact test.
2. The aged Alloy 617 after Charpy impact test for grain size measurement using Light microscope.

3.5 Structural and Morphological Characterization

The physical properties of a material bear a strong correlation with the chemical constituents of elements that usually build the material. Thus, it is indispensable to understand and ultimately tailor the properties of the material by revealing the genetic makeup of the material. Toward achieving this, a detailed characterization of the material structure down to the atomic level is required. Imaging, measuring, modeling, and manipulating matter at dimensions of roughly 1 to 100 nm can be accomplished with the help of emerging nano-characterization techniques such as SEM, TEM, AFM, STM, and FESEM with the capability to achieve high spatial and analytical resolution. However, in our experiment, we have used SEM and TEM; hence we will focus on these two techniques.

3.5.1 Scanning and Transmission Electron Microscopy

Electron microscopes were developed because of the limited image resolution in light microscopes imposed by their wavelength range. From the Rayleigh criterion, the smallest distance (δ) that can be resolved, is approximately given by $\delta \approx 0.61 \times \frac{\lambda}{\mu \sin \beta}$, where λ is the wavelength of light, μ is the refractive index of the viewing medium, and β the semi-angle of collection of the magnifying lens. The resolution limit of a microscope depends on the wavelength used to form the image. Short wavelength provides higher resolution than a longer wavelength in otherwise identical systems. The wavelength (λ) of an electron can be calculated by

$$\lambda = \frac{h}{\left[2m_0 eV \left(1 + \frac{eV}{2c^2 m_0}\right)\right]^{1/2}} \quad (3.1)$$

where h is Plank's constant, m_0 is the mass of the electron, e is the charge of the electron, V is the applied electric potential, and c is the speed of light. The term in the bracket $\left[\left(1 + \frac{eV}{2c^2 m_0}\right)\right]^{1/2}$ is the relativistic correction term applied when the incident electron energy is ≥ 100 keV. A schematic electron-matter interaction is shown in Fig. 3.7.

All electron microscopes take benefit of the particle and wave-like behavior of electrons to obtain very high-resolution images. The electron scattering process is a succession of particle nature, while electron diffraction is governed by a wave theory. In the scattering process, those electrons that do not deviate far from the incident-electron direction give us the information regarding the internal structure and chemistry of the specimen. TEM construction allows the gathering of these electrons. Another form of scattering where electrons are scattered though large angle (e.g. Backscattered electron) and electrons ejected from the specimen (e.g. Secondary electrons) are of much greater interest in the SEM. These electrons provide atomic number contrast, surface-sensitivity and topographic images.

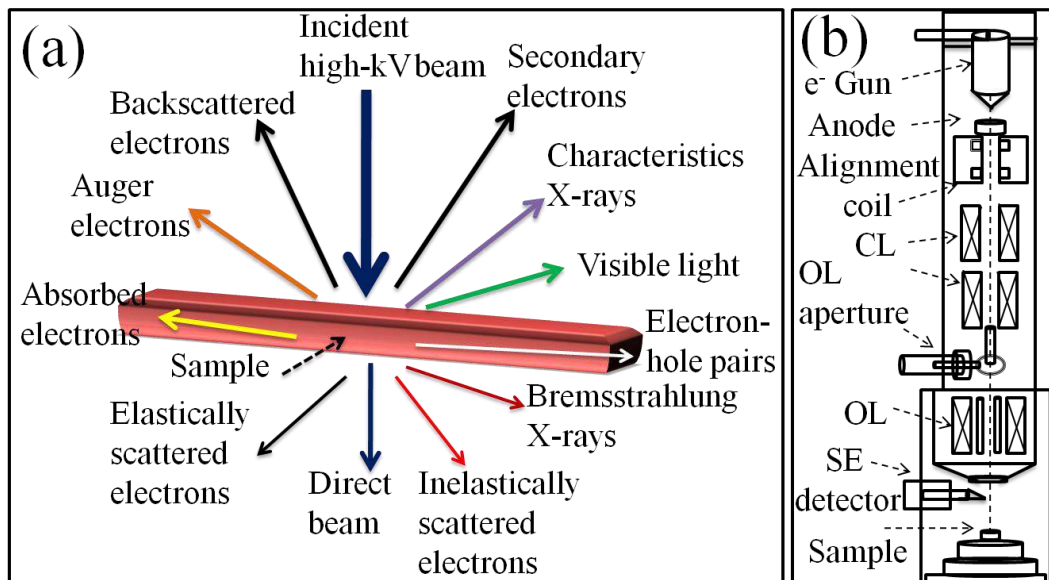


Fig. 3.7 — (a) Schematic representation of the several interactions occurs in a material due to the incidence of the high energy electron beam; (b) Block diagram of a FESEM showing the major components of the system.

3.5.1.1 Scanning Electron Microscopy/Energy Dispersive X-Ray Spectroscopy

Scanning electron microscope (SEM) is one of the most advanced imaging tools to analyze the surface morphology, microstructural analysis, nanomaterials, and nanostructures characterization wherein the images of the specimen is formed by scanning it with a high-energy focused electron beam.

In principle, the high-energy focused electron beam is thermionically generated by applying a voltage to the electron-emitting gun fitted with a tungsten filament acting as a cathode or lanthanum hexaboride (LaB₆) cathode. When a beam of electrons interact with a specimen with a very fine spot size of ~5 nm and having energy ranging from a few hundred eV to 30 keV, it undergoes either elastic or inelastic scattering. The emitted electrons after scattering with the energy of < 30 eV are popularly known as the secondary electron (SE). The elastically scattered electrons with angle ~180° are referred to as backscattered electrons (BSE) (Fig. 3.7 (a)). SE and BSE carry a rich source of information about the atomic number (z) – contrast, surface topography, and elemental composition about the specimen and the information is detected in

corresponding detectors. The major components of a SEM (Schematic view, Fig. 3.7 (b)) are listed above.

The interaction of electrons with the atoms of the specimen produces signals which provide information mainly about the specimens. The electron beam is thermionically emitted from an accelerated electron beam of energy around 0.2 to 40 keV is focused by one or two condenser lenses to a spot of about 0.4 to 5 nm in diameter. The accelerated electron beam (primary electron beam) interacts with the surface of the specimen, and the electrons lose their energy by repeated random scattering and absorption within a teardrop-shaped volume of the specimen known as the interaction volume. Secondary electron (SE), backscattered electron (BSE) and absorbed electrons are produced due to exchange of energy between the electron beam and the specimen, each of which can be detected by specialized detectors. Various types of electronic amplifiers are used to amplify the signals and are displayed as variations in brightness on a cathode ray tube (CRT). The raster scanning of the CRT display is synchronized with that of the beam on the specimen in the microscope, and the resulting image is, therefore, a distribution map of the intensity of the signal being emitted from the scanned area of the specimen. The image can be captured by photography from a high-resolution cathode ray tube, but in modern technology, it can be digitally captured and displayed on a computer monitor and saved in a computer's hard disk [75].

In the present thesis, SEM attached with energy-dispersive X-ray spectroscopy (EDX) was used to characterize the as-received and aged materials and elemental composition analyses. The Oxford INCA PentaFET-x3 Si(Li) microscope fitted with EDX models of SEM system and operated at 20 kV in the secondary electron mode used in the present thesis.

3.5.1.2 Transmission Electron Microscope (TEM)

TEM comprises a range of different instruments that make use of the properties of electrons, both as particles and as a wave [76]. The TEM generates a wide range of signals which can be processed to obtain atomic resolution images, diffraction patterns (DP), and different kinds of spectra from the small region of the specimen. It produces a much-localized electron probe, typically < 5 nm and at best, < 0.1 nm in diameter. The beam current can be as high as ~ 0.1 -1 μA . The wavelength of an electron accelerated by a 200 kV potential (a typical TEM operating parameter) is 2.51 picometer (pm) which is five orders of magnitude smaller than the wavelength of visible light. It provides valuable information about specimen chemistry and crystallography. TEM comes in wide variants, namely high-resolution transmission electron microscope (HRTEM), field-emission transmission electron microscope (FETEM), scanning transmission electron microscope (STEM), Analytical Electron Microscope (AEM), high voltage electron microscopy (HVEM), and intermediate voltage electron microscopy (IVEM). A schematic diagram of the TEM is given in Fig. 3.8. TEM can be viewed as a set of three essential components: the illumination system, the objective lens/stage, and the imaging system.

The illumination system comprises the gun and the condenser lenses and its role is to take the electrons from the source and transfer them to the specimen. It can be operated in two principal modes; parallel beam [for TEM and selected area electron diffraction (SAED)]. The objective lens/stage system is the heart of the TEM, which extends over a distance of 10 mm at the center of the column. In this critical region, beam-specimen interactions take place, and the two fundamental TEM operations occur. These pertain to the creation of various images and DPs that are subsequently magnified for viewing and recording. The imaging system uses several lenses to magnify the image or DP produced by the objective lens and to focus these on the

viewing screen through a detector; charge coupled device (CCD) detector, or TV camera.

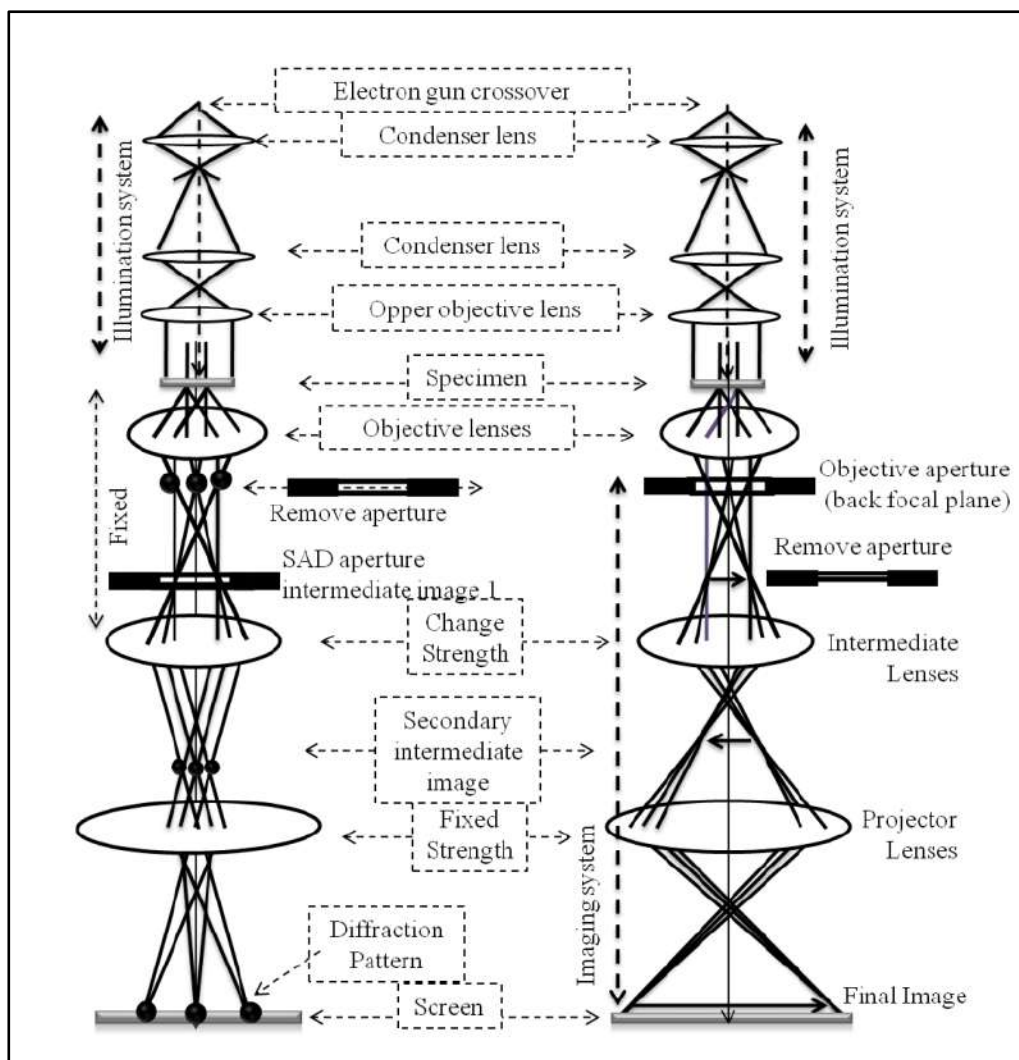


Fig. 3.8 — The highly simplified working diagram showing two basic operations of the TEM imaging system involving diffraction mode where the DP was projected onto the viewing screen (left side), and image mode where the images were projected onto the viewing screen (right side).

In this thesis work, a CM200 Philips TEM was used to substantiate the characterization of Alloy 617 and is shown in Fig. 3.9.



Fig. 3.9 — The actual image of the TEM facility at MMG, IGCAR.

3.6 Mechanical Characterization

3.6.1 Vickers Hardness Testing

Indentation hardness tests such as Vickers, Brinell, Rockwell, Knoop, and instrumented indentation are frequently used methods for determining the hardness of a material. In this thesis, the Vickers macro hardness test formally known as the Diamond Pyramid Hardness (DPH) test is used to characterize the Alloy 617.

The governing principle of all these tests is quite similar. The basis of static indentation tests is that a diamond indenter is forced onto the surface of the material being tested for a preset duration. The full load is normally applied for 10 to 15 seconds. The two diagonals of the indentation left out on the surface of the material after

removal of the load are measured using a microscope and their average are calculated. When the force is applied to the test material through contact with the indenter the test material yields. Once the force is removed, some plastic recovery in the direction opposite to the initial flow is expected, but over a very smaller volume. Because the plastic recovery is not complete, biaxial residual stresses remain in planes parallel to the free surface even after the force is removed. The hardness value is calculated by the amount of permanent deformation or plastic flow of the material observed relative to the test force applied. The deformation is quantified by the area or the depth of the indentation (d). The numerical relationship for Vickers hardness (HV) is inversely proportional, such that as the indent size or depth increases, the hardness value decreases [77].

$$HV = 1569.7 P/d^2 \quad (3.3)$$

where P: test force (gf), d: is the mean diagonal of the indentation (mm), and a square-based, pyramidal indenter with a 136° angle is used.

The hardness value is derived from two primary components: (i) a constraint factor for the test measurement, and (ii) the uniaxial flow stress of the material being involved in the test. The value of the constraint factor depends mainly on the shape of the indenter used in the hardness test. For relatively blunt indenters such as Vickers, Brinell, and Knoop, the constraint factor is approximately three. Prandtl in his seminal work first explained the origin of the constraint factor (for more details refer work by Prandtl, 1920) [78]. He compared the blunt hardness indenters to the mean stress on a two-dimensional punch required for the onset of plastic flow beneath the punch. The material beneath the punch was assumed to flow plastically in plane strain, and the material surrounding the flow pattern was considered to be rigid. Hill generalized Prandtl's approach into what is now known as the slip line field theory. Hill calculated a constraint factor very similar to Prandtl. According to these theories, the material

displaced by the punch is accounted for by upward flow. If the material is hard, a relatively small or shallow indentation will result, whereas if the material is soft, a fairly large or deep indentation will result [77]. The average value of ten Vickers indentations made on the coatings was calculated and used.

In the present study, macrohardness of the as-received solution annealed and aged specimens for 20000 hours aged at 1023 K (750 °C) was determined with a load of 10 kg applied for 15 s on various regions of the specimens using FIE microhardness tester shown in Fig. 3.10. The testing body was a four side diamond-pyramid which locks in an angle of 136°. On the coating, a quadrangle impression is made by the plastic deformation caused by the diamond indenter.



Fig. 3.10 — Hardness measurement facility in IGCAR.

3.6.2 Tensile Testing Machine

The tensile test is one of the simplest and widely used tests on materials to determine how a material will react when it is pulled apart when a force is applied to it in tension. By measuring the force required to elongate a specimen to the breaking point, material

properties can be determined that will allow designers and quality managers to predict how materials and products will behave in their anticipated applications. ASTM E-8 provides guidelines and procedures to conduct a uniaxial tensile test and obtain data about strength and ductility. Ductility, on the one hand, is the ability of a material to deform under tensile load and forms the basis for the metal forming process. Strength, on the other hand, is the ability of the material to bear the applied load without undergoing plastic deformation. The information that can be extracted from the tensile data is in plenty viz. Engineering stress-strain, true stress-strain, % elongation, yield strength (YS), ultimate tensile strength (UTS), flow behavior of the material and work hardening characteristics are just to name a few.

For the present study on the tensile test screw-driven machine model, Hung Ta-2402 is used as shown in Fig. 3.11 available in materials development laboratory (MDL) building of IGCAR.



Fig. 3.11 — Tensile test facility at IGCAR.

3.6.3 Charpy Impact Testing Machine

The impact test method based on a pendulum, popularly called a Charpy test, is one of the most cost-effective material testing procedures [79], often have been followed since past many decades. The name of Charpy remains associated with the impact testing on the notched specimen [80]. The impact energy measured by Charpy impact testing is used as a measure of impact toughness of the materials.

In the present study, the Charpy impact test was carried out using the Charpy test facility at IGCAR (model Tinius Olsen, maximum capacity 358 J) shown in Fig. 3.12 available in materials development laboratory (MDL) building of IGCAR.



Fig. 3.12 — Charpy Impact toughness facility at IGCAR.

3.6.4 Instrumented Drop Weight Testing Machine

The Instrumented Charpy machine is also known as an accelerated drop weight testing machine. The purpose of this machine is to understand the materials fracture behavior when they are subjected to dynamic loading. Impact velocities can be varied by varying the mass in the mass carrier area. The testing of materials under dynamic conditions need an efficient and reliable equipment to experimentally examine and quantify the dynamic behavior of materials under varying velocity impact loads. The range of such impact loads varies from a few m/s to several hundred m/s. It is not possible for any single machine other than this which covers a wide range of velocity.

In this present study instrumented Charpy impact test was carried out using an accelerated drop weight testing facility at IGCAR (model IM 10) shown in Fig. 3.13 available in materials technology division (MTD) building of IGCAR.



Fig. 3.13 — Instrumented Charpy accelerated drop weight testing facility at IGCAR.

3.7 Summary

The experimental techniques utilized for the study of Alloy 617 reported in this thesis are described briefly with the basic principle, significant components of the apparatus, and their technical specifications with schematic or real images of the available facility at IGCAR. Electron microscopy techniques of SEM and TEM utilized for morphology, structure, and elemental analysis of the microstructural study of the aged Alloy 617 are elaborated with the help of schematic diagrams.

Study of Microstructural Evolution for As-Received and Aged Alloy 617

Alloy 617 is one of the Ni-based superalloys which undergo microstructural changes during the prolonged exposure at higher temperatures. Thus, aging treatments at 1023 K (750 °C) for different time durations are expected to bring out the different microstructural changes, relevant to the actual situations during operation. The anticipated changes which could occur during the aging treatments can be the grain size distribution or the changes in the types, sizes, shapes, and distribution of the sub-microscopic precipitates. These issues have been investigated with the help of optical microscopy, scanning electron microscopy (SEM), and transmission electron microscopy (TEM) at different length scales. This chapter describes the study of the microstructural evolution during the course of thermal aging, as investigated with the optical, SEM, and TEM studies for the as-received material and also for the aged materials, with different durations of aging up to 20000 hours at 1023 K (750 °C).

4.1 Introduction

Alloy 617, a member of the superalloy family with a solid solution strengthened capability is one of the most demanding materials for high-temperature applications above 973 K (> 700 °C), especially for long-duration exposures. As discussed in earlier chapters, the ability of this alloy to satisfactorily work in a high-temperature regime is attributed to its exceptional combination of high-temperature strength, microstructural stability, corrosion resistance, and good fabricability. However, the high-temperature mechanical properties, i.e., the deformation characteristics and the fracture resistance of this alloy are strong functions of the microstructural features like grain size and types, size, shape, and distribution of the precipitates. From the discussion in the previous

chapters, it can be anticipated that the microstructural features as observed in the as-received material (solution annealed) undergo significant modifications to influence the deformation characteristics and fracture resistance after long term exposure in the high-temperature regime. To this end, for this Alloy 617, it is essential to understand the aging-induced evolution of microstructure at different length scales to meaningfully characterize its deformation characteristics and fracture resistance. This chapter brings forth the results of the microstructural investigation of Alloy 617 in as-received and in aged conditions, carried out at different length scales using optical, SEM, and TEM studies. The aging treatments, as mentioned in chapter 3, encompass the temperature domain of interest in this material for the advanced ultra-supercritical thermal power plant.

4.2 Optical Metallographic Studies of the As-Received and Aged Alloys

Optical metallography studies have been carried out mainly to evaluate the grain sizes of this material in the as-received and aged conditions. A polycrystalline material generally consists of thousands of individual grains separated by boundaries, scientifically known as grain boundary [81]. Grain boundaries (GB) can be defined as a 2D defect present inside the material, which often tends to decrease the electrical and thermal conductivity of the material and on the other hand helps in impeding grain boundary migration and checking the dislocation motions. It is usually assumed and accepted that the grain boundaries are of two to three atomic layers thick in a polycrystalline material. Typically, the crystalline orientations on either side of the grain boundaries are different, as schematically represented in Fig. 4.1. This typical orientation of the grains along the grain boundaries have several implications on the mechanical properties of the materials and thus are the active centers of investigations.

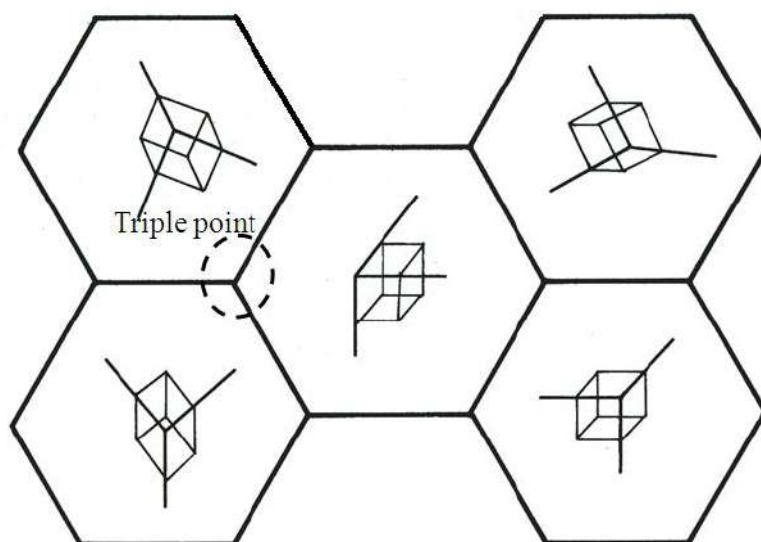


Fig. 4.1 — Schematic diagram of grain boundaries in polycrystals showing the different orientation of the adjacent grains along with the triple point boundaries.

Fig. 4.2 shows the micrographs of grain size in Alloy 617 in its as-received conditions. It is mainly characterized by the presence of polygonal grain structure with duplex mode [82] of grain size distribution as shown in Fig. 4.2 (a). The ‘duplex mode’ indicates toward two groups of grain sizes, the smaller grains with size ranges in 10-30 μm and larger grains with size varying from 40-100 μm . The larger grains could easily grow in the absence of any restriction or without any Zener pinning during the annealing or aging treatments. This duplex nature of grain size could be attributed to Zener pinning [83]. Zener pinning is a well-known phenomenon that explains the effect of smaller and finer precipitates on the movement of grain boundaries. It is generally inferred that a higher degree of precipitation could impede the grain boundaries leading to sluggish grain growth, whereas the grains grow faster in the precipitate free regions. A substantial presence of annealing twins has been noticed in the as-received microstructure and shown in Fig. 4.2 (a). The presence of annealing twins has a lot more to say about stacking fault energy (SFE) of this material. A similar observation on the existence of annealing twins in other superalloys material has also been reported in

the literature [74, 84]. The frequency distribution chart is shown in Fig 4.2 (b) reveals that the majority of grain size lies in the range of ASTM numbers 4 - 6.

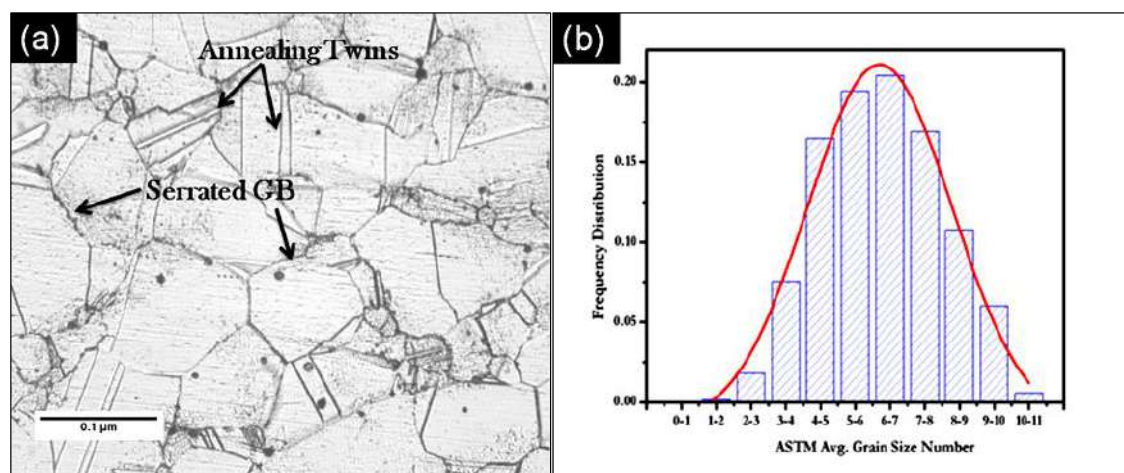


Fig. 4.2 — Microstructure of Alloy 617 obtained at 100X: (a) as-received alloy; (b) Frequency distribution of grain size in Alloy 617 vs. ASTM number for as-received alloy.

Fig. 4.3 (a) shows the optical micrographs of Alloy 617 after 1000 hours of aging treatment. It can be noted that the extent of annealing twins reduced substantially w.r.to as-received condition. The as-received alloy does have some serrated grain boundaries, but the degree of serration is much smaller in 1000 hours aged material. These serrations in the aged alloy indicate that there are indeed small amounts of grain movement and coarsening had occurred during high-temperature exposure. The possible and likely explanation for the serrations in the grain boundaries of this aged alloy is due the secondary phases such as grain boundary carbides pin sections of the grain boundary during migration, thus causing irregular boundaries. Another contributor may be due to the diffusion of carbon along the grain boundaries. Since carbon could be using the grain boundary as a fast diffusion path, a flux of vacancies in the opposite direction would be necessary [60]. Any flux divergence between the vacancies and carbon atoms in the banded regions would cause vacancies to pile up on the grain boundary, thus allowing for a climb of the grain boundary dislocations and

small serrations to form. The frequency distribution chart is shown in Fig. 4.3 (b) reveals that the majority of grain size lies in the range of ASTM number 4 - 6.

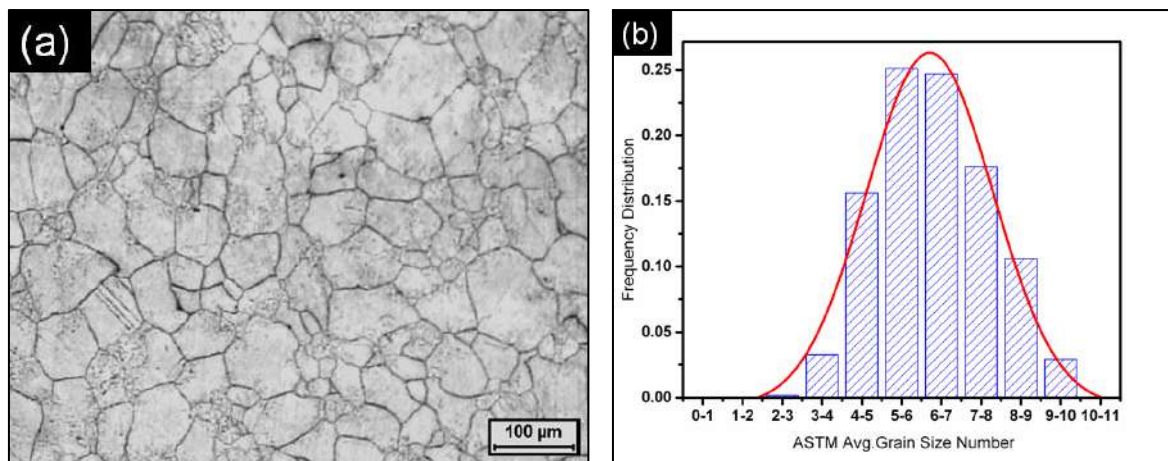


Fig. 4.3 — Microstructure of Alloy 617 obtained at 100X for specimens aged at 1023 K (750 °C): (a) 1000 h; (b) Frequency distribution of grain size in Alloy 617 vs. ASTM number for 1000 h aged alloy.

The microstructure of alloy, aged at 5000 hours is shown in Fig. 4.4 (a). The difference in aging-induced microstructure evolution between 1000 and 5000 hours is much more significant. The significant difference is in terms of carbide banding which has now become increasingly difficult to distinguish due to large amounts of carbide precipitation clustered on and near the grain boundaries. Another remarkable and distinguishable feature of the aging-induced microstructure evolution after aging for 5000 hours is that carbide precipitates have clumped together into small groups which are seen clearly in Fig. 4.4 (a). To these clumped precipitates of carbides, Mankins et al. [22] on their mechanical study on Alloy 617 gave a new nomenclature commonly known as “sunburst” patterns, and they were mostly observed in creep tested samples operated at 1089 K (816 °C) for 3000 hours. Carbides growth during the annealing process likely created dislocations which provided nucleation sites for new precipitation during subsequent aging. The frequency distribution chart shown in Fig. 4.4 (b) reveals that the majority of grain size lies in the range of ASTM numbers 4 - 6.

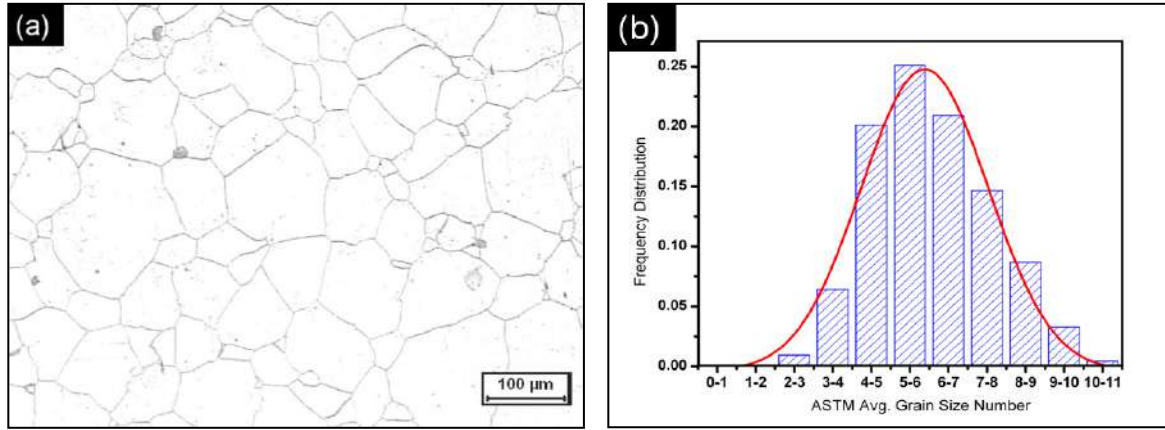


Fig. 4.4 — Microstructure of Alloy 617 obtained at 100X for specimens aged at 1023 K (750 °C):.(a) 5000 h; (b) Frequency distribution of grain size in Alloy 617 vs. ASTM number for 5000 h aged alloy.

Fig. 4.5 (a) shows the microstructure of alloy aged at 10000 hours. There is a significant difference in the microstructure of 10000 hours aged alloy. The extensive precipitation of carbides is one of the salient features of this microstructure. Other features of the 10000 hours aged material can be extracted from the frequency distribution profile shown in Fig. 4.5 (b). As can be seen from the frequency chart that there is a slight shift in the distribution chart from ASTM numbers 4 - 6 to 5 - 7. This shift is an indication that aging has a contribution to not only microstructural evolution but also plays a role in grain growth. Though the increase is insignificant, precipitation of carbides is remarkable.

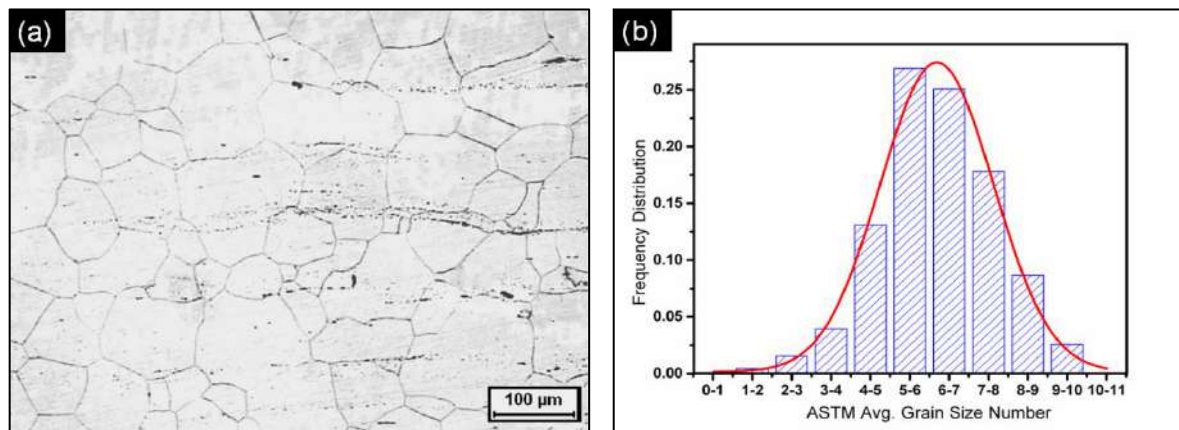


Fig. 4.5 — Microstructure of Alloy 617 obtained at 100X for specimens aged at 1023 K (750 °C):.(a) 10000 h; (b) Frequency distribution of grain size in Alloy 617 vs. ASTM number for 10000 h aged alloy.

The microstructure of 20000 hours with the aging condition maintained at 1023 K (750 °C) is shown in Fig. 4.6 (a). There is a significant difference in microstructure of 20000 hours aged alloy w.r.to.10000 hours. The extensive precipitations of carbides in 10000 hours have coarsened to a large extent, as can be seen from the micrograph in Fig. 4.6 (a) in the form of dark spots. Another salient feature of this microstructure is its uniform grain size distribution. After 20000 hours of aging, the grains have become more uniform in nature and occupied the ASTM numbers 4 - 6 as can be seen from the frequency distribution profile in Fig. 4.6 (b).

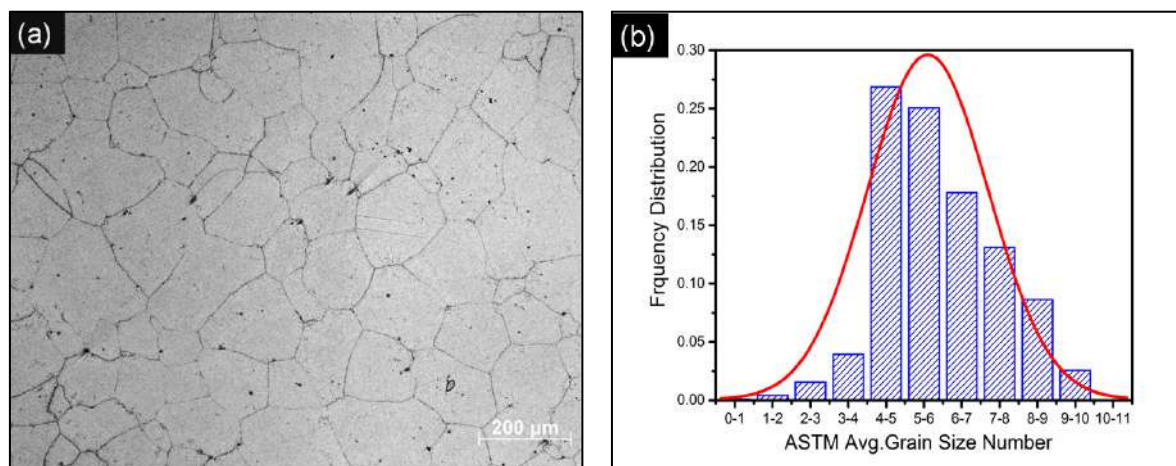


Fig. 4.6 — Microstructure of Alloy 617 obtained at 100X for specimens aged at 1023 K (750 °C). (a) 20000 h; (b) Frequency distribution of grain size in Alloy 617 vs. ASTM number for 20000 h aged alloy.

To appreciate the microstructural evolutions in Alloy 617 and have a clear understanding of grain boundaries in this alloy, a combined frequency distribution vs. ASTM grain size number chart is presented in Fig. 4.7.

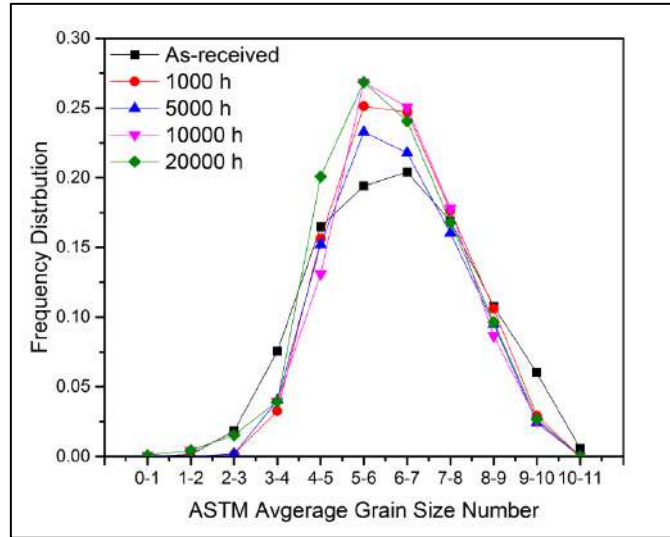


Fig. 4.7 — Comparing the frequency distribution of different aged specimens vs. ASTM grain size number.

The frequency distribution chart appreciates that there is in general no much difference in the overall grain size of the aged alloy and the grain size is reasonably constant. A closer look at the frequency distribution chart reveals that there has been a grain growth with increasing aging duration at 1023 K (750 °C), but the grain growth has resulted in a uniform distribution of grain. There is some grain growth as seen from (Fig. 4.2 – 4.6), and the distribution of grain size plot becomes broader. The sharpening of the peak in the grain size distribution chart of Fig. 4.3 (b) through Fig. 4.6 (b) is attributed to the Zener pinning. These finer particles (Fig. 4.3 (b)) exerts a pinning pressure and thus counteracting the driving force for boundary movement, which is very important to the grain growth process. The notion that there is some grain growth in the alloy with the aging time cannot be ignored, but the distribution of the overall grain size is still in the range of ASTM numbers 4 - 6. The property of this material to constrain the grain growth even after an aging durations of 20000 hours is a strong point that attracted the designers to consider this material toward high-temperature applications.

4.3 Morphological Characterization of Alloy 617 for High-Temperature Application

With the hard-earned wisdom in the field of metallurgy, it is now a well-accepted fact that the physical properties of a material are a strong function of nature, shape, size, and morphology of evolved microstructure. Thus, it is now imperative that a detail investigation of microstructural evolution in Alloy 617 has to be accomplished for a better understanding of the material behavior over long duration aging considering it as a replica of in-service conditions. For this, as-received and aged specimens are explored for their precipitate evolutions, and the associated elemental analysis is undertaken. The elemental analysis has been undertaken to understand the composition of the evolving precipitates over aging and also to get an idea of the preventive measures to be taken to impede the formation of some detrimental phases in the material.

Fig. 4.8 reveals the SEM image and the corresponding elemental analysis of the alloy in the as-received condition being only in solution annealed state. In the as-received alloy, the micrographs show two different kinds of precipitates as shown in Fig. 4.8 (a) and marked as A and B. The one being populated near and on the grain boundaries and other lying inside the matrix. The point marked by A in the microstructure is globular in shape, and point B is block shape. Moving further to elucidate the chemical composition using EDS analysis, it is confirmed that globular shaped precipitates are Cr, Mo, and Co-rich and therefore expected to be $(\text{Cr, Mo})_{23}\text{C}_6$ carbides and the block-shaped particles are Ti-rich and thus most probably are $\text{Ti}(\text{C, N})$ carbonitrides as can be seen in the Fig. 4.8 (b) and Fig. 4.8 (c), respectively.

These primary carbides are the carbides which are somehow got interlocked at the grain boundaries during their migration in annealing treatment. These precipitates show their presence in serrated grain boundaries often seen in Fig. 4.2. Though, the

formation of serrated grain boundaries is still a field of open debate and has not yet reached a consensus [85]. But, various research groups have upvoted the triggering of the serrated grain boundaries by the discontinuous segregation of Cr and C atoms at the grain boundaries in the interest of releasing the excessive elastic strain energy [86-88]. These low energy serrated boundaries often resist creep deformation inside the material.

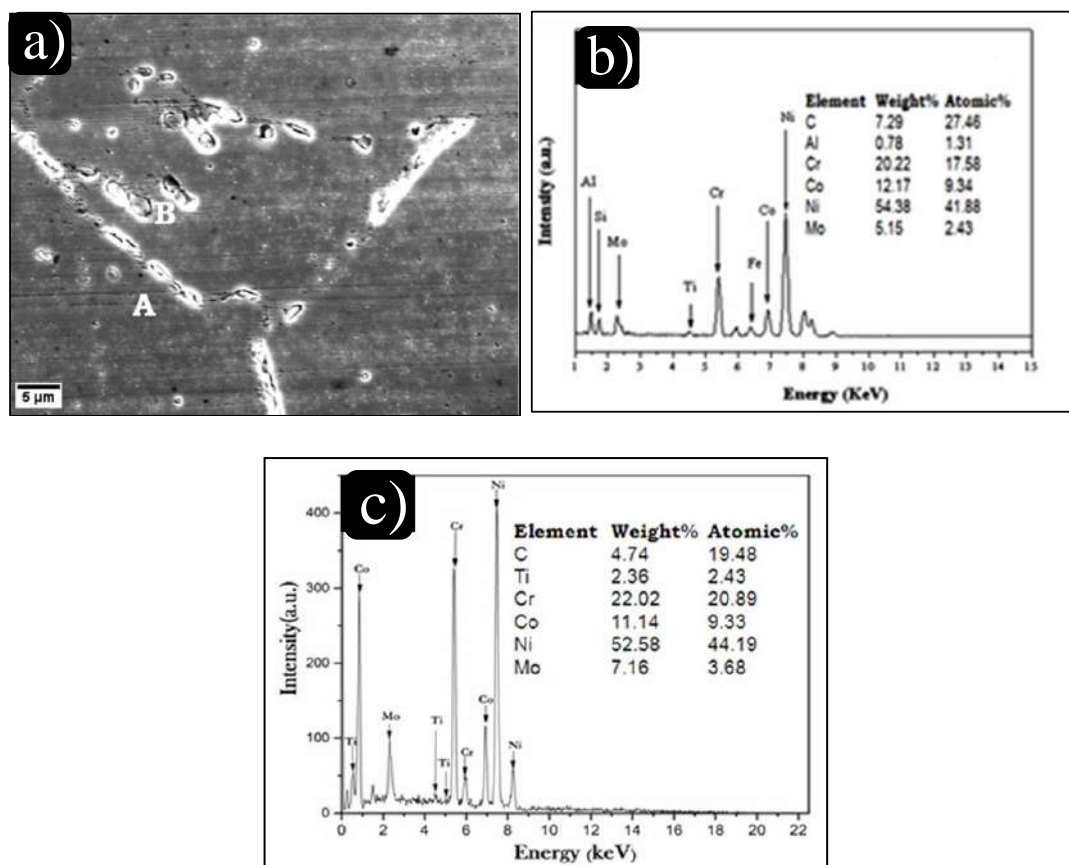


Fig. 4.8 — SEM images unveiling the effect of aging duration on precipitate evolution in Alloy 617: (a) SEM micrograph of as-received alloy; (b) the EDS results of A point in (a); (c) the EDS results of B point in (a).

The SEM image and the corresponding elemental analysis of the 1000 hours aged sample is shown in Fig. 4.9. After aging, the material produced plenty of carbides near and inside the grain boundary as can be seen from Fig. 4.9 (a). This characteristic of releasing carbides in the matrix spontaneously even after 1000 hours of aging is an indication that the Alloy 617 has a propensity towards aging-induced microstructural evolution. The spontaneous evolution of microstructures is in conformity with other

reports published earlier by various other research groups [22, 89]. The corresponding EDS spectrum is shown in Fig. 4.9 (b). The elemental analysis indicates that the precipitates are Cr, Mo, and Co-rich and therefore expected to be $(\text{Cr, Mo})_{23}\text{C}_6$ carbides.

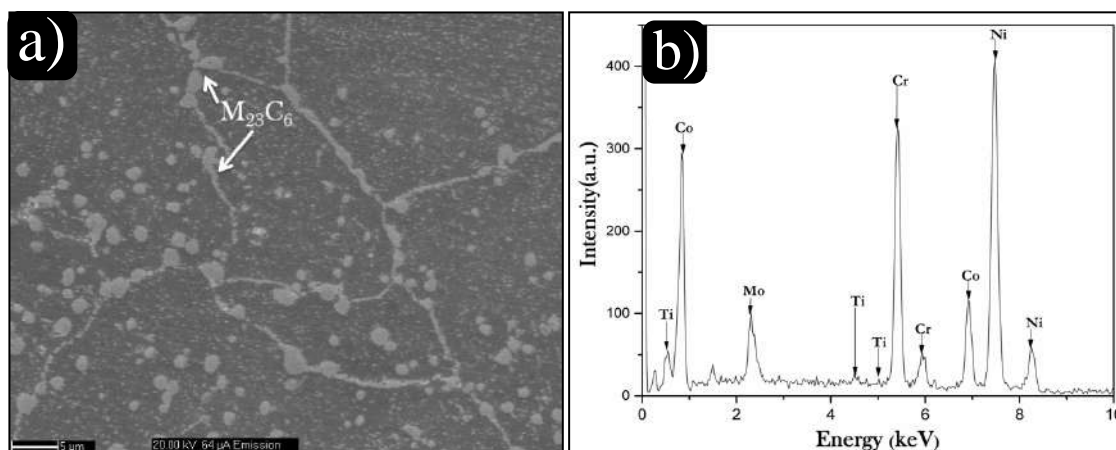


Fig. 4.9 — SEM images unveiling the effect of aging duration on precipitate evolution in Alloy 617: (a) SEM micrograph of 1000 h aged alloy; (b) the EDS spectrum corresponding to Cr_{23}C_6 .

The SEM image and the corresponding elemental analysis of 5000 hours aged sample is shown in Fig. 4.10. The SEM of 5000 hours aged sample shows plenty of carbides near and inside the grain boundary. $\text{Ti}(\text{C, N})$ as block-shaped particles with an average size of 5 μm can be seen inside the grains as shown in Fig. 4.10 (a). The presence of $\text{Ti}(\text{C, N})$ has been reported by many researchers in Ni-based superalloys for high-temperature and is consistent with our result [90, 91]. The corresponding EDS spectrum in Fig. 4.10 (b) confirms the precipitates to be rich in Ti (carbon and nitrogen are excluded from the quantitative analysis) and hence indicate toward the $\text{Ti}(\text{C, N})$. The presence of $\text{Ti}(\text{C, N})$ helps in pinning the dislocation motion and also render resistance to grain growth [92, 93].

The bright colour $\text{Ti}(\text{C, N})$ precipitates are located preferentially near the grain boundaries. Primary TiC may also contain some amounts of nitrogen and can form carbides and nitrides which have cubic structures with a lattice parameter of $a = 0.43$ -

0.47 and $a = 0.424$ nm, respectively [94]. Thus, it seems more accurate and acceptable to represent and refer it to carbo-nitrides $\text{Ti}(\text{C}, \text{N})$. These carbonitride precipitates serve and provide an active site for the crack initiation and cause material failure. Furthermore, it is well known that Alloy 617 is a solid solution strengthened alloy, removal of the Cr content and its participation in the formation of $(\text{Cr})_{23}\text{C}_6$ owing to the formation and degeneration of $\text{Ti}(\text{C}, \text{N})$ near the grain boundaries could play a detrimental role in the strengthening of the alloy. These precipitates are not always troublesome, but on certain occasions, help in enhancing the hardness of the matrix experienced during the aging treatments. But, in spite of their benefits, they mostly play a negative role by assisting the formation of voids and cracks along the grain boundaries causing the reduction in the creep rupture life.

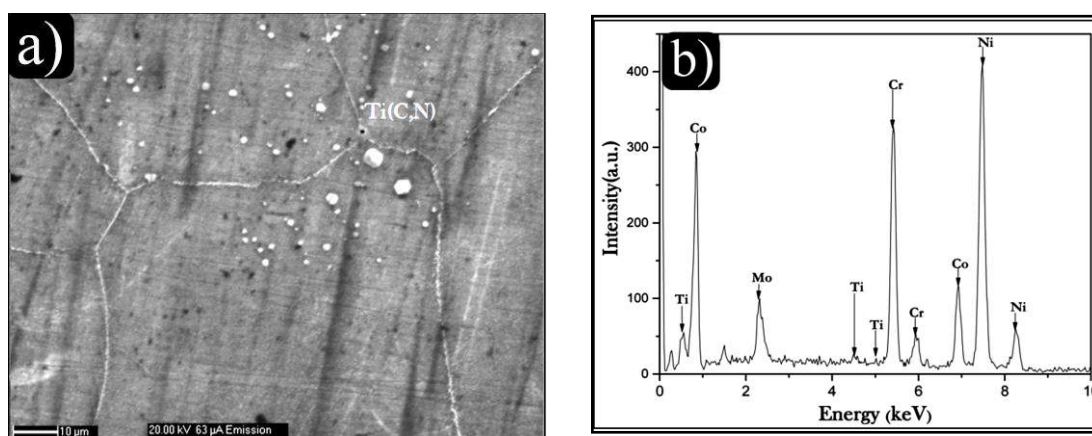


Fig. 4.10 — SEM images unveiling the effect of aging duration on precipitate evolution in Alloy 617: (a) SEM micrograph of 5000 h aged alloy; (b) the EDS spectrum corresponding to $\text{Ti}(\text{C}, \text{N})$.

Fig. 4.11 shows the SEM image and the corresponding elemental analysis of 10000 hours aged material. After aging for 10000 hours, it is clearly seen that the precipitates are populated mainly at the grain boundaries as shown in Fig. 4.11 (a). The corresponding EDS spectrum in Fig. 4.11 (b) confirms the precipitates are Cr and Mo-rich and therefore expected to be $(\text{Cr}, \text{Mo})_{23}\text{C}_6$ carbides of the Cr_{23}C_6 type. These carbides have clumped together to form small groups.

Exciting features that can be seen from the micrographs are its homogenous precipitations, intensive precipitations near the grain boundaries, and precipitates growth compared to 5000 hours aged samples. Similar to those fine precipitates around the TiN particles at shorter times, carbide growth during the aging process likely created dislocations which provided nucleation sites for new precipitation during subsequent aging.

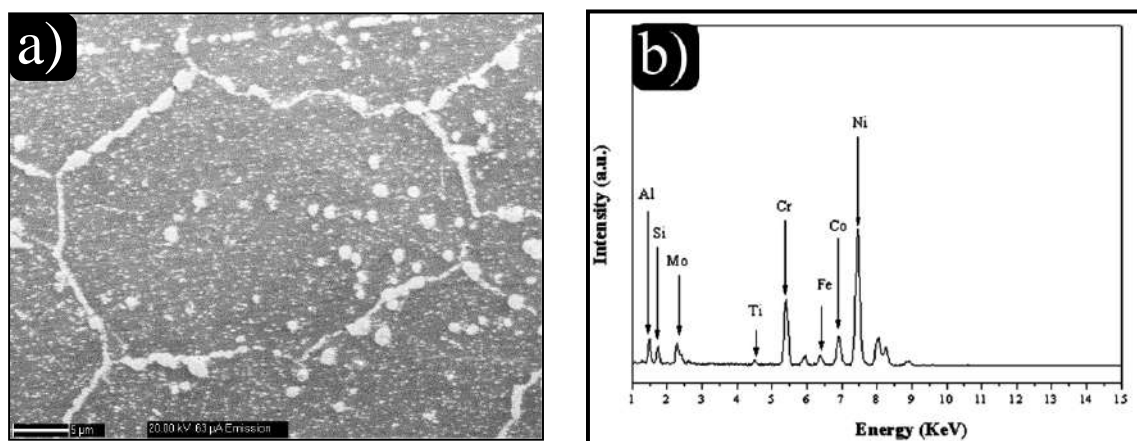


Fig. 4.11 — SEM images unveiling the effect of aging duration on precipitate evolution in Alloy 617: (a) SEM micrograph of 10000 h aged alloy; (b) the EDS spectrum corresponding to Cr_{23}C_6 .

SEM image of 20000 hours aged material is shown in Fig. 4.12. After aging for 20000 hours, it can be clearly seen that extensive carbide precipitates have completely occupied the grain boundaries. The corresponding EDS spectrum in Fig. 4.12 (b) substantially re-confirms the precipitates to be rich in Cr and Mo and therefore expected to be $(\text{Cr}, \text{Mo})_{23}\text{C}_6$ carbides of the Cr_{23}C_6 type.

The micrograph of 20000 hours aged specimen is again impressive due to its precipitation profile. The particles instead of coarsening due to aging, as observed in other superalloys [95], here in Alloy 617 have gone fine in structures. The unexpected decline in the size of precipitates is a matter of curiosity and, indeed, a driving force for further investigation in this alloy.

As opposed to coarsening, precipitations size shows a fine distribution in the matrix as shown in Fig. 4.12. The decline in size, yet keeping the same composition of the precipitates as confirmed from the EDS spectrum dictates that a new set of precipitates might have evolved and the previous larger precipitates might have been engulfed within the matrix due to aging. At this stage, no solid confirmation can be given owing to a lack of experimental characterization. Bright light can be thrown on this issue only after obtaining a clear picture from the TEM investigations.

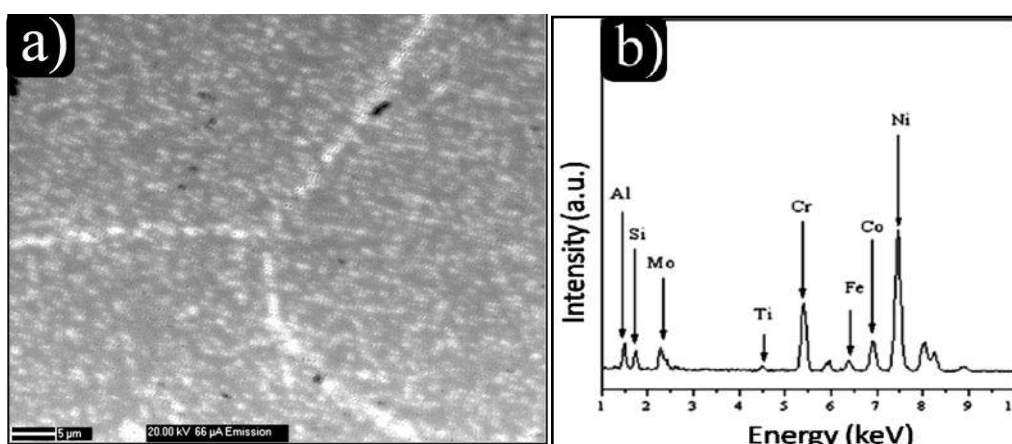


Fig. 4.12 — SEM images unveiling the effect of aging duration on precipitate evolution in Alloy 617: (a) SEM micrograph of 20000 h aged alloy; (b) the EDS spectrum corresponding to Cr₂₃C₆.

4.4 Quantifying the precipitates of Alloy 617

The nature and the extent of precipitations have been already discussed by and large in the previous section. From the earned wisdom it is well established that size, nature, and type of precipitates play a significant role in determining the crack initiation energy of the alloy. Quantification of such an important parameter is imperative for a better understanding of the structural integrity and functionality of the components during in-service [96, 97]. A few interesting facts about the nature of precipitates inside the alloy 617 have been tabulated in table 4.1. The precipitate size in the column average size shows an anomalous trend of the particle growth. The average precipitate size of 1.21 μm in the as-received is an indication of solution annealed precipitates which got stuck

during the annealing and got interlocked at the grain boundaries. Initial aging for 1000 hours shows a uniform precipitate of size distributed across the grain boundaries as evident from the large precipitate counts in table 4.1. Further aging increases the precipitate size also evident from Fig. 4.10 and 4.11. There is an anomaly in the 20000 hours aging where the precipitates instead of coarsening in size, they mark a reduction in size as also seen in table 4.1.

Table 4.1 Quantified precipitates of the indigenous Alloy 617 in the different heat-treated conditions.

| Conditions (h) | Counts | Total Area (μm^2) | Average Size | % Area |
|----------------|--------|--------------------------------|--------------|--------|
| As-received | 87 | 105.74 | 1.21 | 6.15 |
| 1000 | 309 | 183.30 | 0.593 | 6.44 |
| 5000 | 66 | 90.23 | 1.367 | 0.803 |
| 10000 | 107 | 199.37 | 1.863 | 1.40 |
| 20000 | 351 | 370.87 | 1.057 | 13.21 |

4.5 TEM Study of As-received and Aged Alloy 617

The microstructural features for the as-received and aged alloys have further been investigated with the transmission electron microscopy.

TEM study of as-received condition reveals the presence of two types of carbides, namely the Mo-rich M_2C and the Cr-rich M_{23}C_6 , as shown in Fig. 4.13 and Fig. 4.14, respectively. Fig. 4.13 (a) & (b) show the bright-field transmission electron microscopy (TEM) image of as-received alloy with precipitates and the corresponding SAED pattern respectively. The corresponding EDS spectrum, as shown in Fig. 4.13 (c) confirms the precipitate to be rich in Mo and Ti. The SAED analysis and the associated EDS spectra confirm the precipitate to be of M_2C type $((\text{Mo}, \text{Ti})_2\text{C})$.

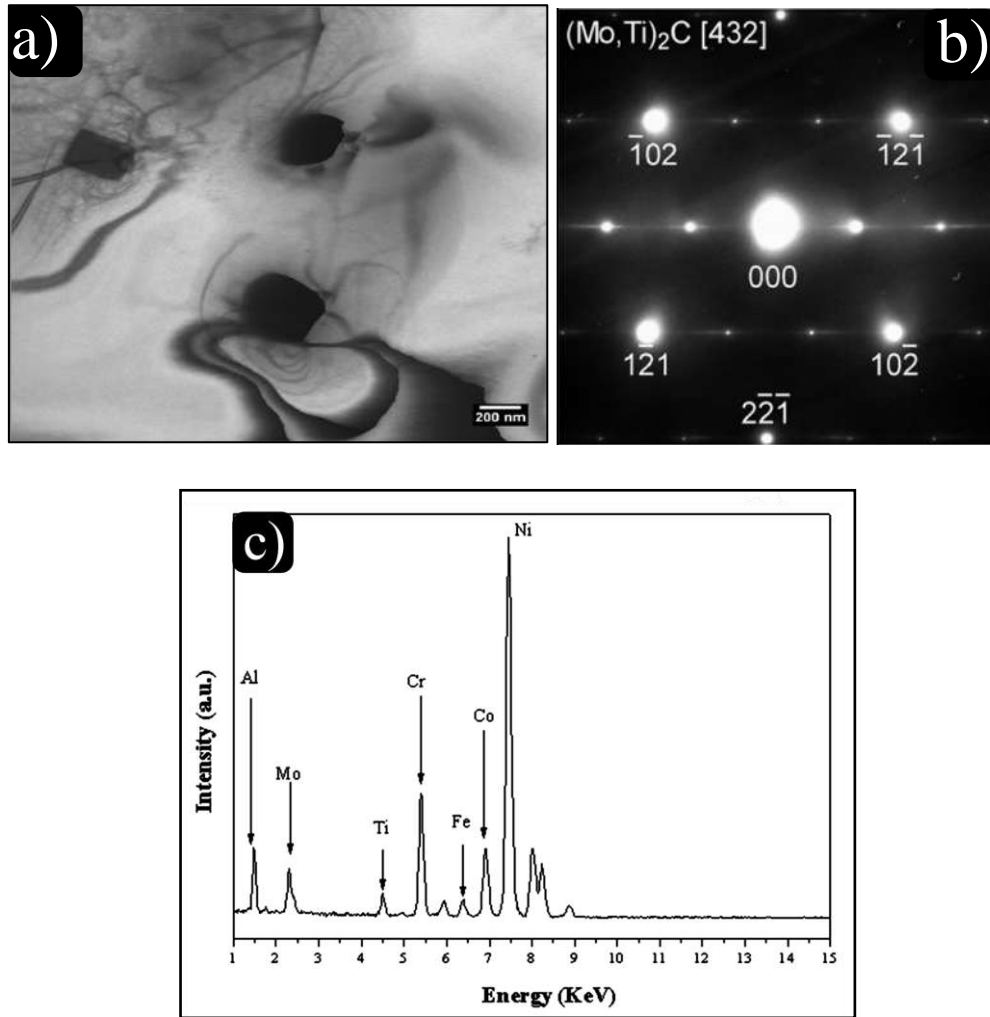


Fig. 4.13 — (a) Bright-field TEM image of as-received Alloy 617 showing M₂C carbide in Alloy 617 (b) SAED pattern correspond to M₂C type (zone axis [432]); (c) The corresponding EDS spectrum confirms Mo and Ti-rich precipitates.

Fig. 4.14 (a) to Fig. 4.14 (b) shows the TEM micrograph and the SAED pattern from precipitates of the type M₂₃C₆, respectively. The TEM investigations of these precipitates in the Alloy 617 were found to be Cr-rich M₂₃C₆ type. These results were also in conformity with the result obtained by Mankins et al. [15]. The SAED pattern is shown in Fig. 4.14 (b). The EDS spectrum corresponding to the SAED pattern is shown in Fig. 4.14 (c) and they confirm that precipitates are rich in Cr and Mo and are of the form (Cr, Mo)₂₃C₆.

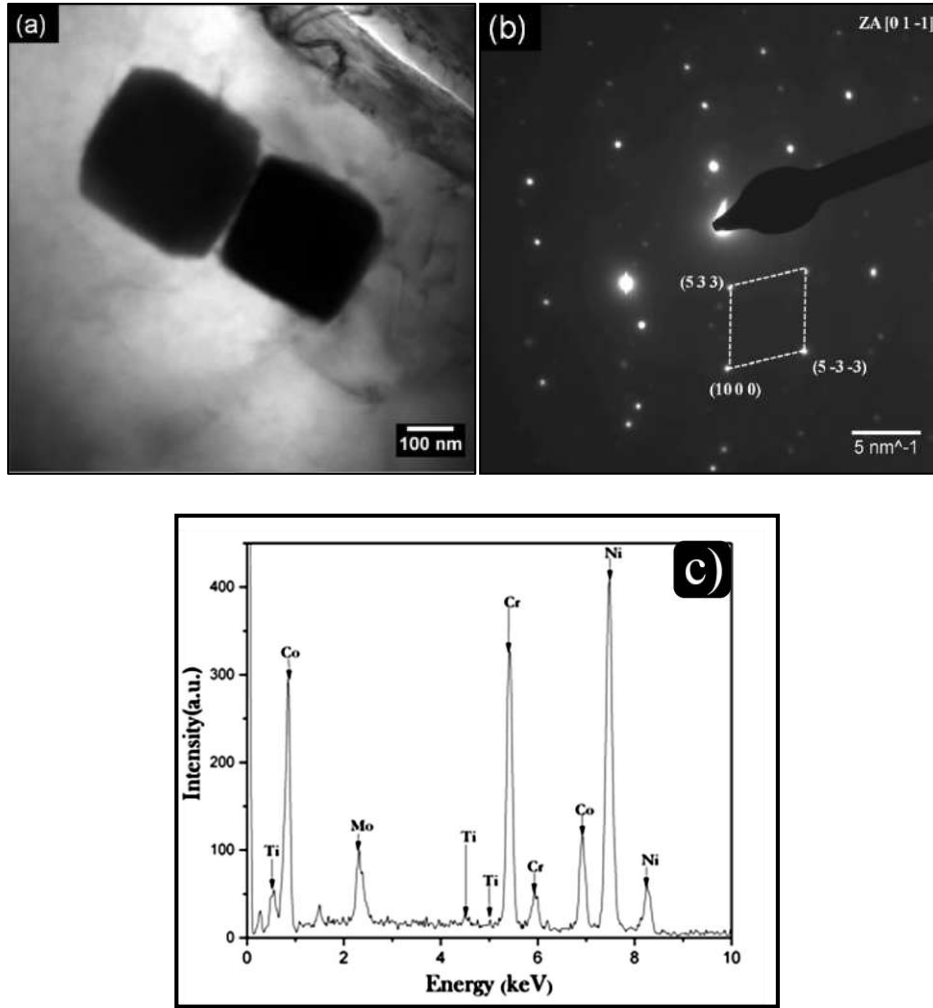


Fig. 4.14 — (a) Bright-field TEM image of as-received Alloy 617 showing $M_{23}C_6$ carbides (b) SAED pattern correspond to $M_{23}C_6$ type (zone axis [011]); (c) The corresponding EDS spectrum confirms $M_{23}C_6$ type to be rich in $(Cr, Mo)_{23}C_6$.

The TEM results after 1000 hours of aging treatment are shown in Fig. 4.15. The bright-field TEM image shown in Fig. 4.15 (a) reveals the presence of $Ni_3(Ti, Al)$ precipitates, commonly known as the γ' phase. The dominant feature during the short-term aging of 1000 hours was found to be the fine and ordered γ' precipitates are nucleating on the planes with zone axis ([0 1 1]). For the 1000 hours aging duration, depending on the nucleation site, the size of the fine spherical γ' precipitates was on a range from ~ 50-70 nm. A similar kind of observation has also been reported in work carried out by Krishna et al. [98]. The corresponding EDS spectrum, as shown in Fig. 4.15 (c) confirms the precipitate to be rich in Ni, Al, and Ti are of type $Ni_3(Al, Ti)$.

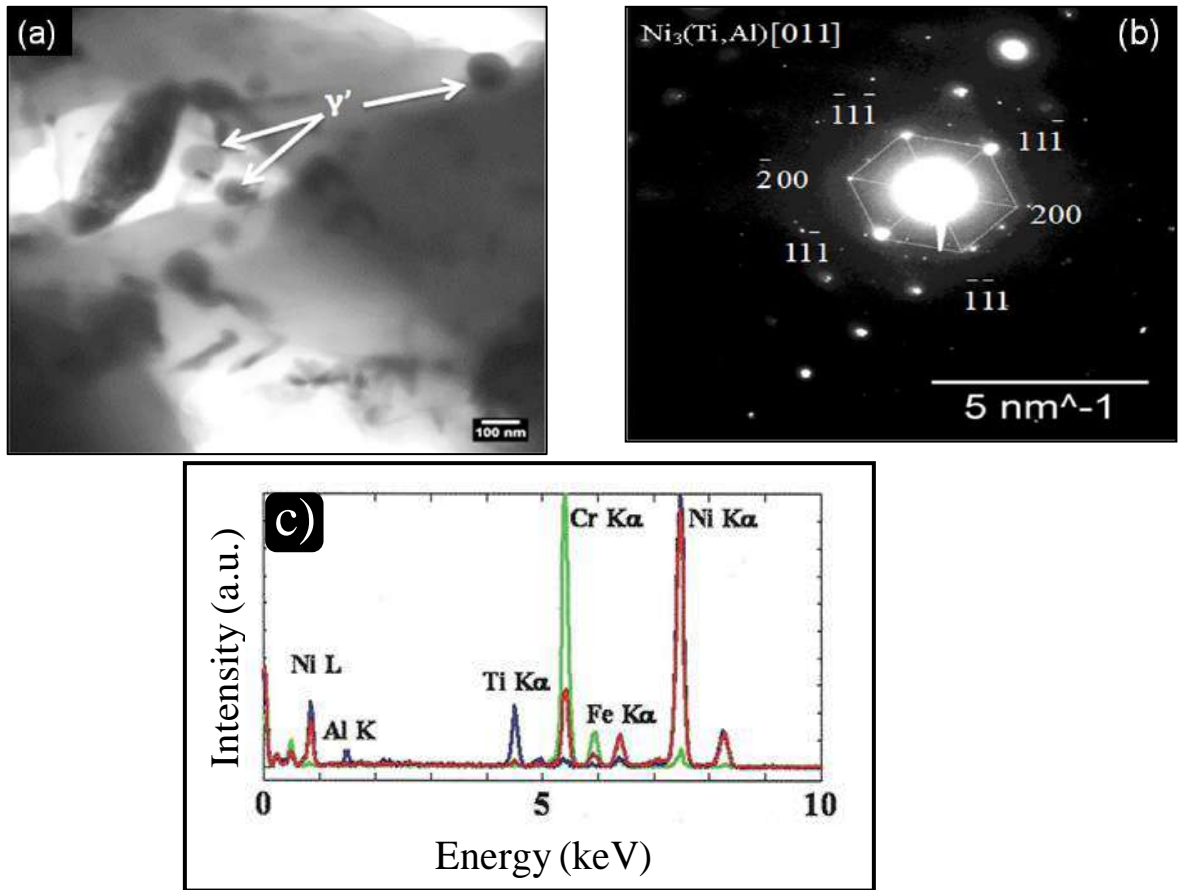


Fig. 4.15 — Bright-field TEM images and SAED pattern of γ' precipitate in Alloy 617 aged at 1023 K: (a) TEM image after 1000 h of aging showing spherical precipitates of γ' phase commonly known as $\text{Ni}_3(\text{Ti}, \text{Al})$; (b) SAED pattern correspond to γ' phase (zone axis $[011]$); (c) The corresponding EDS spectrum confirms γ' phase to be rich in Ni, Ti, Al and they correspond to $\text{Ni}_3(\text{Ti}, \text{Al})$.

The TEM results after 5000 hours of aging treatment are shown in Fig. 4.16. The morphology of γ' precipitates in 5000 and 1000 hours aged condition remains unaltered bearing the same spherical nature. Marginal growth in the size $\sim 80 - 100 \text{ nm}$ has been noticed (Fig. 4.16 (a)) w.r.to 1000 hours aged material. It is well appreciated that the presence of γ' precipitates in the matrix of an aged alloy of this material plays a crucial role in imparting strength at higher temperatures [99]. It can be concluded from the TEM investigations that the morphology of γ' precipitates hardly changes during the aging treatments. However, there are indications that it only grows in size due to thermal aging, but to a limited extent. It could be appreciated that even this marginal

change in the precipitate size may have a significant influence on the deformation characteristics of this material. The SAED pattern has validated the TEM results, and EDS spectrum shown in Fig. 4.16 (c) confirming the elemental composition of γ' to be rich in Ni, Al, and Ti and most probably of the type $\text{Ni}_3(\text{Al}, \text{Ti})$.

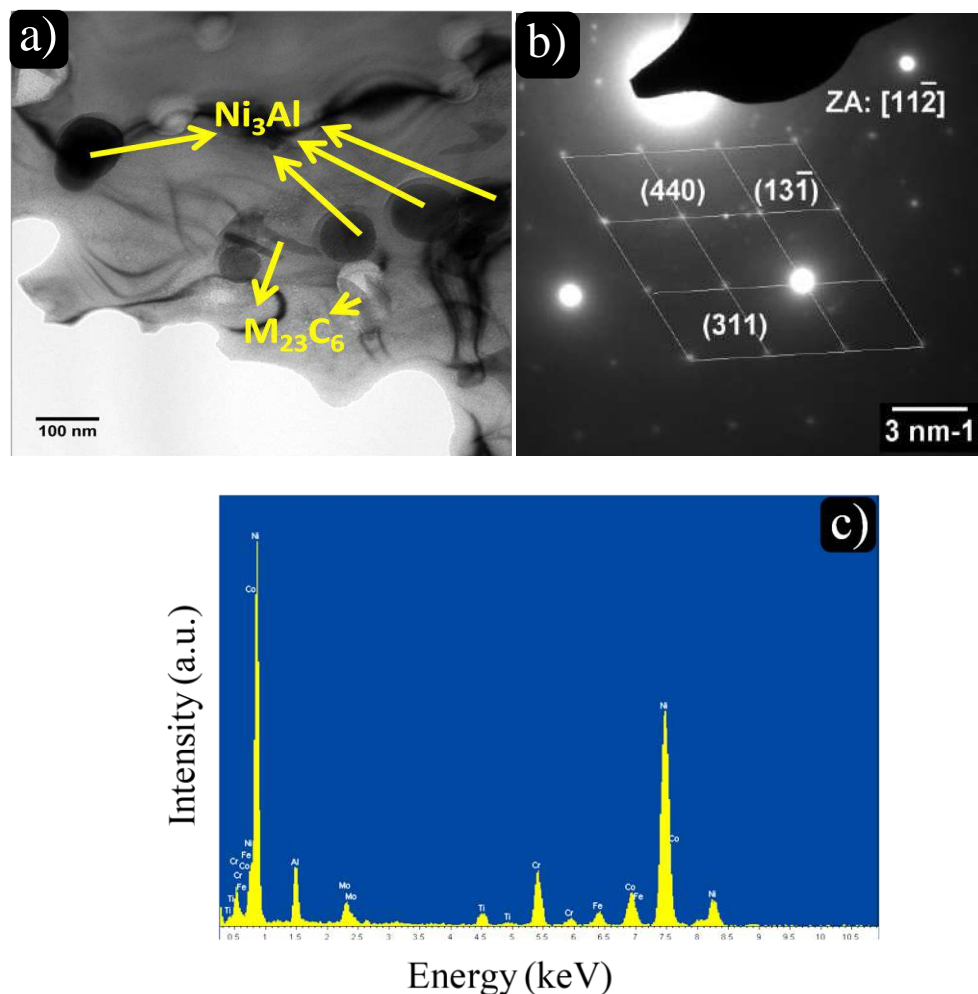


Fig. 4.16 — Bright-field TEM images and SAED pattern of Coherent γ' precipitate and M_{23}C_6 in Alloy 617 aged at 1023 K: (a) TEM image after 5000 h of aging showing spherical precipitates of γ' phase commonly known as $\text{Ni}_3(\text{Ti}, \text{Al})$ and M_{23}C_6 ; (b) SAED pattern correspond to γ' phase (zone axis $[0\ 1\ 1]$); (c) The corresponding EDS spectrum confirms γ' phase to be rich in Ni, Al, and Ti and they correspond to $\text{Ni}_3(\text{Ti}, \text{Al})$ and M_{23}C_6 to be rich in Cr, Mo, and they correspond to $(\text{Cr}, \text{Mo})_{23}\text{C}_6$.

Fig. 4.17 shows the TEM images of γ' precipitates after the 10000 hours of aging. The morphology of γ' precipitates in 1000 hours aged condition and γ' precipitates even after aging for 10000 hour bears the same spherical nature. To appreciate the aging, marginal growth in the size $\sim 80\text{-}110\text{ nm}$ has been noticed in Fig.

4.17 (a) w.r.to 1000 hours aged material. The presence of γ' precipitates in the matrix of the aged alloy of this material plays a crucial role in imparting strength at higher temperatures [99]. It is further concluded from the TEM investigations that the morphology of γ' precipitates hardly changes during the aging treatments. However, there are indications that it only grows in size due to thermal aging, but to a limited extent. The importance of even a minor growth in size of these precipitates is well supported by a significant change in the deformation mechanism of this material. The type of precipitates has been validated by the SAED pattern, as shown in Fig. 4.17 (b). The corresponding EDS spectrum shown in Fig.4.17 (c) has confirmed the elemental composition of γ' to be Ni-rich and of the type $\text{Ni}_3(\text{Al}, \text{Ti})$.

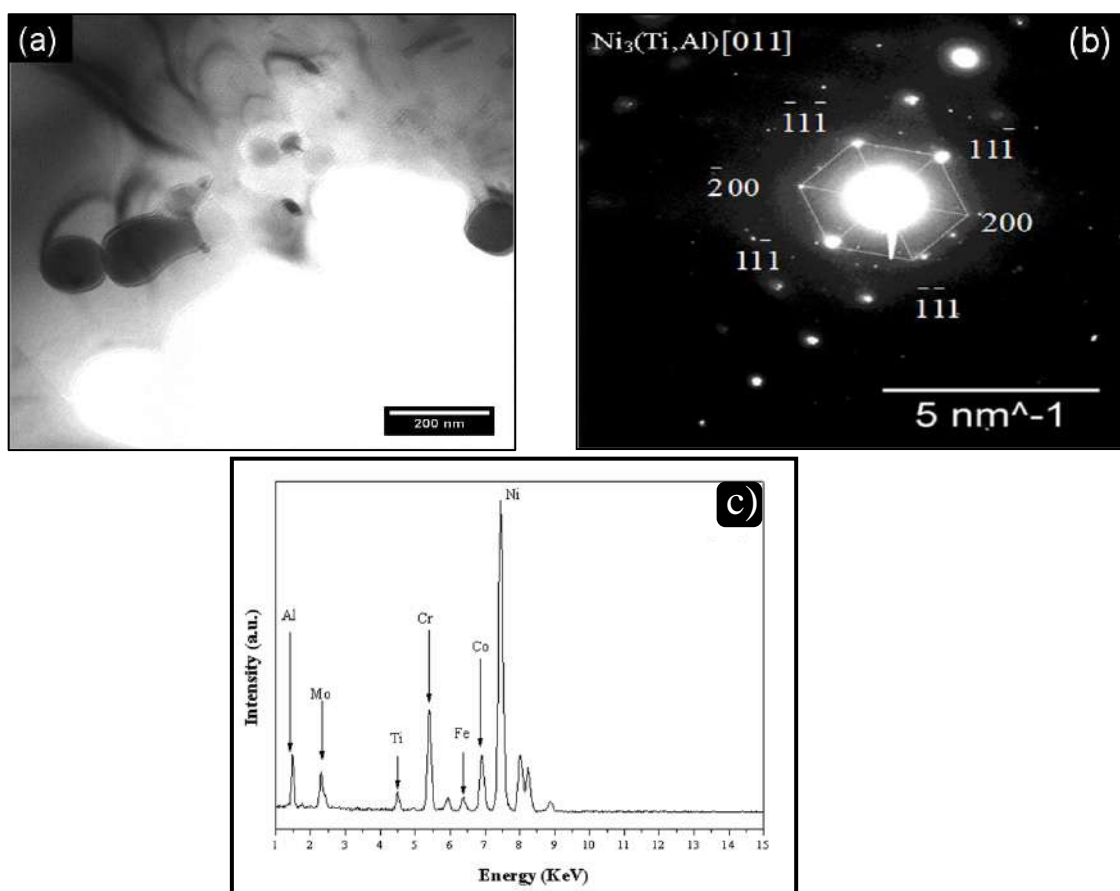


Fig. 4.17 — Bright-field TEM images and SAED pattern of γ' precipitate in Alloy 617 aged at 1023 K: (a) TEM image after 10000 h of aging showing spherical precipitates of γ' ; (b) SAED pattern correspond to γ' phase (zone axis $[0\ 1\ 1]$); (c) The corresponding EDS spectrum confirms γ' phase to be rich in Ni, Al, and Ti and they correspond to $\text{Ni}_3(\text{Ti}, \text{Al})$.

Not only γ' has evolved during the course of aging, but also the carbides have sufficiently grown enough due to aging treatment. TEM results of thermally aged specimens for 10000 hours have also shown the $M_{23}C_6$ precipitates of size 70-80 nm as shown in Fig. 4.18 (a). SAED pattern along the $[011]$ zone axis as shown in Fig. 4.18 (b) corresponds to the $M_{23}C_6$ type. The corresponding EDS spectrum shown in Fig. 4.18 (c) has confirmed the elemental composition of the $M_{23}C_6$ to be Cr-rich $Cr_{23}C_6$. The elemental composition (by wt pct) around the $M_{23}C_6$ is shown in Table 4.2.

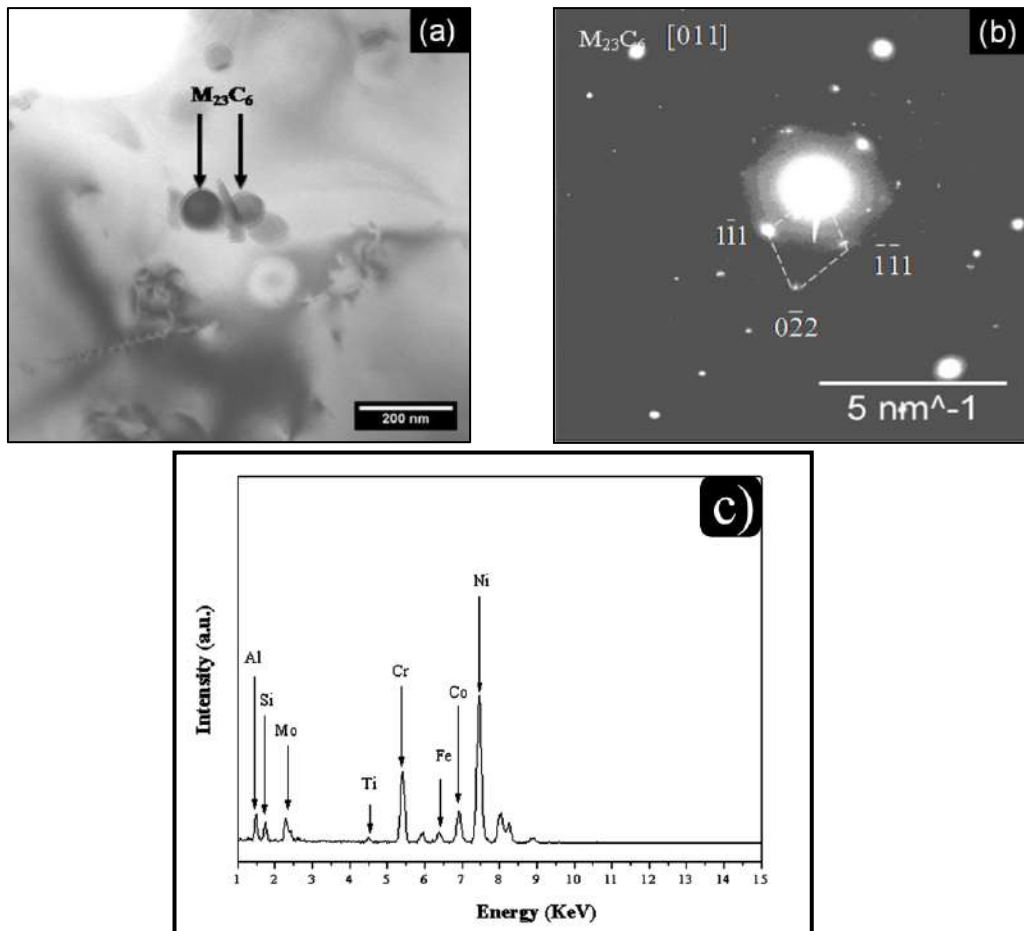


Fig. 4.18 — Bright-field TEM image and SAED pattern of Alloy 617 aged at 1023 K for 10000 h: (a) Bright-field TEM image showing precipitates of size 80-100 nm (b) SAED pattern confirming that they correspond to $M_{23}C_6$; (c) The corresponding EDS spectrum confirms $M_{23}C_6$ to be rich in Cr, Mo and they correspond to $(Cr, Mo)_{23}C_6$.

Table 4.2 Local (wt pct) composition variation of elements in the matrix and around $M_{23}C_6$ (10000 hours aged).

| | Ni | Cr | Co | Mo | Fe | Al | Ti |
|----------------------|-------|-------|-------|------|------|------|------|
| Grain interior | 49.07 | 22.1 | 11.6 | 9.4 | 0.12 | 1.2 | 0.4 |
| Close to $M_{23}C_6$ | 50.21 | 23.49 | 13.46 | 8.22 | 2.28 | 1.64 | 0.70 |

It is interesting to look at table 4.2, illustrating the weight (wt) pct composition of elements near the carbide precipitates. A local enrichment in pct compositions of major carbide forming elements can be seen in the table. Due to a higher propensity toward the formation of carbides under the influence of aging treatment, major alloying element viz: Cr and Mo which were supposed to provide a solid solution strengthening are now playing a role in reducing the solid solution strength by their active participation in the formation of carbides. Though, carbides can offer a small contribution towards high-temperature strength (due to its small size, it can pin the dislocation and cause an increase in strength of the material), but its coarsening ability under the influence of aging makes it a notorious agent favouring the grain boundary embrittlement rather than to strengthen the grain boundary.

It is also interesting to note the along with γ' and carbides another precipitate was also seen under TEM and was confirmed to be Ni_3Si shown in Fig. 4.19. Bright-field TEM image shown in Fig. 4.19 (a) of the alloy aged for 10000 hours shows some coarser precipitates of the size 110-120 nm. From the SAED analysis, it can be inferred that the precipitates are rich in Si. Tokunaga et al. [93] have reported a similar observation of an intermetallic of Ni-Si system in Ni-Si-B ternary alloys. Crack-tip dislocations and fracture behaviour of Ni_3Si and Ni_3Al system have been reported by Yoo and group [100]. Very few reports have been published in this direction stating Ni_3Si presence in superalloys; we though found out Ni_3Si and precipitates have been confirmed from combined SAED pattern as shown in Fig. 4.19 (b) and corresponding

EDS spectrum shown in Fig. 4.19 (c), a suitable explanation for its origin and its role in Alloy 617 performances can only be said in due course of time with the availability of more TEM results.

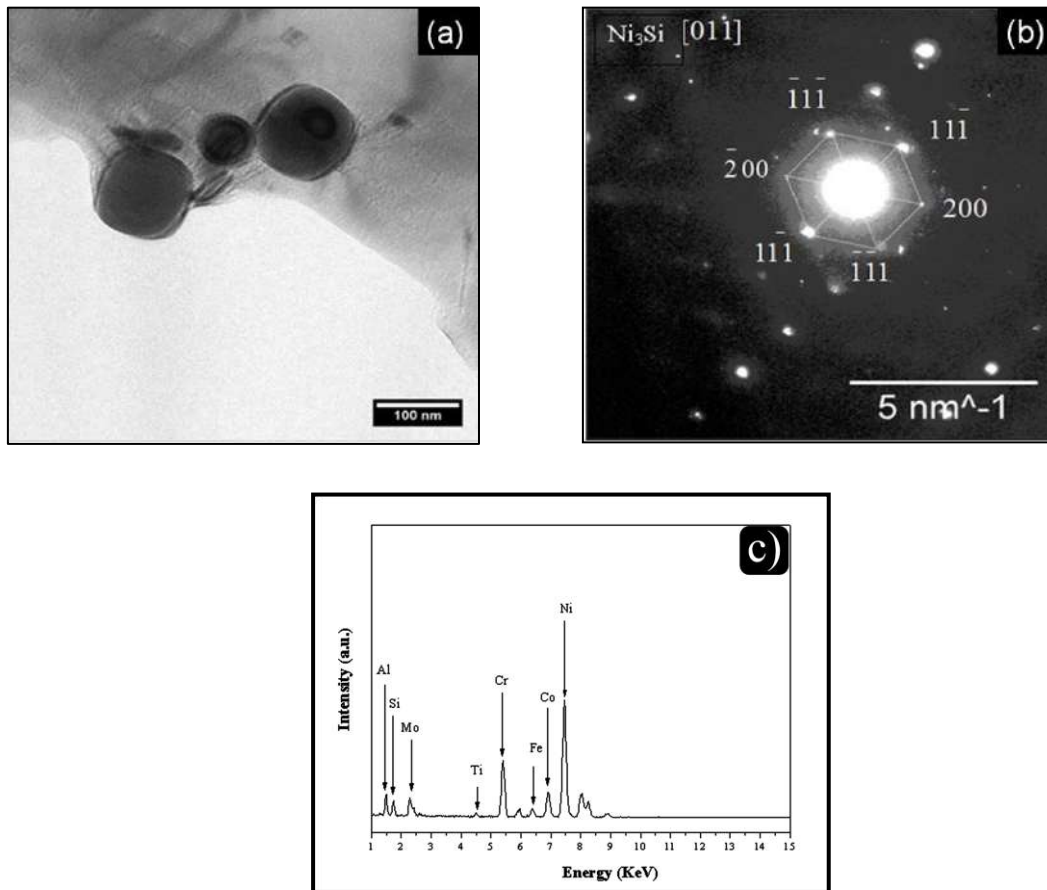


Fig. 4.19 — Bright-field TEM image and SAED pattern of Alloy 617 aged at 1023 K for 10000 h: (a) Bright-field TEM image showing precipitates of size ~ 110 -120 nm (b) Corresponding SAED pattern (c) The corresponding EDS spectrum confirms precipitates to be rich in Ni and Si and they correspond to Ni_3Si .

TEM images of 20000 hours aged material is shown in Fig. 4.20. There are few new precipitates in this aged condition which are quite finer and smaller than the previous precipitates found in the other aged conditions.

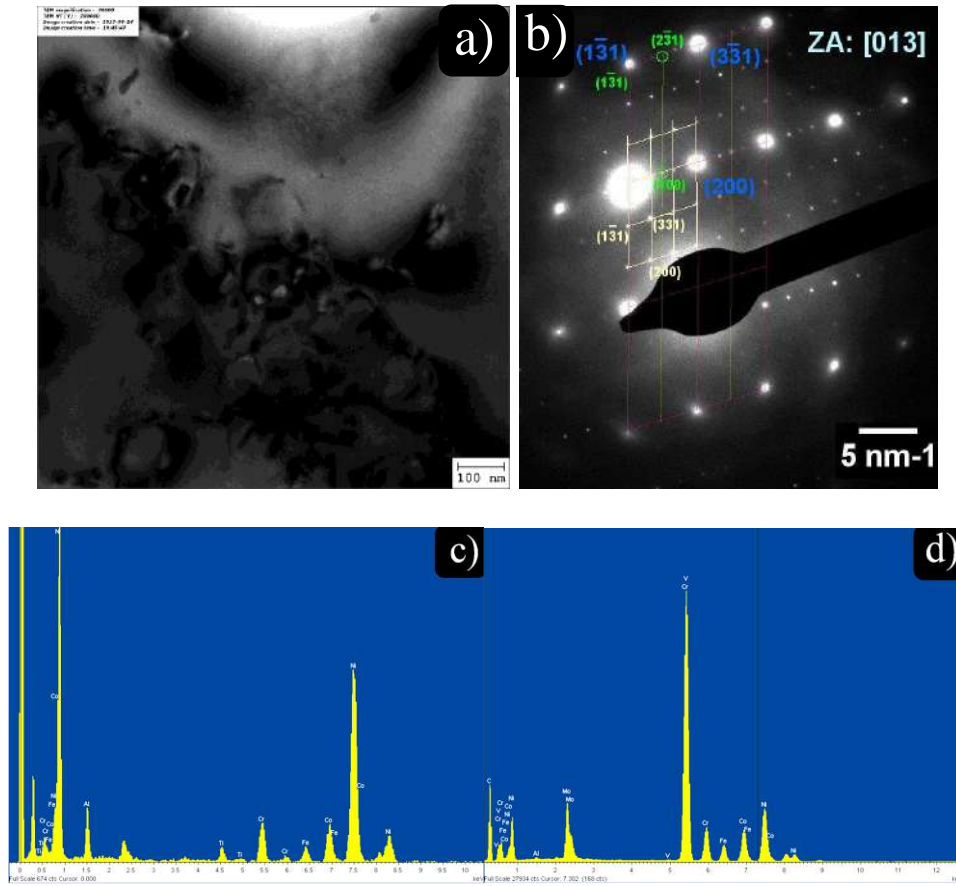


Fig. 4.20 — (a) Bright-field image of alloy 617 aged for 20000 h showing $\text{Ni}_3(\text{Ti, Al})$ and M_{23}C_6 precipitates in a gamma matrix. (b) SADP for matrix (indexed in blue), $\text{Ni}_3(\text{Ti, Al})$ (indexed in green) and M_{23}C_6 (indexed in sandal) along the zone axis [013]; (c) EDS spectra indicate $\text{Ni}_3(\text{Ti, Al})$; (d) EDS spectra indicate Cr rich M_{23}C_6 .

Further observation of the TEM results reveals some finer precipitates of size ~15 to 20 nm, as shown in Fig. 4.21. However, the exact types of these precipitates could not be identified within the present scope of this thesis work.

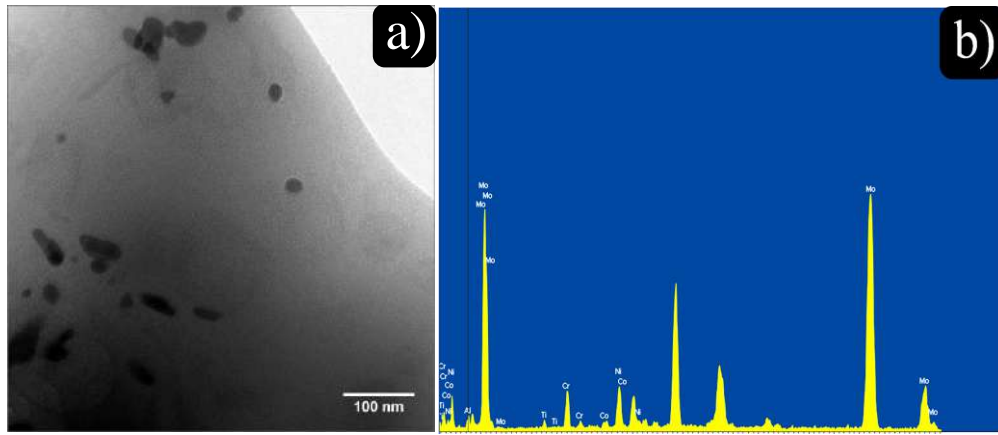


Fig. 4.21 (a) Bright-field image of alloy 617 aged for 20000 h showing unidentified finer precipitates; (b) EDS spectrum indicating they are Mo-rich phase.

Though to our knowledge, literature data to this end is silent, and there are a few research reports on long term aging microstructure of Alloy 617 [101, 102], which has not reported the precipitates over 20000 hours of aging. It may be noted that Alloy 718 bears similar composition with our Alloy 617 but fine precipitates present in short duration of aging at higher temperature is (Ni_3Nb), which in our case can be ruled out as we have found Mo-rich precipitates as identified by the EDS spectra as shown in Fig. 4.21 (b). Thus, it could be inferred that this finer precipitates, as observed after 20000 hours aging at 1023 K (750 °C) is Mo-rich compound which needs further investigations. However, a further investigation in the identification of these finer precipitates and a study on their influence on the deformation and fracture properties is recommended at this present state of this thesis work.

4.6 Summary

A detailed microstructural characterization of Alloy 617 has been accomplished both in as-received and in aged condition. From the above results, it is now evident and clear that in this material, the overall grain size distribution during the entire aging duration remains almost constant. Though a slight shift in frequency distribution is clearly seen to occur during 10000-20000 hours but this seems to be a marginal shift. The grain

boundary serrations have been seen to disappear during the aging. The duplex nature of grain size distribution has also been less prominent in the aged material. The salient feature of this alloy is its propensity to release precipitates even for the aging duration of 1000 hours. The aging-induced precipitates can be categorized into two major types, namely $M_{23}C_6$ and γ' , i.e. $Ni_3(Ti, Al)$ with traces of Ni_3Si . Further, where the γ' has been precipitated randomly (within the grain and also in boundaries), the $M_{23}C_6$ has been precipitated mainly in the grain boundaries. Titanium carbonitrides $Ti(C, N)$ precipitates are mainly seen inside the grains. TEM investigation of this material has brought out significant information regarding aging-induced microstructural changes in the material. As-received material shows only Mo-rich and Cr-rich precipitates and no sign of γ' phase. Aging caused an evolution of γ' precipitates but with morphology rarely changed over the entire span of aging. Though a slight coarsening can be seen over periods of aging, but the change is insignificant. To our surprise, TEM images of 20000 hours aged material showed some very fine precipitates, other precipitates have been identified as γ' and $M_{23}C_6$, but few other precipitates with Mo-rich are also identified as elemental compositions are confirmed by EDS spectra. These very fine structures and their influence on the mechanical properties are yet to be looked in for a better understanding of this alloy over long durations of aging. This work has been listed as our future scope of the thesis.

Study of Tensile Deformation Behaviour of As-Received and Aged Alloy 617

The uniaxial tensile test is one of the most common experimental techniques to understand the deformation behaviour of engineering materials. A variety of deformation parameters which are being analyzed by tensile tests are yield stress, ultimate tensile stress, and ductility in terms of percentage elongation. Additional information on work hardening mechanisms also can be understood by analyzing the true stress-strain plots. To this end, various equations available in literature can be used depending on the material's flow characteristics. It is also well known that the microstructural constituents in a material strongly influence the deformation behaviour. Especially the types, size, shape, and distribution of the precipitates exhibit a strong influence on the yield stress, flow, and work hardening behaviour. The previous chapter has discussed the aging-induced microstructure evolution of Alloy 617 at different length scales. This chapter brings forth the results of the investigations on deformation characteristics of Alloy 617 in as received and aged conditions. The effect of the aging-induced microstructural changes on the deformation behaviour also has been discussed in detail.

5.1 Introduction

A tensile test is one of the most commonly used test methods toward assessing the deformation and flow behaviour of engineering materials and alloys under different conditions owing to its sensitivity to the micro-mechanisms of deformation under uniaxial loading condition. In a tensile test, the gross plastic flow initiates only after the yielding, and it is now well recognized that the slip in terms of gross dislocation motion is the dominant mechanism for the post-yield plastic deformation. Further, it is also

evident that most of the engineering materials get strengthened as the plastic deformation continues. This phenomenon is termed as the work hardening and is attributed to the dislocation-dislocation or dislocation–precipitate interactions as the deformation proceeds. In turn, it can be seen as obvious that the work hardening behaviour of materials is a strong function of the inherent microstructural features including the type, size, and distribution of the precipitates. To this end, an in-depth analysis of the work hardening behaviour in the post-yield domain of the deformation process is of interest to the designers. This chapter brings forth the results of the investigations on deformation characteristics of Alloy 617 in as-received and in various aged conditions. The plastic flow behaviour after different durations of aging, as evaluated by uniaxial tensile tests at ambient temperature, has been examined in terms of various existing models toward explaining the work hardening rate. Further, the work hardening behaviour of Alloy 617 has been explained in the light of microstructural evolution during various aging treatments.

5.2 Hardness of As-received and Aged Alloy 617

As a prelude to the deformation mechanism of this material under uniaxial tensile loading, hardness of the Alloy 617 in as-received and aged conditions have been studied to generate a preliminary idea about the deformation characteristics of this material.

Hardness of the Alloy 617 in its as-received and aged conditions was measured at room temperature (RT) by a Vickers hardness tester with a dwell time of 15 seconds at a 40X magnification, and the results are reported in Fig. 5.1. Though there have been usual scatter in the hardness data, a clear trend in the variation of hardness can be easily observed. In the as-received condition, alloy displayed its lowest hardness value of ~ 196 HV, whereas the aged alloy shows improved hardness even after the aging duration

of 1000 hours. The hardness of this alloy increases consistently for the aging treatments up to 5000 hours. This is attributed to the simultaneous occurrence of the $M_{23}C_6$ and γ' precipitates leading to the overall strengthening of the matrix. There is a marginal drop in hardness between the aging treatment of 5000 hours and 10000 hours. For the aging treatment from 10000 to 20000 hours, it is tending towards a marginal increase at around 250 HV.

The marginal drop in hardness between the 5000 and 10000 hours aging durations needs further attention. It is taken for granted that the matrix strength is a function of precipitate type, size, shape, and morphology. In the present circumstances, the strength of the matrix would be ultimately governed by the simultaneous presence of $M_{23}C_6$ and γ' (Ni-rich Ni_3 (Ti, Al)) precipitates, their respective sizes, shapes, and distributions. The TEM results, as reported earlier in chapter 4 and as can be seen in Fig. 4.13 to Fig. 4.21, indicate towards an aging-induced increase in size for the γ' precipitates though a marginal, along with a slight coarsening in $M_{23}C_6$. Thus, it may be concluded that the aging-induced strength of the matrix is ultimately dependent on the size and distribution of the γ' precipitates alone. After the 10000 hours aging treatment, marginal growth in the size of the γ' precipitates (from 40-70 nm to 80-110 nm) has been observed, as discussed earlier in chapter 4. It is also anticipated that unless fresh precipitates form, the increase of size would lead to higher interparticle spacing, leading to a loss of matrix strength [103]. This attributes to the marginal drop in hardness between the aging treatments of 5000 to 10000 hours.

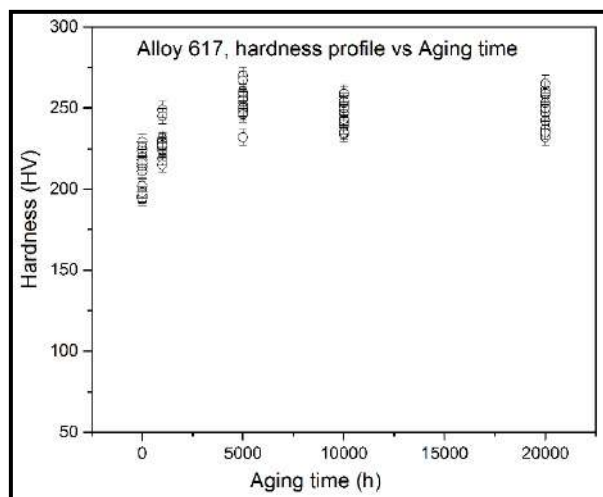


Fig. 5.1 — Profile of Hardness of the Alloy 617 with aging time.

5.3 Tensile Properties of As-received and Aged Alloy 617

The flat tensile specimens (detailed in Fig. 5.2) were fabricated as per the standard practice elaborated in ASTM standards E-8 [73]. Tensile tests were carried out in the ambient air on a floor model Hung Ta-2402 universal testing machine (UTM). Experiments were performed on specimens at room temperature 298 K (± 2 K) using a nominal strain rate of $3 \times 10^{-3} \text{ s}^{-1}$. Load–elongation-time to fail, data was recorded using the Hung Ta-2402 autographic recorder for all the different aged samples.

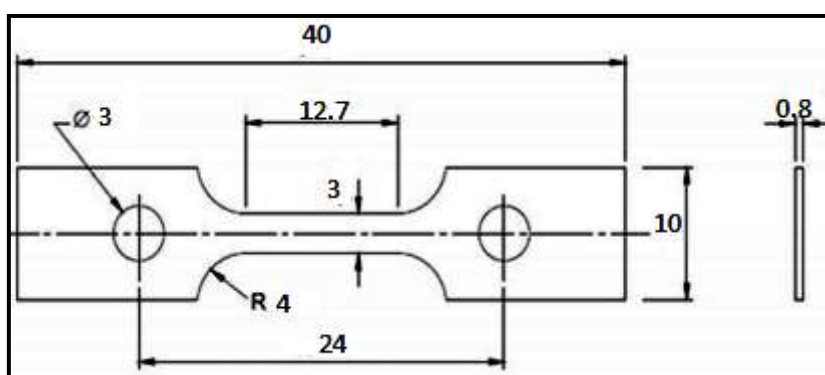


Fig. 5.2 — Schematic representation of miniaturized tensile specimen (dimensions in mm).

The Engineering stress vs. engineering strain plot and the true stress vs. true plastic strain plots of the as-received and aged conditions are shown in Fig. 5.3 (a) and (b), respectively. From Fig. 5.3 (a) and (b), it is evident that the thermal aging has made significant influences toward the deformation characteristics of this alloy.

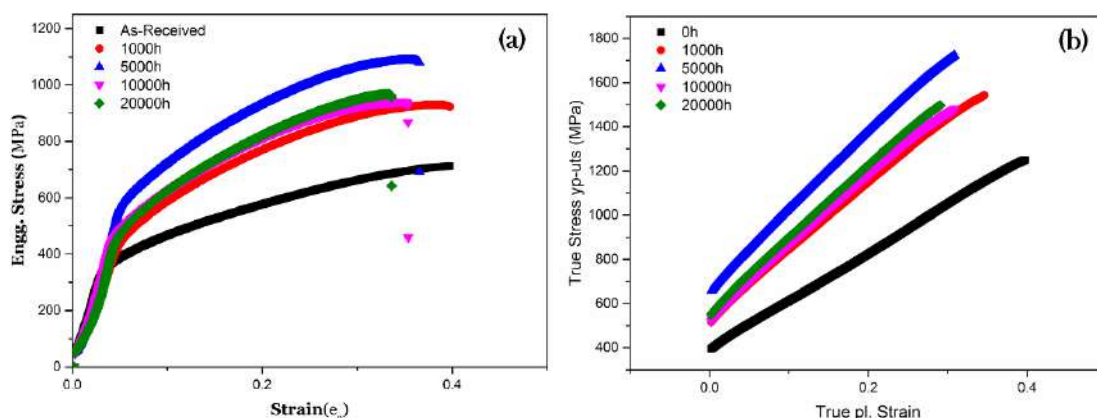


Fig. 5.3 — Tensile curves for Alloy 617 (a) Showing the variations in Engineering Stress-Strain curve for different aged conditions (b) True Stress-Strain plot from the yield point (YP) to ultimate tensile strength (UTS) for different conditions of aging duration.

Different material parameters as derived from the uniaxial tensile tests are given in table 5.1.

Table 5.1 Tensile properties of the indigenous Alloy 617 in the different heat-treated conditions tested at ambient temperature.

| Sr. No. | Aging Conditions (h) | YS (MPa) | UTS (MPa) | Elongation (%) |
|---------|----------------------|----------|-----------|----------------|
| 1. | As-received | 393.14 | 717.90 | 79 |
| 2. | 1000 | 517.24 | 929.15 | 69 |
| 3. | 5000 | 657.31 | 1086.45 | 62 |
| 4. | 10000 | 519.52 | 941.66 | 59 |
| 5. | 20000 | 551.00 | 967.32 | 56 |

As compared to the as-received material, the yield stress (YS) shows an increase up to 5000 hours of aging. Then it declines up to 10000 hours, followed by a marginal rise up to 20000 hours. The as-received alloy does possess some higher ductility in terms of measured %-elongation. As per the first-hand observation of Fig. 5.3 (a), it

reveals that the highest work hardening has been achieved by the as-received one, followed by 1000, 5000, 10000, and 20000 hours in decreasing order.

Variations of yield stress (YS) and % tensile elongation (TE) with the aging duration of the Alloy 617 in both as-received and aged conditions is shown in Fig. 5.4 (a) and (b) Yield stress (YS), as shown in Fig. 5.4 (a), initially increases up to 5000 hours of aging, then decreases in the 5000–10000 hours aging duration and finally shows a saturation/marginal increase in the regime of 10000–20000 hours aging duration. It has been observed that unlike the yield stress variation, the tensile ductility, as measured as the % total elongation (TE) consistently decreases with the aging duration, as shown in Fig. 5.4 (b).

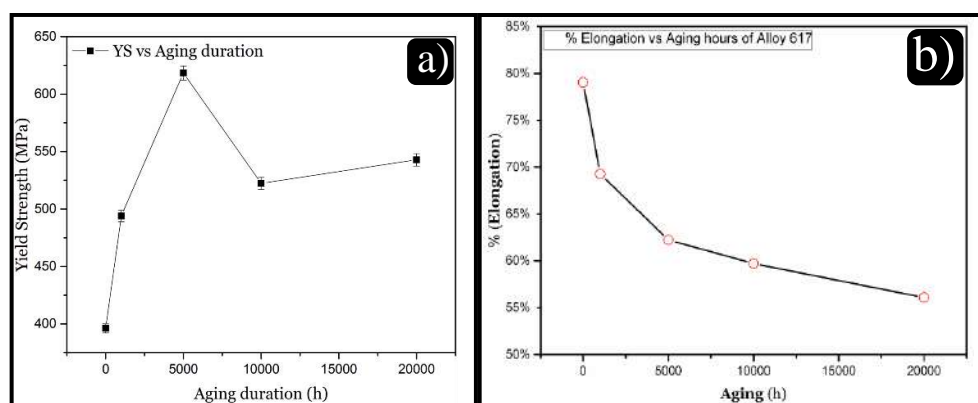


Fig. 5.4 — (a) Variation of yield strength with aging duration; (b) Variation of % of elongation with aging durations.

The yield stress (YS) is defined as the nominal stress level at which bulk plastic deformation is initiated in the material, and is commonly attributed to the initiation of gross dislocation movements in the crystal lattice. It is a well-accepted fact that the type, morphology, shape, and distribution of the precipitates influence the flow of dislocation to a significant extent, thus making the YS a very sensitive deformation parameter to their changes. Thus, the observed variation of yield strength due to the different aging durations needs to be discussed in this light. Further, the effect of stacking fault energy (SFE) often plays a crucial role in the deformation mechanisms, mostly reflected in the

variation of YS. Lower SFE would lead to a lower probability of cross slip of dislocations, and rather confining the movements of dislocations on the slip planes alone. The Alloy 617, in solution annealed condition, can be termed as an alloy with low SFE with SFE $\sim 30 - 40 \text{ mJ/m}^2$ [104-106] The presence of annealing twins in the as-received alloys (Fig. 4.2) also indicates towards its lower SFE [107]. This suggests that the Alloy 617 is more prone to planar slip in deformation, where the motion of dislocations are more strongly influenced by the nature and distribution of the precipitates, as compared to the higher SFE materials with a higher tendency to cross slipping. However, the absence of annealing twins in the aged microstructures (Fig. 4.3 to Fig 4.6) indicates toward an increase in SFE due to aging-induced precipitation and re-distribution of different precipitates.

The TEM results of 1000 hours aged material shown in Fig. 5.5 reveal that the evolution of new precipitates in the form of γ' has started in the early stages of the aging itself. The evolution of precipitates, like γ' and M_{23}C_6 even in its very preliminary stage, has a very profound impact on the mechanical properties of this material. Thus, it is imperative that careful investigation of these precipitates must be carried to explore and establish a relationship between the significant changes occurring in the properties of the material to its constituent shape, morphology, and size of the precipitates.

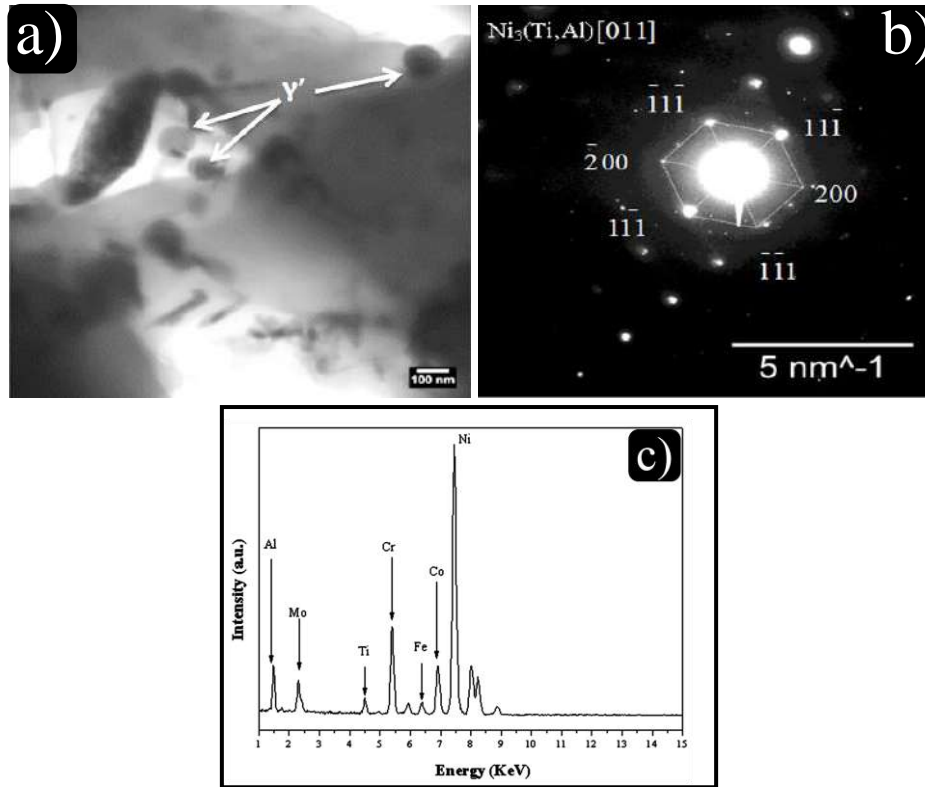


Fig. 5.5 — (a) TEM image after 1000 h of aging showing spherical precipitates of γ' phase commonly known as $\text{Ni}_3(\text{Ti, Al})$; (b) corresponding SAED pattern for γ' precipitates; (c) The corresponding EDS spectrum confirms γ' phase to be rich in Ni, Ti, Al and they correspond to $\text{Ni}_3(\text{Ti, Al})$.

Considering the material to be prone to planar slip due to moderate SFE, the fresh precipitates are expected to inhibit the planar motion of dislocations to a significant extent. This is expected to increase the matrix strength, and raise the yield strength to a significant extent. This explains the stiff rise of YS (up to $\sim 625 \text{ MPa}$) of this material up to the aging duration of 5000 hours. However, further aging treatment up to 10000 hours shows an anomalous behavior, as the YS drops to $\sim 525 \text{ MPa}$. Roy et al.[108], J. Wang et al.[39], and C. Wang et al. [109] have also reported the similar behavior of YS variations during similar aging treatments. It is interesting to note that during this aging duration, there has been a decreasing trend in the hardness too. As discussed earlier, after the 10000 hours aging treatment, a marginal growth in the size of the γ' precipitates (from 40-70 nm to 80-110 nm) has been noticed from the previous chapter in Fig. 4.17 to Fig. 4.18. Coarsening of existing precipitates is always known to

be accompanied by a loss in solid solution strength of the material. Further, in the absence of formation of fresh precipitates, it can be argued that the increase of size would lead to higher interparticle spacing. This straightforward means, for the planar slip to continue, the dislocations would receive reduced resistance from the matrix as the shear stress required to move a dislocation is known to vary inversely with the interparticle spacing [103]. It has also been noted earlier that the absence of annealing twins in the aged micrographs indicates toward an aging-induced increase in SFE. This would give rise to a change in a mode in the dislocation movement, i.e. pro planar slip mode for the as-received one to pro cross slip mode for the aged ones. Indicating that even if fresh precipitates form during the aging treatments during 5000-10000 hours, their influence on the dislocation movements would be less significant as the dislocations would follow an easy path to escape to parallel planes by cross slipping. Thus, it is reasonable to argue that during the aging duration of 5000-10000 hours the material undergoes a softening owing to the combined effect of an increase in the size of the γ' precipitates and the rise of SFE in this regime. This explains the anomalous drop in yield strength of this material during the aging treatment of 5000-10000 hours. Further, a saturation/marginal increase of yield stress up to 20000 hours of aging can be attributed to a saturation of strength due to the trade-off between the ongoing hardening and softening process.

The loss in ductility with the aging duration is convincible from Fig. 5.4 (b). It is frequently argued that in alloys yield strength of the material bears an inverse relation to its ductility. This argument also satisfactorily applies to this alloy until 5000 hours of aging conditions. This inverse relationship fails to follow in the aging duration between 5000–10000 hours where a decrease in yield strength is also accompanied by a simultaneous reduction in ductility. This implies that the loss of ductility is governed by a separate mechanism other than influencing the yield strength. It is found that, after

aging treatment of 5000 hours, grain boundaries get embrittled, and this has been attributed to the aging-induced $M_{23}C_6$ precipitations in the grain boundary region [96]. Presence of extensive carbides near the grain boundaries can be seen from Fig. 4.8 to Fig. 4.12 has been a significant reason for grain boundary embrittlement, and this phenomenon can be considered as a supporting cause in aging-induced loss of ductility.

5.4 Work Hardening Analysis of the As-received and Aged Alloy

617

5.4.1 Analytical Framework for Work Hardening Analysis

Though, several efforts have been made in the literature to explain the work hardening behaviour of engineering alloys with widely varied mechanical and microstructural properties using Hollomon [110], Ludwik [111], Swift [112], Ludwigson [113], and Voce [114, 115], an unequivocal and material independent expression remains elusive even today. At this point, a few important approaches have been discussed in brief. The plastic flow behaviour of several metals and alloys in the uniform elongation regime is satisfactorily described by a simple power law equation (Eqn. 5.1) as proposed by Hollomon.

$$\sigma = K_H \epsilon_p^{n_H} \quad (5.1)$$

where σ is the true stress, K_H is the strain hardening coefficient, ϵ_p is the true plastic strain, and n_H is the strain hardening exponent. A modified version incorporating the mechanical history (in terms of stress σ_0) in the flow relationship has been proposed by Ludwik [111] as expressed in Eqn. 5.2.

$$\sigma = \sigma_0 + K_L \epsilon_p^{n_L} \quad (5.2)$$

where K_L is the strain hardening coefficient and n_L is the strain hardening exponent.

Further towards accounting the pre-strain in the material, Swift [112] has proposed another modification to Eqn. 1 as described in Eqn. 5.3.

$$\sigma = K_S (\varepsilon_0 + \varepsilon_p)^{n_S} \quad (5.3)$$

where ε_0 , signifies the amount of pre-strain in the material and K_S , n_S is the strain hardening coefficient, and exponent, respectively.

Ludwigson [113] demonstrated that large positive stress deviation in FCC material on account of their lower stacking fault energy (SFE) could not be described by Hollomon which can be overcome by an extra term as

$$\sigma = K_1 \varepsilon_p^{n_1} + \exp(K_2 + n_2 \varepsilon_p) \quad (5.4)$$

where K_1 and n_1 bear the same identity as K_H and n_H in the Eq. (1) respectively, and K_2 and n_2 are new additional constants. Voce [114, 115] proposed a different equation for materials demonstrating saturation behaviour at high magnitudes of stress/strain levels as

$$\sigma = \sigma_s - K_V \exp(n_V \varepsilon_p) \quad (5.5)$$

with σ_s is the saturation stress, K_V and n_V are strain hardening coefficient and the rate at which stress tends to achieve steady-state respectively.

From the tensile tests, true stress (σ)-true plastic strain (ε_p) data for all the aged materials have been obtained following usual procedures as practiced in tensile tests. The σ vs. ε_p data were fitted to the various flow relationships through Eqns. (5.1) – (5.5), respectively, using the Levenberg–Marquardt (L–M) algorithm [116, 117] with unknown constants as adjustable parameters. The goodness of fit was evaluated using the Chi-squared (χ^2) value [118].

To better understand the flow curve logarithmic true stress (σ)-true plastic strain (ε_p) data were obtained using a computer software program from the digitized load–elongation data up to the maximum load values, i.e., up to the onset of necking. Since no strain gauge was deployed; the specimen extension was taken equivalent to the crosshead displacement. The linear elastic portion of Load–Elongation data was also contributed by the specimen, machine frame, and load-train assembly. The

combined effect of this elastic elongation was subtracted from the total elongation by appropriately using the slope of the initial linear portion of the Load–Elongation curves for the calculation of plastic strain. The plot of the logarithmic scale of true stress (σ)-true plastic strain (ϵ_p) is shown in Fig. 5.6 was obtained from stress and plastic strain data respectively.

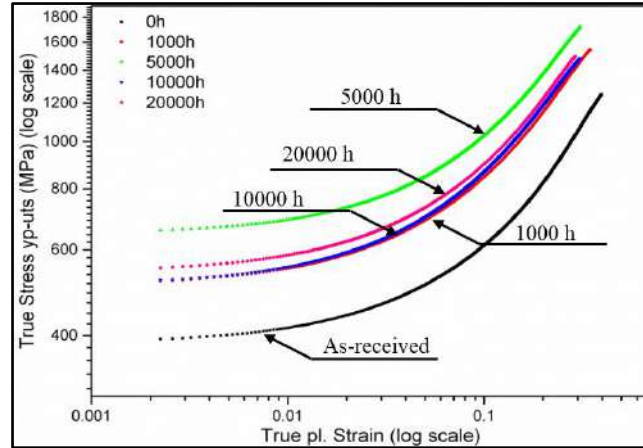


Fig. 5.6 — True stress (σ)-true plastic strain (ϵ_p) for Alloy 617 obtained at a strain rate of $3 \times 10^{-3} \text{ s}^{-1}$ for different aged conditions are superimposed.

Alloy 617 exhibits a nonlinear log (σ) vs. log (ϵ_p) characteristics in the plots shown in Fig. 5.6 for all the different heat-treated conditions, including the as-received material. The sudden increase in log (σ) vs. log (ϵ_p) for the 1000 hours aged alloy w.r.to as-received is attributed to the lesser density of dislocation-dislocation interaction in as-received material. As aging proceeds, this material owing to its strong propensity to precipitate formation even at the relatively shorter period of aging duration [60] causes dislocation-precipitates interaction a dominating mechanism. A further increase in the flow curve of 5000 hours is because of fine γ' structures in the matrix which started to precipitate as early as 1000 hours of aging as can be seen from Fig. 5.5 (a). The curve reaches its global maximum at 5000 hours aging and then drops down in the interval from 5000 to 10000 hours. This drop in the work hardening behaviour of the alloy is attributed to the: (1) coarsening of γ' during further aging (though only a small

variation in size) causes the mobility of dislocation easier and a drop in strain hardening which is consistent with other Ni-based superalloys [119], (2) the rapid drop in the work hardening from 5000 to 10000 hours aging can be attributed to the dissolution of γ' in the course of aging. Surprisingly there is an increase in the flow stress of 20000 hours of the aged sample. The increase in the work hardening from 10000 to 20000 hours can be supported by the evolution of some new precipitates in the matrix. This increase in the work hardening pattern is attributed to some further finer precipitates which might have to evolve during aging treatment giving resistance to dislocation motion.

5.4.2 Flow relationships of Alloy 617

A comparison of the Chi-squared (χ^2) values as obtained from the flow curves of material aged till 20000 hours is presented in Table 5.2, and various flow relationships have been examined and plotted in Fig. 5.7.

Table 5.2 Values of χ^2 for different flow relationships fitted for the different heat-treated conditions tested at ambient temperature. (All the values have been rounded off to one decimal place.)

| Sr. No. | Aging Conditions (h) | Hollomon | Ludwik | Swift | Ludwigson | Voce |
|---------|----------------------|----------|--------|-------|-----------|-------|
| 1. | As-received | 3100.9 | 252.6 | 19.1 | 14.5 | 258.1 |
| 2. | 1000 | 13379.9 | 57.6 | 41.3 | 9.0 | 39.0 |
| 3. | 5000 | 3799.5 | 48.9 | 31.6 | 48.9 | 60.1 |
| 4. | 10000 | 5420.4 | 46.2 | 27.9 | 46.2 | 14.0 |
| 5. | 20000 | 13038.0 | 17.8 | 15.1 | 17.8 | 21.3 |

The χ^2 values obtained from various flow curves convince us that the Hollomon relationship cannot be adopted to describe the plastic flow behavior of this alloy in any of the five heat-treated conditions, as the plots exhibit curvilinear behavior and not mere straight lines. The non-linear nature of the flow curve invites other flow relationship to be tested for the best fit.

Hereafter results from the analytical framework of σ - ε_p data using Hollomon and Voce relationships are not considered owing to their abnormal values of χ^2 and unrealistic prediction of σ - ε_p data. Ludwigson and Swift equations exhibited comparatively lower χ^2 values compared to those shown by Hollomon, Ludwik, and Voce equation for all the aged conditions of the alloy. Interestingly, it can be seen that both Ludwigson and Ludwik relationships describe σ - ε_p behavior adequately with nearly equal confidence for 5000, 10000, and 20000 hours of aging conditions shown in Fig. 5.6. Swift equation follows the experimental data with a good lower value of χ^2 in the aging duration of 5000-20000 hours. High χ^2 values for Hollomon and Voce equations (Eqn. 5) indicated their inapplicability in the range of aging duration of as-received-20000 hours except that for 10000 hours as shown in Table 5.2. Alternatively, a closer look at Voce equation demonstrates the capability to describe σ - ε_p behavior adequately with marginally higher χ^2 values than those obtained for the combination of Ludwik and Hollomon equations in the entire aging range of interest, i.e., as-received–20000 hours (Table 5.2). The gain from the application of Ludwigson equation arises mainly due to the following: (a) single flow relation can offer a reasonable description of σ - ε_p data for the different aging durations and (b) provide a useful prediction of tensile properties [120].

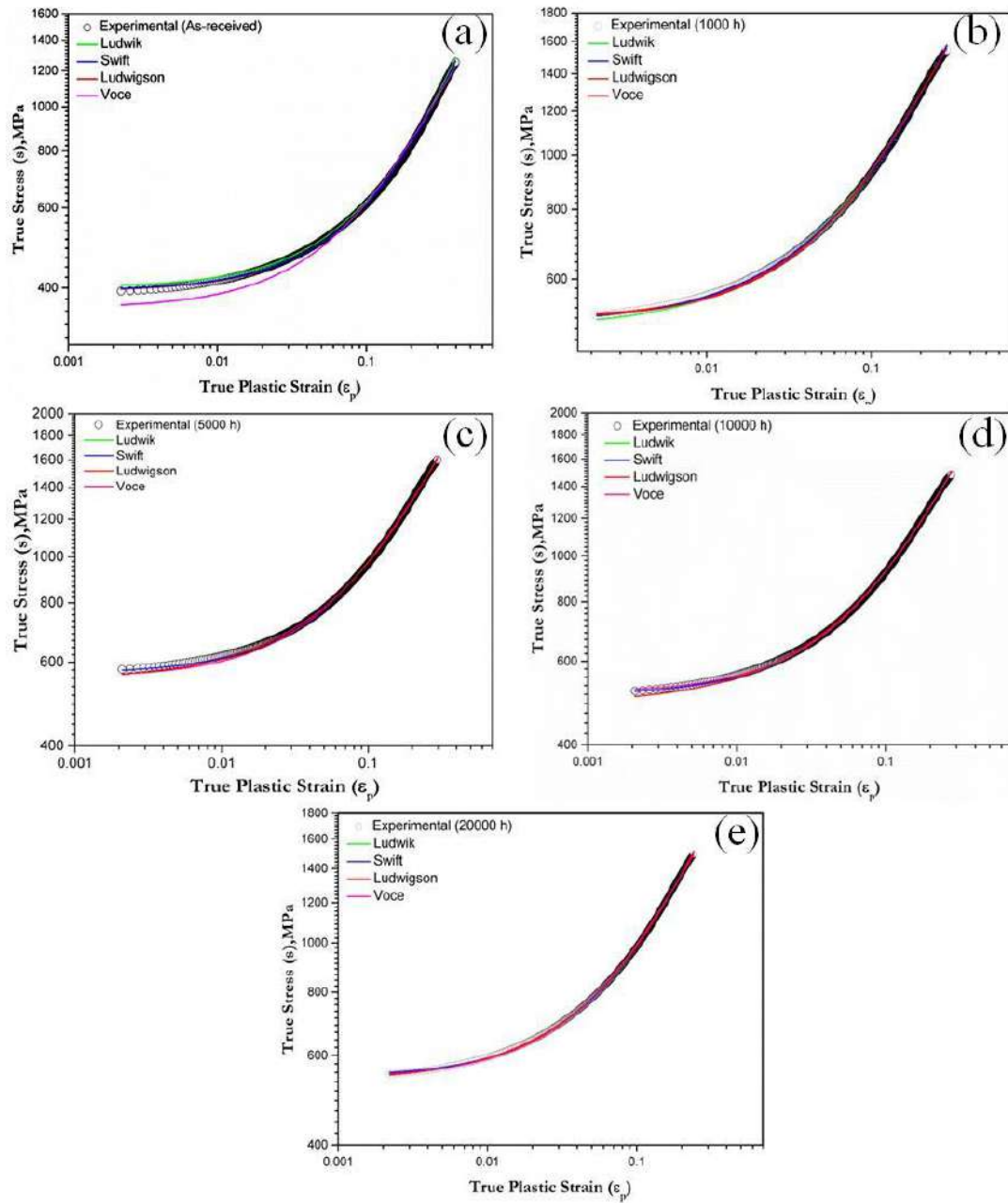


Fig. 5.7 — Best fit for different flow relationships true stress (σ)–true plastic strain (ϵ_p) for Alloy 617 at strain rate of $3 \times 10^{-3} \text{ s}^{-1}$ for different aged conditions at 1023 K ; (a) as-received; (b) 1000 h; (c) 5000 h; (d) 10000 h; (e) 20000 h.

Ludwigson and Swift's relationships are seen to closely match the experimental data and gives the best fit for the various aged conditions examined for true stress (σ)–true plastic strain (ϵ_p). Ludwigson and Ludwik relationships are known to describe the flow behavior of these materials, exhibiting identical nonlinear characteristics of $\log(\sigma)$ vs. $\log(\epsilon_p)$, such as Supercast 247A, Nimonic 263, and various other austenitic

stainless steels family [119, 121, 122]. Ludwigson and Ludwik equation shows identical values for the aging duration between 5000–20000 hours. Ludwigson equation is, in general, a best-fit mathematical model for various FCC materials and is based on the deviation of stress at low strain from that resulting from extrapolation of the linear high strain data [123]. Greater insight into the physical interpretation of flow can be obtained in work carried by Soussan et al. [124]. While K_1 and n_1 in the Ludwigson are defined as work hardening coefficient and exponent respectively and have the same significance as K and n in power-law expression. The term K_2 in the $\exp(K_2 + n_2 \epsilon_p)$ is a representation of true stress, extrapolated to a true plastic strain of zero, in the plot of $\log(\omega)$ vs. ϵ_p ; where $\omega = \exp(K_2 + n_2 \epsilon_p)$, is the difference between the experimental true stress value and true stress represented by the extension of the straight line segment of the $\log(\sigma)$ vs. $\log(\epsilon_p)$ (straight-line slope touching to the exponential curve not shown in the graph for simplicity). Moving to K_2 and n_2 , K_2 is responsible for inducing short-range stress first mobile dislocation, whereas n_2 represents the ratio between short-range and long-range stress decrement.

5.4.2.1 Variations of Work Hardening Parameter with Aging Durations

The variation of strain hardening parameters K_1 , K_2 , n_1 , and n_2 of the Ludwigson with aging duration are shown in Fig. 5.7. Aging for 5000 hours shows a transition in the K_1 and K_2 , which can be clearly seen in Fig. 5.8 (a) & (b), respectively. On the other hand, n_1 and n_2 show an opposite trend to that of K_1 and K_2 ; their values decrease up to 1000 hours of aging then again a slight increase in the 5000 hours aging. The variation in the 20000 hours is also appreciably higher in comparison with 10000 hours of aging. The additional constant n_2 in the Ludwigson equation exhibited a marginal increase (in negative scale) in the aging duration of 1000 hours followed by a sharp increase for 5000 hours.

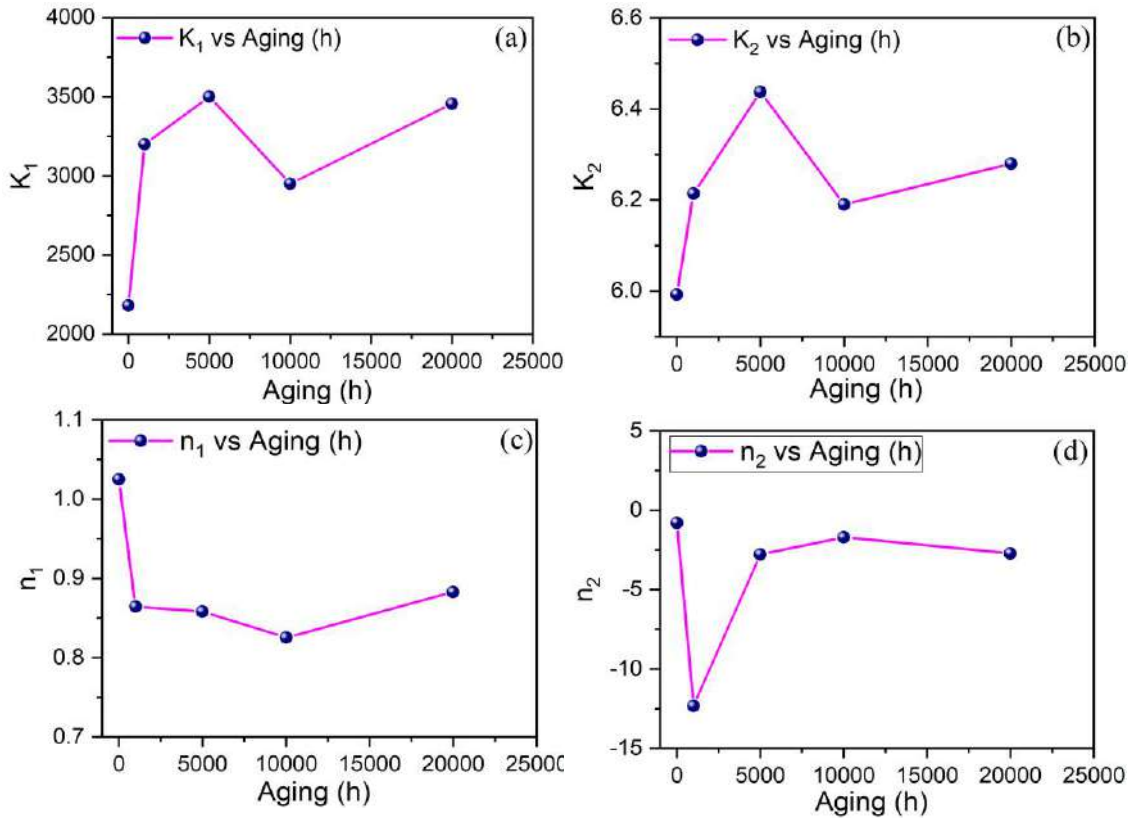
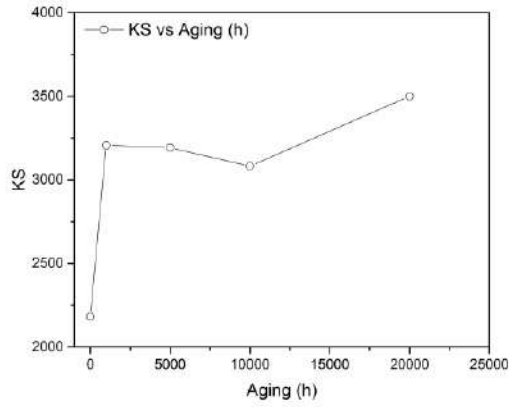


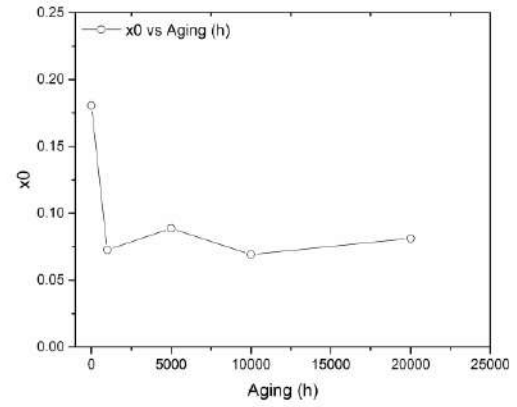
Fig. 5.8 — Variation of Ludwigson equation parameters (a) K_1 ; (b) K_2 ; (c) n_1 ; (d) n_2 with the aging treatment of Alloy 617.

The plot of Swift equation parameters (K_s , x_0 , and n_s) against aging hours shown in Fig. 5.9 also shows similar trends to that of Ludwigson. The strain hardening coefficient K_s is seen likely to follow a similar trend to that of Ludwigson parameter. The strain hardening exponent n_s is also set to shows a similar orientation to that of n_1 of Ludwigson parameter.

(a)



(b)



(c)

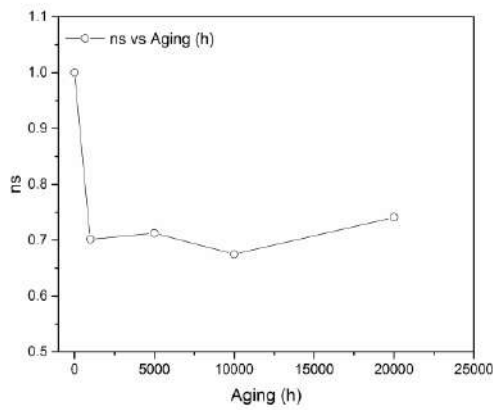
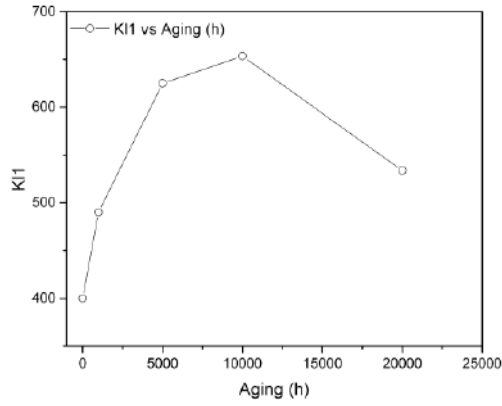


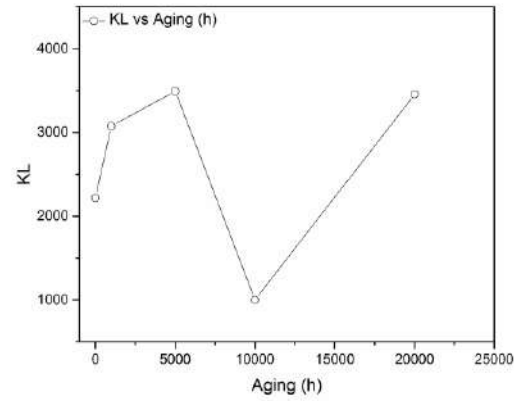
Fig. 5.9 — Variation of Swift equation parameters (a) K_s ; (b) x_0 ; (c) n_s with the aging treatment of Alloy 617.

The flow behaviour studies using Ludwik equation shown in Fig. 5.10 also shows similar trends to that of Ludwikson. The strain hardening coefficient K_L also imitates the Ludwikson parameter in a similar trend. The strain hardening exponent n_l is also showing a similar orientation.

(a)



(b)



(c)

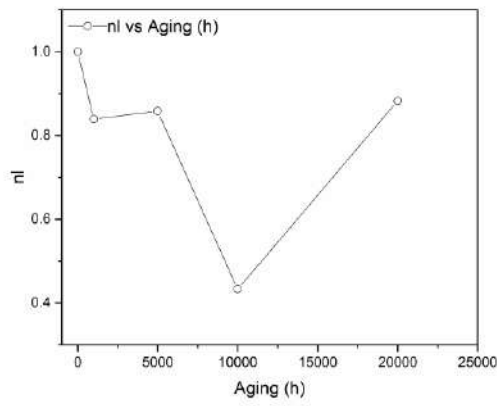


Fig. 5.10 — Variation of Ludwik equation parameters (a) K_{11} ; (b) K_L ; (c) n_1 with the aging treatment of Alloy 617.

It can be seen from the above fit that Ludwikson follows the experimental data more closely than any other flow curves used. But Ludwik and Swift too are in good agreement for the flow curve analysis of the Alloy 617.

5.4.2.2 Variations of Instantaneous Work Hardening Rate with Stress and Aging Duration

In order to get insight into the work-hardening behavior of the Alloy 617, the instantaneous work-hardening rate $\theta = d\sigma/d\varepsilon_p$ is considered as is plotted against σ as shown in Fig. 5.11. The plot of θ vs σ is preferred over θ vs ε_p , as this equation is invariant to prior deformation history as proposed by Reed-Hill et al.[125].

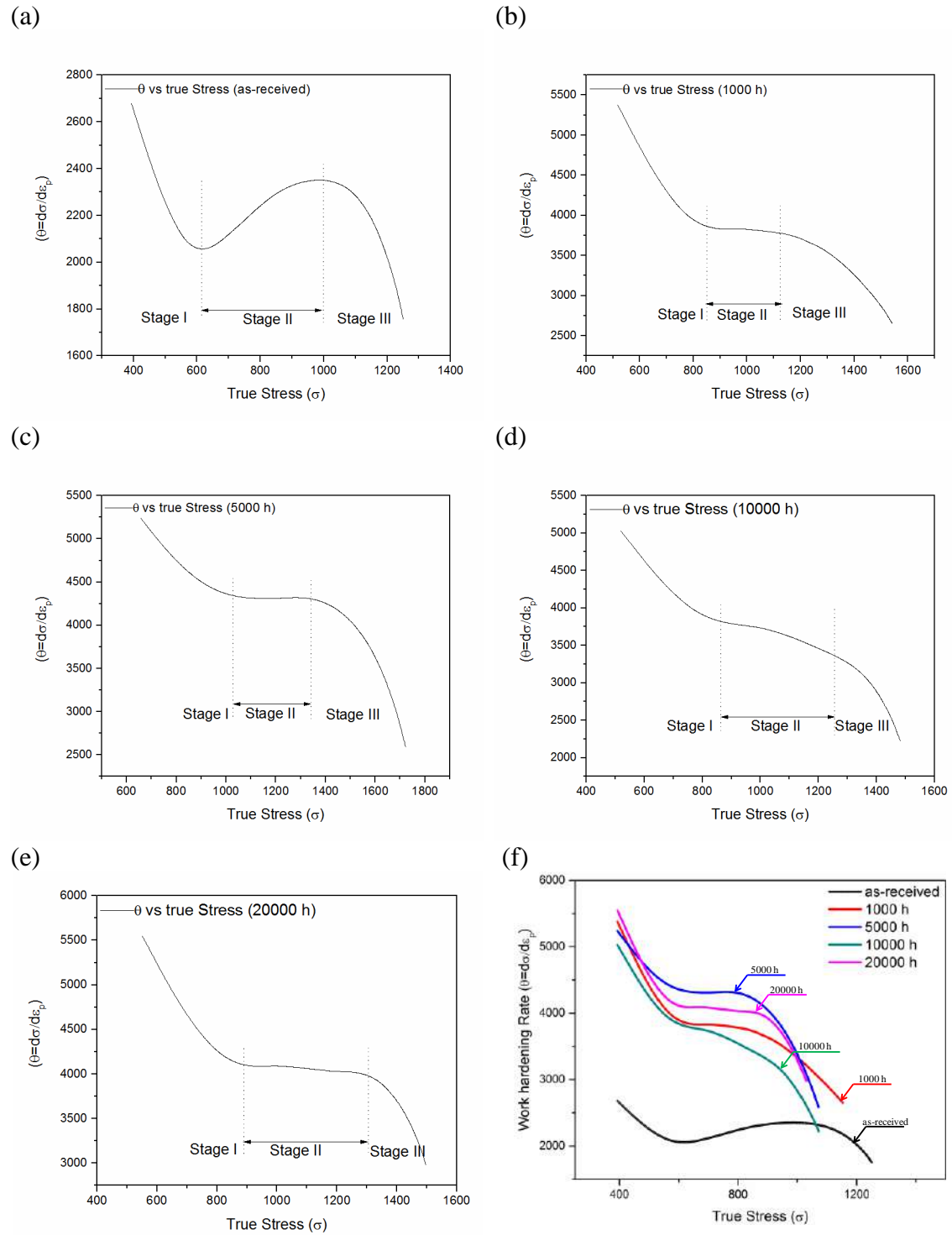


Fig. 5.11 — Variations of instantaneous work hardening rate θ vs σ for different aged conditions for Alloy 617; (a) as-received; (b) 1000h; (c) 5000 h; (d) 10000 h; (e) 20000 h; (f) Combined plot of θ vs σ for all aged samples.

It is customary, that the rate $\theta = d\sigma/d\epsilon_p$ of work hardening continuously decreases with an increase in strain; however, deviations from this behavior have been reported earlier by Kocks et al. [126] and Asagari et al. [127]. Fig. 5.11 shows the

results of the numerical differentiation of the experimental data as derivative functions of the fitted equations. All the θ - σ shows clear three-stage behaviour at all aging durations: (1) an initial transient stage (TS), where θ decreases rapidly, (2) a stage where θ increases gradually and attains a local maximum (stage II) with σ for as-received alloy and almost remain constant in other aged conditions, and (3) a stage where θ gradually decreases (stage III). While the work hardening rate increases for as-received and 1000 hours aged alloy, it remains nearly constant for the rest of the aging conditions. This disparity in work-hardening characteristics of the material in its different heat-treated conditions are attributed to the differences in their initial microstructures as can be seen from Fig. 4.2 to Fig. 4.6. The various zones of hardening observed in this material are accordant with those reported for other metals and alloys [122, 128]. In polycrystalline material the transient stage I occur only for lower initial plastic strain, the value of which is a function of SFE. The low value of SFE forbids cross slip of dislocations at a lower value of strain. Initially, deformation in this alloy occurred easily, as the dislocations can travel relatively large distances before encountering barriers. This is because the matrix is devoid of precipitates such as γ' and $M_{23}C_6$.

Stage II is triggered at a particular level of stress achieved inside the material and is also a function of SFE. The Alloy 617, in solution annealed condition, has low SFE with SFE ~ 30 -40 mJ/m² [107] The presence of annealing twins in the as-received alloys (Fig. 4.2) also indicates towards its lower SFE [107]. This indicates that the Alloy 617 is more prone to planar slip in deformation, where the motion of dislocations are more strongly influenced by the nature and distribution of the of precipitates, as compared to the higher SFE materials with a higher tendency for cross slipping. It is this difficulty of cross slip and multiple slips during the process of a planar slip lead to an increase in work hardening behavior in stage II. However, during aging, the

resistance to dislocation motion is reduced on account of a coarsening of the precipitates and thus stage II of 5000 to 20000 hours aged shows steady characteristics. Stage III is a recovery stage where again θ decreases, but now with a small change and with a good increase in ε_p . At this stage, a sufficient number of plastic deformations have been accumulated, which causes a localized stress increment causing a tendency to cross slip and consequently there is a decrease in work hardening.

Combined results in Fig. 5.11 (f) shows that there is a similar trend in the instantaneous work hardening rate behaviour of this alloy and $\log(\sigma)$ vs. $\log(\varepsilon_p)$, plot. The work hardening increases from as-received to 5000 hours and then a drop till 10000 hours, and again, there is a marginal increase in 20000 hours aged specimen.

5.4.3 The Fundamental Interplay of Precipitate-Matrix Interface and its Influence on Work Hardening

The fundamental interplay between the precipitate-matrix interface and its influence on the material property will be discussed in the subsequent paragraph hereafter.

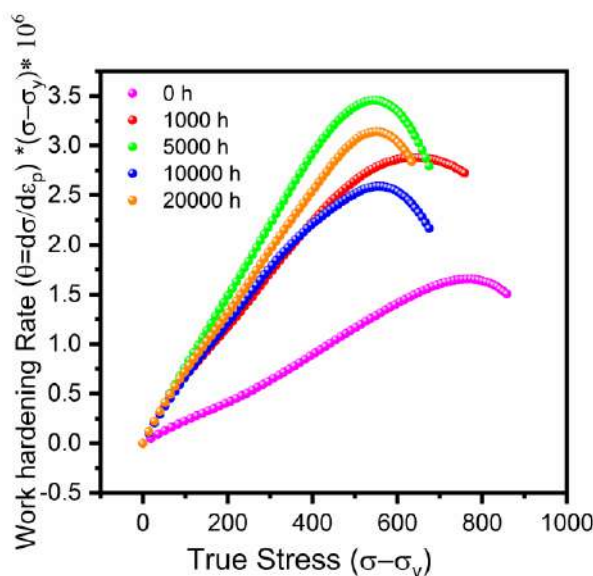


Fig. 5.12 — Variations of instantaneous work hardening rate $\theta \times (\sigma - \sigma_y) \times 10^6$ vs $(\sigma - \sigma_y)$ for different aged conditions for Alloy 617.

Fig. 5.12 clearly reveals two main mechanisms occurring in the various aged conditions in the Alloy 617. A long term hardening due to carbides precipitants followed by a softening due to Ostwald ripening. This kind of behaviour is also demonstrated in other superalloys family [54]. After long term aging the carbides precipitates reaches a certain volume fraction and thus the distance between the two nearing neighbours increases. The increase in the neighbouring distance reduces the capacity of strengthening due to Orowan bowing mechanism [129, 130]. One again it has to be reminded here that the grain boundaries and structures do not appreciably change in this alloy, so the possible attributes to strength reduction come from the precipitates coarsening. Over the long term aging the number density decreases which results in an appreciable increase in effective distance leading to a fall in strength of this alloy at around 10000 hours.

Something strange happens at 20000 hours, the work hardening rate increases contrary to the expected decrease in other alloys over long duration aging. As revealed in Fig. 4.21 there are some finer rods shaped coherent precipitates. These coherent precipitates are expected to increase the stress and results in an increase in overall yield stress and work hardening rate. Owing to the absence of high-resolution TEM (HRTEM) images only theoretical support can be given in the direction of coherency of the precipitates in 20000 hours aged sample. From the literature support it is known that a needle shape precipitates help in increasing the resistance to deformation [2, 131].

5.5 Insights Into the Deformation Mechanism

To get deeper insights into the deformation mechanism of this material in various aged condition, we additionally investigated failed tensile specimens of 1000 and 20000 hours aged samples. These samples are representative of our entire aged specimen

owing to its initial and final aged conditions of our studies. Fig. 5.13, clearly develops an idea that how the fracture mechanism might have changed in our material.

From the fractographic observations as shown in Fig. 5.13, it is certain that this material has a clear tendency of change in its fracture mode from predominantly ductile to predominantly intergranular cracking as the aging time increases from 1000 to 20000 hours. To strengthen our proposed fracture mechanism we investigated 1000 and 20000 hours samples and tried to present a clear picture behind the mechanism of deformation. Fig. 5.13 (a) is a representative image of 1000 hours fracture tensile tested sample and the region marked as **1** shows the micro-crack formation close to the grain boundary. This is an indication that the thermal residual stress concentrations have just surpassed the UTS locally which generally occurs at a precise point and a certain temperature [132, 133]. The region marked as **2** in Fig. 5.13 (a) shows a tendency of intergranular fracture in this material. The reason for this tendency is not far to seek, as the aging durations increase the secondary precipitates coarsen and their preferential segregation to the grain boundaries further acts as nucleation sites for the crack growth. The region marked as **3** in Fig. 5.13 (a) is a dimple structure a representative of ductile failure in the material. These marked positions (**1**, **2**, **3**) clubbed together in one deformed fractographs is a straight indication toward ductile failure inside the material. SEM image of the 20000 h aged sample shows plenty of slip bands as shown in Fig. 5.13 (b). Extensive slip bands are also observed in the high Mn-based lightweight steels [134] as in our material. These extensive slip bands are an indication that definitely the fracture mode has changed from the ductile to certainly that is non ductile in nature.

It would be interesting to recall that the grain size and grain boundaries remained fairly constant in this material (discussed in detail in section 4.2) and yet though marginal this material showed anomalous tensile behavior. It showed increasing yield strength after 20000 hours aging, contrary to the belief that during the aging yield

strength of a material usually increases to a certain time and then decreases further [135, 136]. To sum up- this material showed a fairly constant grain size, tensile elongation continually declined over the aging duration, and precipitates also showed a gradual increase in size or coarsened during the aging. In spite of these behaviors, tensile strength behaved abnormally and rescinded to follow the usual trend and showed a marked increment at 20000 hours of aging. The credit goes to few new precipitates that just started evolving in the longer aging duration of 20000 hours. These precipitates are finer in structure and thus raise the tensile strength of the material. Turning towards the fracture mechanism in the most embrittled tensile specimen, TEM images shown in Fig. 5.13 (c and d) clearly demonstrate that the extent of slip bands in 1000 and 20000 hours differ significantly. The extent of slip bands in 20000 hours is relatively more than the 1000 hours fractured tensile sample. The presence of smaller precipitates in 20000 hours is a testimony of the re-precipitation and dissolution of older precipitates. Though the presence of smaller but newer precipitates has helped in increasing the tensile strength, but the fracture mode has not changed significantly. The fracture mode in the most embrittled state is still intergranular fracture.

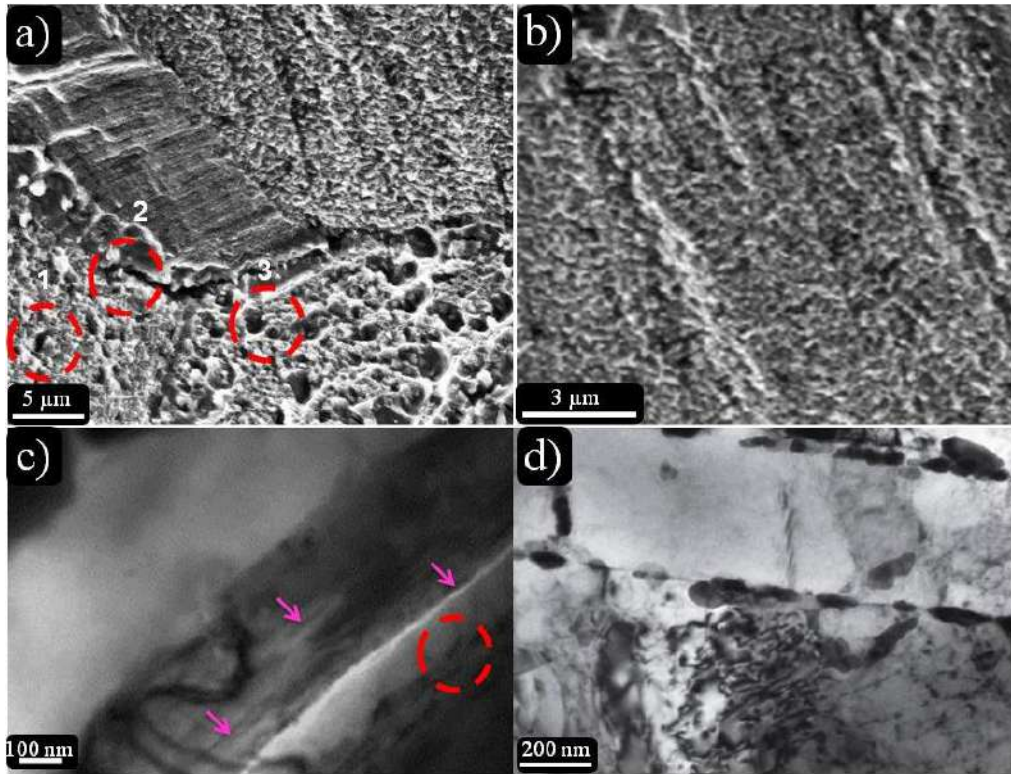


Fig. 5.13 — Deformed micrographs of the Alloy 617 in aging conditions for 1000 and 20000 h at a strain rate of $3 \times 10^{-3} \text{ s}^{-1}$. (a) The presence of sufficient amounts of fibrous dimples is a major characteristic of ductile deformation mechanism; (b) extensive amounts of slip bands in 20000 h aged sample is an indication that this material has a strong tendency for the planar slip and do not favor the cross slip tendency; (c) TEM image shows the presence of nano-twins as formed in 1000 h aged sample; (d) TEM images of 20000 h deformed samples clearly show extensive precipitations. These extensive precipitations and grain deformations explain the enhanced capability of extended tensile elongation in this material.

To support our proposed mechanism we performed the EDS analysis on the fractured samples and surprisingly found that precipitate distribution has a strange characteristic in both the samples as shown in Fig. 5.14. The EDS spectra in Fig. 5.14 (a) shows very less intense peaks of Cr and Mo indicating that the presence of Cr and Mo-rich phases in 1000 hours tested samples. Exactly opposite is seen in Fig. 5.14 (b) which show intense peaks of Cr indicating that the presence of Cr-rich phases in 20000 hours tested samples. We stand on the previous reports that the solubility limit of Cr in the Ni-rich alloy in the temperature range of 600 - 950 °C is ~ 32-43 atomic % [108]. This characteristic of Cr favors and offers its mobility inside the matrix at much-

reduced resistance than Mo and thus succeed in the formation of more new precipitates. Another advantage that Cr enjoys over me is its long-range diffusion of Cr enabling the precipitates to be evenly distributed in the matrix. This characteristic of Cr has offered a substantial rise in the tensile strength as shown in Fig. 5.4 (a).

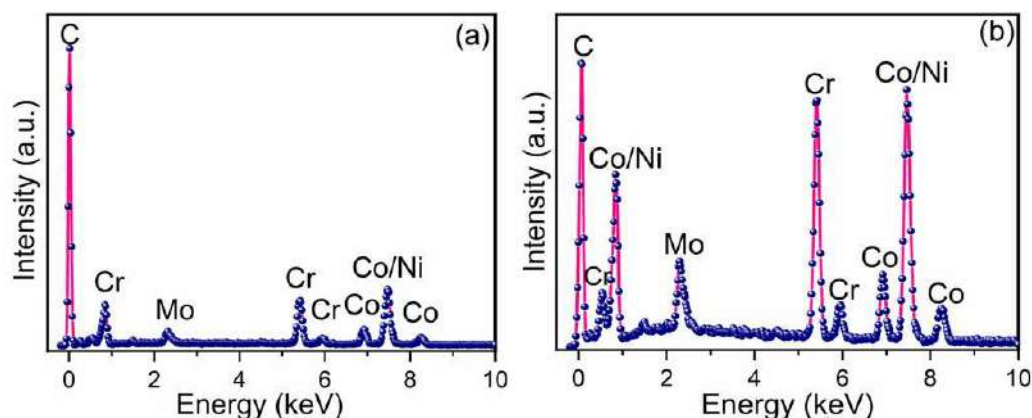


Fig. 5.14 — The elemental mapping of the fractured tensile samples. (a) The EDS spectrum of 1000 h indicates that precipitates are rich in Cr and minimal in Mo-rich; (b) The elemental mapping of 20000 hours tensile tested sample indicates that there has been a substantial rise in the Cr and Mo-rich phase in the precipitates. The intense peaks of Cr and Mo in (b) is an indication that these elements are widely distributed in the matrix.

We hear also state that few new types of unidentified precipitates are also seen in Fig. 4.21. These fine precipitates along with these Cr-rich precipitates have doubly helped in raising the tensile strength, but the fracture mode in the most embattled state still remains to be intergranular in nature. As Cr mostly precipitated inside and on the grain boundaries, the crack initiation through these paths is comparatively easier. To sum up, we see a transition of the fracture mode from ductile to mixed mode and finally fracture through an intergranular mode.

5.6 Summary

Based on the detailed studies of the effect of thermal aging on the hardness, tensile behavior, and instantaneous work hardening of Alloy 617 and their correlation with

microstructure, following conclusions have been made: Thermal aging of Alloy 617 is accompanied with precipitation of γ' precipitates, which strongly influences the hardness and tensile properties of this alloy after different aging durations. The absence of annealing twins in the aged specimens indicates toward an aging-induced increase of stacking fault energy. This alloy exhibits anomalous work hardening characteristics for the different aged conditions. There has been a sudden rise in the work hardening from as-received to 1000, 5000, and then a sudden drop at 10000 hours. The anomalous decrease in yield stress between 5000 hours and 10000 hours aging duration is attributed to the ease of dislocation movement in this regime owing to the combined effect of coarsening of γ' precipitates and the rise in stacking fault energy. Alloy 617 exhibits three distinct stages of work hardening in the plot of θ vs. σ for all the four heat-treated conditions. The three stages of work hardening are observed for all aged specimens. An initial transient stage (TS), where θ decreases rapidly, the stage II is more prominent in as-received and 1000 hours and remains almost constant for other conditions of aging conditions and a stage III where θ gradually decreases. Based on the detailed fracture mechanism explained in the aforesaid paragraph, we also arrive at a conclusion that there have been gradual changes in the fracture mode of various tensile tested specimens from ductile in the as-received, then a mixed-mode in the next aged material and finally ended its life with the intergranular fracture in the 20000 hours specimen.

6

Study of Fracture Resistance of As-Received and Aged Alloy 617

Fracture resistance of an engineering material as measured in terms of the impact energy is one of the essential mechanical properties of the designers. This is also recognized as most microstructure sensitive mechanical properties. As discussed in the previous chapters that after aging, Alloy 617 undergoes a substantial change in its microstructure at different length scales. Thus, it is anticipated that the fracture resistance of this alloy will be strongly influenced due to the aging treatments in different durations. This chapter brings forth the results of the investigations on the degradation of fracture energy after different aging durations, as measured by Charpy impact tests. The results have been analyzed in the light of aging-induced microstructural changes in this material. Further, the load-displacements plots as obtained from the instrumented Charpy tests have been used to generate the fracture resistance curves using an analytical-empirical methodology as proposed in the literature.

6.1 Introduction

Degradation of fracture resistance of an engineering material during their service period is a matter of concern for the designers as early initiation and propagation of crack often lead to premature failure of a component. Especially, when exposed to higher temperatures for longer durations, this is further aggravated due to unfavorable microstructural changes due to thermal aging. As the Alloy 617 is mostly used in the high-temperature domain for longer durations, the study of its degradation of fracture energy due to aging-induced microstructural variation bears technological importance.

Charpy impact tests are one of the most common testing methodologies to evaluate the fracture resistance of materials at different material conditions. The fracture resistance as measured in terms of the impact energy is often considered to be one of the most microstructural sensitive parameters. Further, the presence of a notch in the Charpy specimens and the associated high strain rates originating from impact loads give rise to the most conservative (lowest) estimation of fracture resistance of the materials. The use of an instrumented Charpy gives rise to the loading history of the material in terms of load vs. displacement plots. These can also be used to derive some of the mechanical properties of the materials at higher strain rates. In this light, the fracture resistance of the as-received and aged Alloy 617 has been investigated using the Charpy impact tests.

In chapter 4, it has been observed that the Alloy 617 undergoes significant microstructural changes due to the aging treatments. Its influence on the tensile deformation and work-hardening behavior has been analyzed in Chapter 5. This chapter deals with aging-induced degradation of fracture energy of Alloy 617 concerning the microstructural changes due to aging treatments.

6.2 Materials and Methodology

The details of the chemical composition and the aging treatments have been given in chapter 3. After aging treatment, full-size Charpy V-notch specimens (Fig. 6.1) with dimensions of $(55 \times 10 \times 10 \text{ mm}^3)$ were fabricated in conformity with the ASTM E-23 [74] from these tubular blocks with two different notch orientations, namely, Type-A and Type-B. The Type-A notch orientation has ensured crack propagation along the circumferential direction, and the Type-B notch orientation has ensured crack propagation in the radial direction. The schematic layout of the specimen fabrication,

along with the notch axes for both the Type-A and Type-B notches, is also shown in Fig. 3.1. For more details on the material aging condition refer to chapter 3.

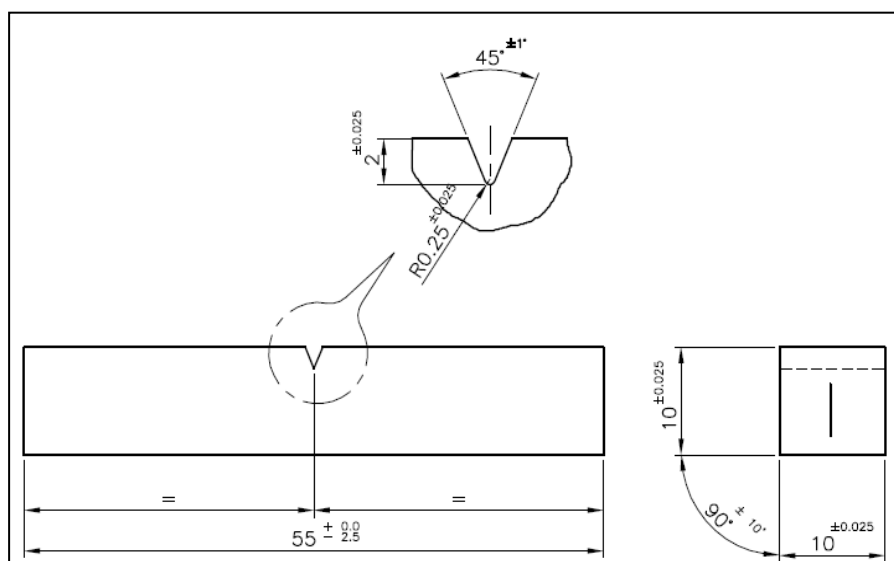


Fig. 6.1 — Schematic representation of a Charpy impact specimen with given dimensions in mm.

6.3 Results from Charpy Impact Testing

The variation of Charpy impact energy (J) with aging duration (h) is shown in Fig. 6.2. Though the Charpy energy values show usual scatter, a systematic trend of degradation with the aging time can be noticed in Fig. 6.2 (a). This material shows high impact energy in the as-received condition, but a sharp reduction in impact energy after 20000 hours of aging. A reduction of $\sim 80\%$ w.r. to as-received material has been noticed in 20000 hours aged material.

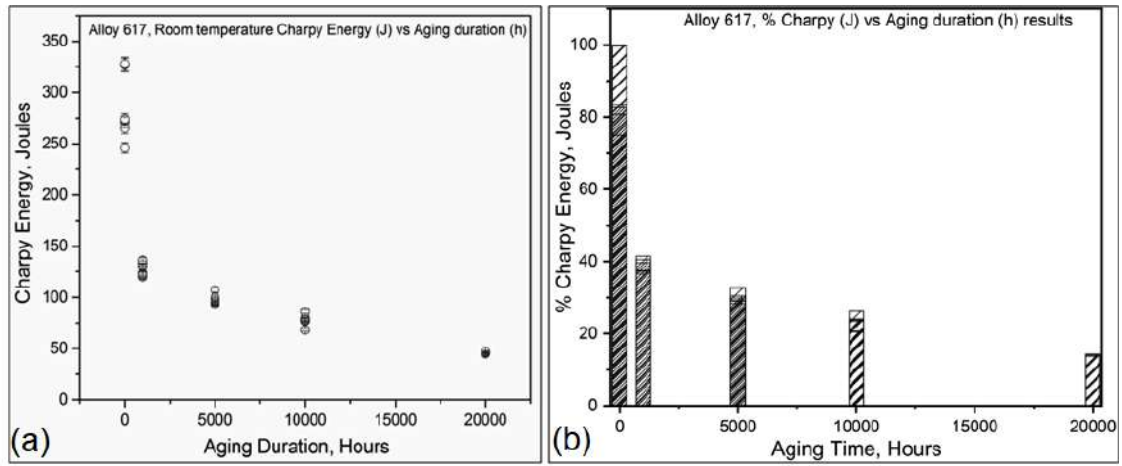


Fig. 6.2 — Effects of thermal aging on the variation of Charpy impact energy for the Alloy 617. (a) Charpy energy profile of alloy 617 aged at various conditions; (b) % Charpy energy of the aged conditions.

Aging has a profound influence on the Charpy impact energy of this material as can be seen from Fig. 6.2. The Charpy tests conducted at room temperature for the as-received specimen shows the highest value with an average energy of ~ 285.16 J. There is a rapid drop in the Charpy impact energy during the first 1000 hours of aging and the average energy of impact reaches ~ 130 J. The subsequent energy values after 5000 and 10000 hours of aging have shown a marginal decrease with registered average values of 98.16 and 77.6 J, respectively. Alloy 617 aged for 20000 hours shows a huge difference in the Charpy impact energy as compared to as-received material. The drop is as high as 83 % w.r.to as-received one. This extensive reduction in Charpy impact energy is a clear indication of a reduction in the toughness of this material over long duration aging.

Fig. 6.2 (b) reveals that, though there has been a sharp decline in the 1000 hours aged material further aging has influenced a little as clearly evident from the bar graph. The strong nature of precipitate evolutions has asked the impact energy value to drop drastically from as-received to aged one. But, as aging progresses, the evolved precipitates coarsen slowly. This characteristic helps in imparting greater strength to this material. Over aging has always been detrimental to alloys operating at high temperature but this alloy is resistant to such severe attacks. The coarsening of

precipitates mainly at the grain boundaries provide a site to initiate cracks and propagate through it, causing a decline in the impact energy of this material.

6.4 Fractography of Charpy Tested Specimens

To better understand the type and cause of fracture in the failed specimen of Charpy impact tested Alloy 617 material fractographic investigation was carried out. This section of the chapter will bring out the type of fracture in the various aged conditions along with as-received sample. Fractographic study under SEM is also essential to know the nature of transition in fracture mode if any in the material acquired over the aging duration.

In order to substantiate the impact failure observation of the Alloys 617 on thermal aging, fractographic investigation has been carried out using SEM for the regions a) near to notch, b) middle of the specimen and c) far away from notch tip. The results obtained from the as-received is shown in Fig. 6.3 (a-c).

Morphological features that appeared in the failed specimen of Alloy 617 in its as-received condition illustrate a signature of the ductile mode of fracture. This ductile mode of fracture is manifested by the extensive fibrous dimples (cup-cones structures in fractographs). The mechanism behind the formation of cup and cone structure of a ductile material is the coalescence of a large number of microvoids.

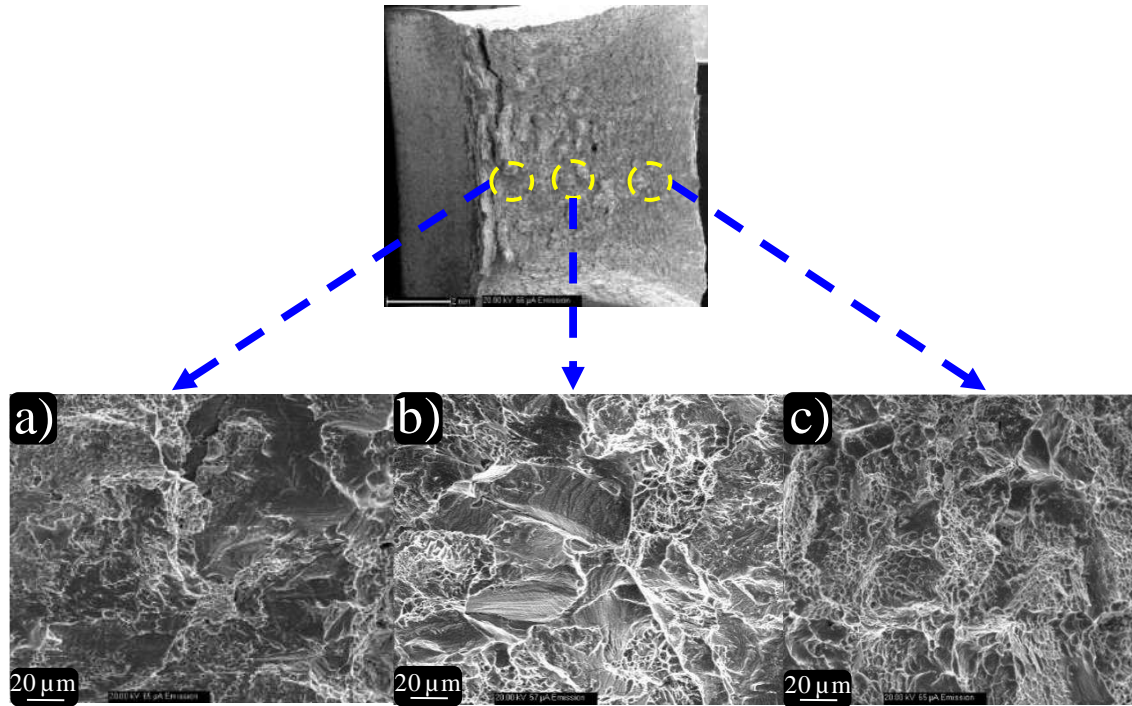


Fig. 6.3 — SEM fractographs of failed as-received Alloys 617 during Charpy impact test (a) Near to notch tip; (b) Middle of the specimen; (c) Far end of notch tip.

As can be seen from Fig. 6.3 (a), the extent of fibrous dimples gradually increases from the near notch via the middle of the specimen to far end of the notch tip.

The fractographic features appeared in the failed specimen of Alloy 617 in 1000 hours aging duration, as shown in Fig. 6.4, shows a signature of transition from predominantly ductile one to predominantly intergranular mode of fracture. This transition in fracture mode is in tandem with a sudden drop of toughness in 1000 hours aged Charpy tested sample w.r.to as-received alloy.

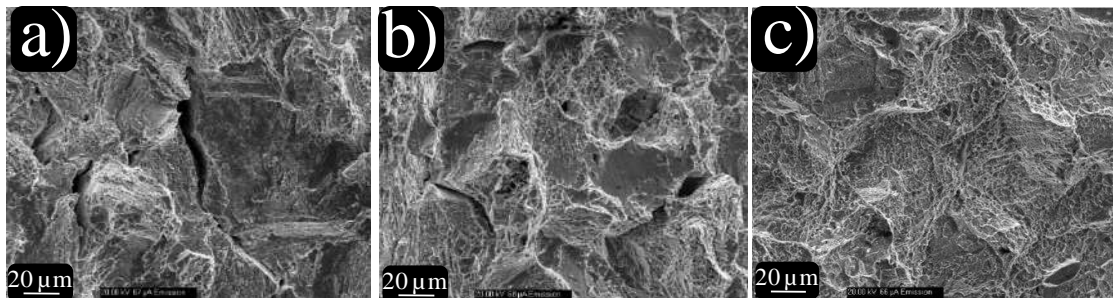


Fig. 6.4 — SEM fractographs of failed specimen unveiling the effect of aging duration on Charpy impact test for the sample aged at 1023 K for 1000 h; (a) Near to notch tip; (b) Middle of the specimen; (c) Far end of notch tip.

A mixed of failure with a greater contribution from the grain boundary cracking and least contribution from the fibrous dimples remain the salient features of the Fig. 6.4 (b). The main reason for the grain boundary cracking is attributed to the spontaneous evolution of copious amounts of carbides at the grain boundary regions as can be seen from chapter 4 in Fig. 4.9. Alloy 617 has a high propensity towards precipitation on aging treatment. This fact is also backed by the earlier results obtained by various groups [22, 55, 101].

Fractographs of failed specimen aged for 5000 hours is shown in Fig. 6.5. Morphological features that appeared in the failed specimen persuade us that there has been a substantial intergranular failure in all of the three fractographs marked as Fig. 6.5 (a-c). Longer aging duration has embrittled the grain boundary further or if not it has started to show its presence as can be seen in fractographs. The huge drop between the Charpy impact energy of 1000 hours (~130 J) and 5000 hours (~98.16) has better conformity with the fractographs.

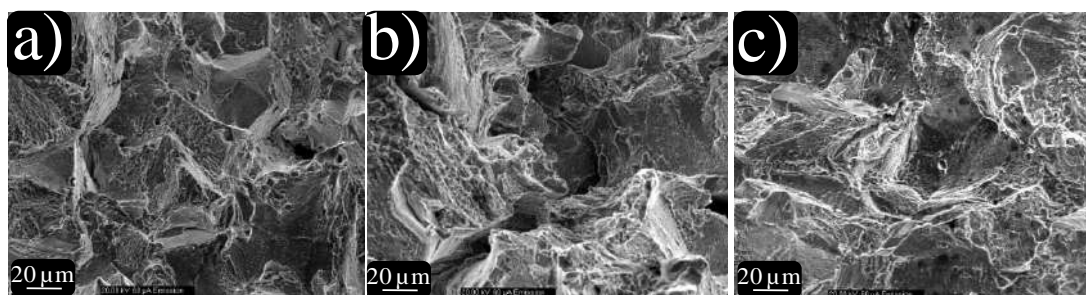


Fig. 6.5 — SEM fractographs of failed specimen unveiling the effect of aging duration on Charpy impact test for the sample aged at 1023 K for 5000 h; (a) Near to notch tip; (b) Middle of the specimen; (c) Far end of notch tip.

Morphological features that appeared in the failed specimen of Alloy 617 in 10000 hours aging duration show extensive grain boundary embrittlement as can be seen in Fig. 6.6. The presence of microcracks and microvoids act as initiation sites and provide an easy way for the crack to propagate during the Charpy impact test and ultimately lowering the fracture toughness of this material. The observations from the

Charpy impact energy which is ~ 77.6 J is very close to 50000 hours aged alloy which is ~ 98.16 [96]. This minimal difference in the Charpy energy is also reflected by the fractographs. The fractographs of the 10000 hours aged alloy show a similar fractographs as of 5000 hours aged alloy.

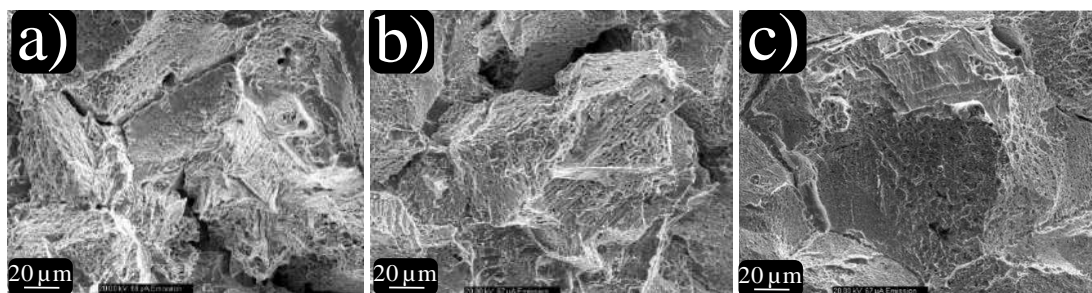


Fig. 6.6 — SEM fractographs of failed specimen unveiling the effect of aging duration on Charpy impact test for the sample aged at 1023 K for 10000 h; (a) Near to notch tip (b) Middle of the specimen; (c) Far end of notch tip.

These intergranular cracks are a response of aging-induced degradation of fracture resistance due to precipitation of carbides at the grain boundaries. Over the aging, carbides have not only grown in size, but they have populated over the entire grain boundary as can be seen from chapter 4 in Fig. 4.8 to Fig. 4.12. This condition had made the crack to initiate from most of the grain boundaries, as can be seen from Fig. 6.6 (b). The sudden impact in the Charpy test has transferred the load to the weaker section in the grains. Needless to say that in this Alloy 617 the weaker section of the grain structure is its grain boundaries, and crack initiated mostly from the embrittled grain boundaries.

Fig. 6.7 reveals the fractographs of 20000 hours aged Alloy 617. Though the aging durations from the 10000 to 20000 hours are double, the fractographs have not demonstrated much variation in their fractographs and this is in tune with Charpy impact energy too. Impact toughness value of 20000 and 10000 hours is 46 and 77.6 J, respectively. The decrement in Charpy impact energy for 20000 and 10000 hours is only 40 pct.

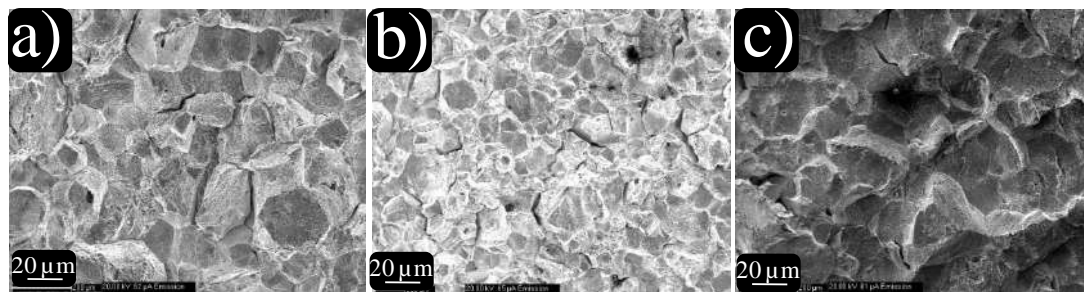


Fig. 6.7 — SEM fractographs of failed specimen unveiling the effect of aging duration on Charpy impact test for the sample aged at 1023 K for 20000 h; (a) Near to notch tip (b) Middle of the specimen; (c) Far end of notch tip.

Fig. 6.7 (a) shows the embrittled grain after 20000 hours of aging duration. The mode of failure is still via an intergranular mode of fracture which is most prominently seen in Fig. 6.7 (b) & (c). The interesting feature of Fig. 6.7 (b) is crack initiating still along the boundaries with dimples completely absent.

Finer precipitates situated at the grain boundaries can also cause embrittlement. Other superalloy families (Superalloy: 718 and 230) which closely matches our 617 has a clear proof that such embrittlement is possible. The precipitates of δ - phase (Ni_3Nb) similar to $\text{Ni}_3(\text{Al}, \text{Ti})$ found on and near the grain boundaries assists two failure mechanism leading to collapse of the crystal structure of the superalloys. The two failure mechanism are hydrogen enhanced localized plasticity (HELP) [137, 138], and the other is hydrogen enhanced decohesion (HEDE) [139, 140]. The δ -phases are the active sites to absorb hydrogen along the grain boundaries and cause severe strain at the precipitates-matrix interface. The severely strained interfaces escalate cracks initiations leading to failure.

We also further analyze fracture surfaces and establish a relationship among the fracture energy vs. the extent of fibrous features in the various aged samples. To our surprise, we find that there is a trend in the amount of fibrous area present inside the fracture surface and Charpy impact energy with little deviations owing to the impact of

grain boundary precipitates. To this end, we scrutinized the fracture surface area with the help of ImageJ (version 1.52a) the details of which are tabulated in table 6.1.

Table 6.1 Area considered for the energy from impact tests of as-received and aged conditions of Alloy 617.

| Material condition | Area considered (μm^2) | Fibrous Area (FA) | ~ % FA |
|--------------------|-------------------------------------|-------------------|--------|
| As-received | 41780.85 | 35408.99 | 84 |
| 1000 h | 40728.22 | 24377.26 | 60 |
| 5000 h | 38547.7 | 11441.07 | 30 |
| 10000 h | 44695 | 6113.78 | 14 |
| 20000 h | 152347.9 | 14296.53 | 10 |

Fig. 6.8 is a replica of the data obtained from the above table 6.1 which pushes to think that the extent of the fibrous area is in compliance with the amount of energy obtained from the Charpy impact energy shown in Fig. 6.2. Larger the fibrous area, high is the fracture energy required to break the material. For instance, 84 % fibrous area (FA) corresponds to the % fracture energy of 100 with a numerical value of ~ 285 J which being highest ever achieved in this material. The % FA results were quite consistent with the other aged samples also with slight deviations in the highly embrittled sample owing to the significant role of the precipitates being dominated by mere fibrous characteristics. The enticing feature of these data can be appreciated by its simplicity in revealing really a significant property (the values obtained from the % FA runs parallel to Charpy energy) and also closely establishing a relationship between Charpy fracture energy and SEM morphology. We also state that the intergranular area supplements the % FA in the area fraction table 6.1.

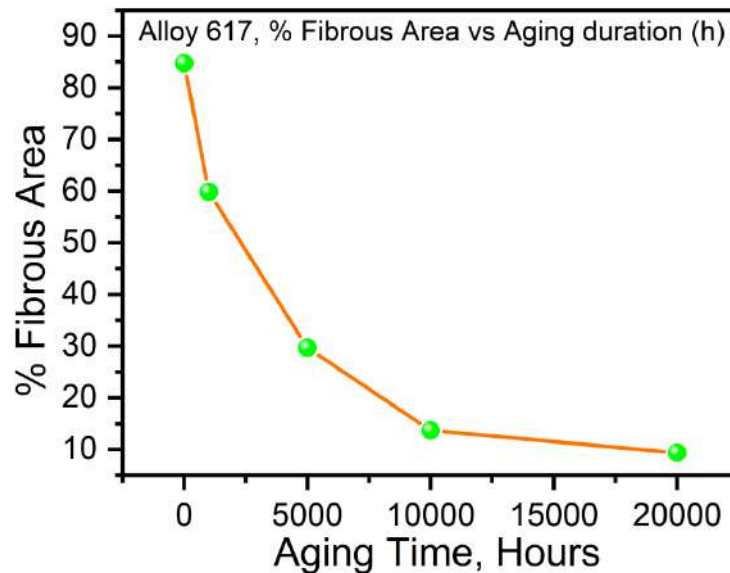


Fig. 6.8 — Graphical representation of % fibrous vs. various aging durations in Alloy 617. Area (μm^2) shown in the graph is a pictorial representation of the data obtained from table 6.1.

6.5 Peering Fracture Through the Shear Lip Formations

Shear lip formations on a fracture surface is a quantitative characteristic of fracture [141]. To understand the extent of shear lip formation and delamination we present a low magnification camera view as shown in Fig. 6.9. The dotted area marked in figures represents the formation and extent of the shear lip in various aged Charpy fractured samples. The varying nature of its formation is an indication that aging has a profound impact on this alloy. The extent of plasticity or localized plasticity near the crack tip is an indication of the material toughness which can also be viewed in terms of the shape of the shear lip formed on the Charpy fractured surfaces. The idea of establishing a relationship between Charpy samples vs. temperature on the brittle-to-ductile transition in the upper shelf region of shear lips has been well documented in the published literature [141, 142]. The area of the shear lip is an indication about the amount of the absorbed energy and bears a close relationship with the data plotted in Fig. 6.2. The larger the shear-lip area, the more significant the ductility is. Furthermore, shear-lips are a characteristic sign of the influence of the meso-level mechanisms of the processes

of deformation and failure of the material. The extent of shear lip formed in Fig. 6.9 (a) is comparatively larger than any of the shear lip formed in the other aged samples. During the extensive investigation of shear-lip areas and fracture surface of Charpy samples, a change in the appearance of shear-lips (area enclosed) are found, which are formed on their side surfaces. The development of shear lips in the 1000 hours aged alloy shown in Fig. 6.9 (b) has changed and more precisely reduced which complies with the sudden drop in Charpy impact energy as evident from Fig. 6.2. At 5000 hours aging, shear lips have a weakly developed shape (Fig. 6.9 (c)). Moreover, it was complemented by the formation of the metal delamination at the zones of shear and smaller cracks on the surface. The shear lips in Fig. 6.9 (d & e) almost disappeared, indicating that plastic deformation at the meso-level is well connected with the rotational dynamics of the conglomerates of grains, and the dissipation of energy occurs due to friction on their boundaries. One of the revelations of this is the formation of shear lips. Fig. 6.9 (f) is shown to represent the location of shear lip and crack propagation and is used for the explanation purpose only.

So, we further conclude that the decreasing Charpy energy trend is in good agreement with the shear lip formation as evident from Fig. 6.2 (a-e) and well complemented by the formation of the metal delamination and microcracks on the surface.

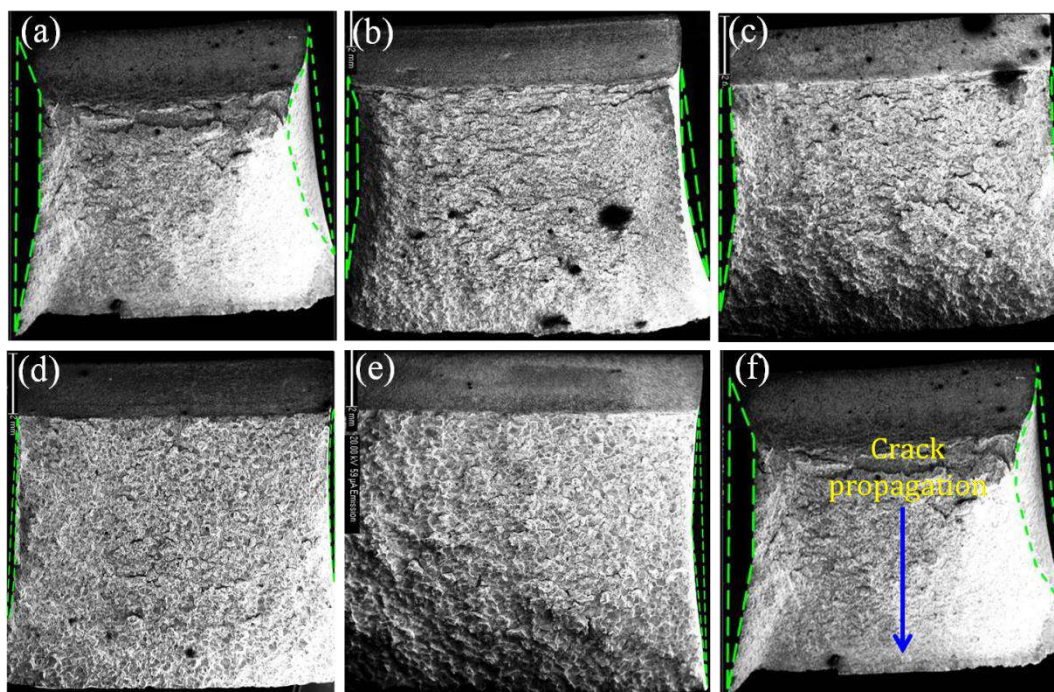


Fig. 6.9 — Shear-lip formation observed during various Charpy tested specimens of Alloy 617: (a) As-received; (b) 1000 h; (c) 5000 h; (d) 10000 h; (e) 20000 h; (f) the arrow indicates direction of crack propagation and dashed area represents the formation of shear lip.

6.6 Nature and Compositional Morphology of Precipitates on Fracture Surface

This section of the chapter deals with a detailed study of the elemental composition and the nature of precipitates near and around the crack zone. The precipitate responsible for the strengthening of the matrix and aging-induced degradation of fracture resistance of the alloy has been identified. The elemental mapping has been aptly done to get more insights into the fracture behaviour of alloy 617.

SEM elemental mapping analysis was performed to reveal the nature of the precipitates observed in the microstructure of the as-received alloy, and the results are presented in Fig. 6.10. When elemental mappings are analyzed, it is brought to notice that, the precipitates found at the grain boundary are rich in Cr, Mo, Ti, and Al elements. However, in areas, where precipitates exist, it is found that these regions are depleted in Ni and Cr elements from the matrix. However, these precipitates not only

contain these elements completely (Ni, Fe, and Cr), but above all, in the region where Mo, Ti, and Al elements are clustered, the C element also shows an accumulation. Because of an increase in the amount of C at the precipitates, it can be said that these precipitates are carbides. The common carbide types in nickel-based superalloys are MC, $M_{23}C_6$, M_6C , and M_7C_3 [143, 144].

It has been confirmed from the TEM analysis (Fig. 4.13) that carbides are Mo-rich and is Mo_2C precipitates. The origin of Mo_2C carbides can be traced back in the solution treated condition of as-received alloy. In the solution treated condition the temperature was reasonably good enough 1443 K (1170 °C), and it is well known that the higher the temperature is, the greater the atomic activation energy will be. The higher temperature favors atomic migration, leading to a large diffusion coefficient [145, 146] These carbides grew initially by taking the solutes from the matrix until its content in the matrix reached equilibrium. After that, their growth took place gradually by the mechanism of Ostwald ripening [147]. In this stage, the growth rate of carbides was governed by atomic diffusion rate.

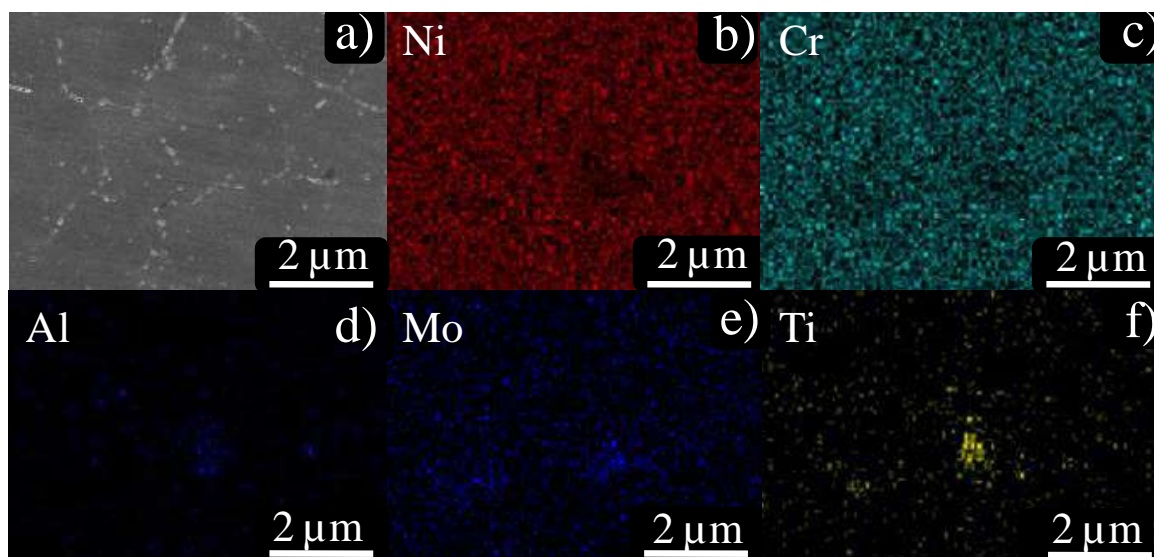


Fig. 6.10 — (a) SEM image of as-received alloy; (b-f) SEM 2D element maps of the elements extracted from EDX spectra.

Fig. 6.11 shows the images of SEM and elemental mapping analysis of the 1000 hours aged sample. Additions of alloying elements play different roles in the Ni-based superalloys with positive effects to increase the alloy strength required while operating at a very high-temperature. Of these several factors, the one making the major contribution to increasing the strength at high-temperature is the fact that they form intermetallic precipitations of different types with major elements being Ti, Al, and Nb and generally of the form $\text{Ni}_3(\text{Ti}, \text{Al}, \text{Nb})$. Alloy 617 used in this study contains Al and Ti in 1.2% and 0.4 %, respectively and a trace amount of Nb (0.02 %). When the images of the elemental mapping analysis given in Fig. 6.11 are examined, it is particularly observed that around the few small clustering at the grain boundaries the strengthening elements mentioned above show a nearly homogenous distribution. As examined under TEM in Fig. 4.15, the precipitates are rich in Al and Ti and constitute $\text{Ni}_3(\text{Ti}, \text{Al})$.

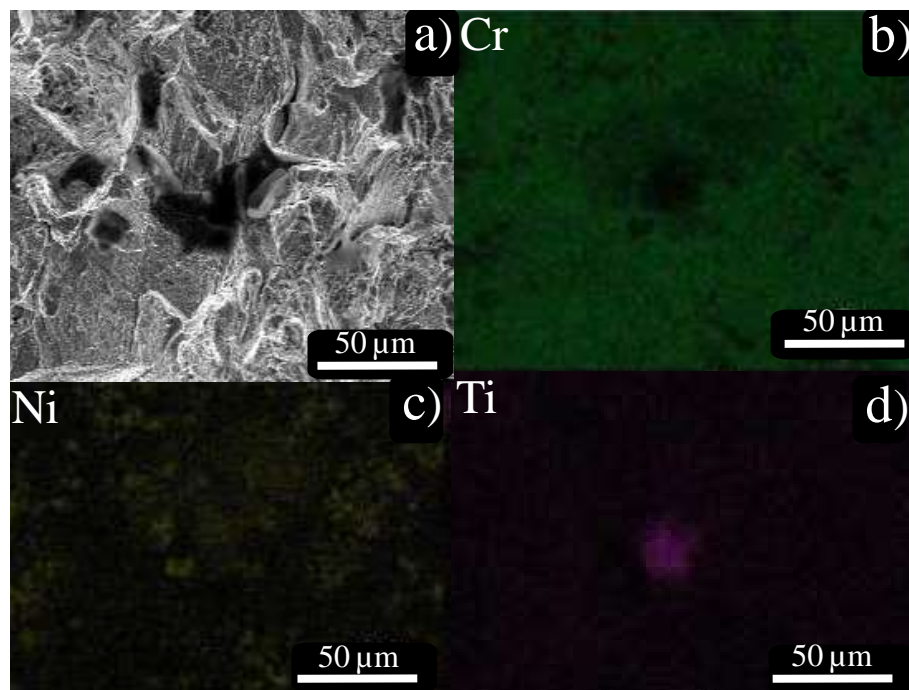


Fig. 6.11 — (a) SEM image of 1000 hours aged alloy; (b-d) SEM 2D element maps of the elements extracted from EDX spectra.

The evolved γ' commonly known as $\text{Ni}_3(\text{Ti}, \text{Al})$ as a result of aging-induced precipitations in 1000 hours aged sample also shows its presence in 5000 hours of aged alloy. Fig. 6.12 shows the images of SEM and elemental mapping analysis of the 5000 hours aged sample. In the elemental mapping analysis here too the formation of Ni_3Nb was ruled out because Nb being sufficiently low for the compound formation at this aging durations. Aging has a profound impact on Alloy 617. Aging for 5000 hours has given sufficient time to γ' to coarsen as can be seen in TEM analysis shown in Fig. 4.16. The size of γ' has increased to $\sim 70\text{-}80\text{ nm}$ from $\sim 50\text{-}70\text{ nm}$ in 1000 hours aged alloy.

In addition to γ' precipitates, elemental mapping analysis at the region close to the grain boundary has shown the presence of elements rich in Cr. It is interesting to note that the Cr mapping in Fig.6.11 (b) and 6.12 (c). The Cr has distributed nearly uniform in the region close to the grain boundary which is in particular absent in Fig.6.11 (b). The TEM investigation of the 5000 hours aged alloy shows the presence of Cr-rich precipitate and is Cr_{23}C_6 as confirmed from SAED pattern.

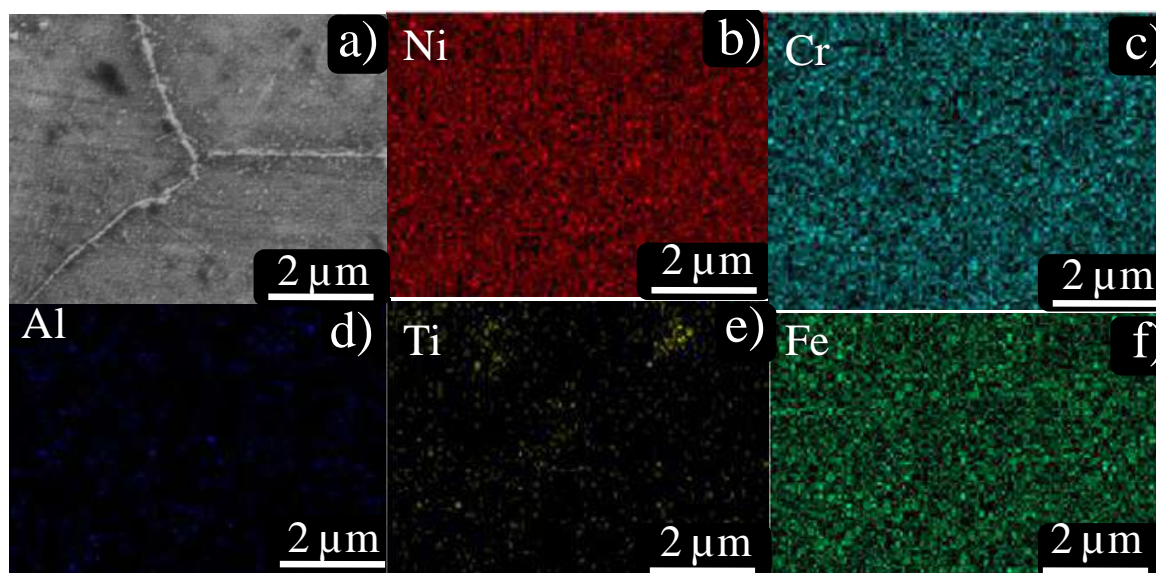


Fig. 6.12 — (a) SEM image of 5000 hours aged alloy; (b-f) SEM 2D element maps of the elements extracted from EDX spectra.

TEM images of γ' precipitates after the 10000 hours aging treatment are shown in Fig. 4.17. The morphology of γ' precipitates even after aging for 10000 hours bears the same spherical nature. Though, it can be denied that a marginal growth in the size ~ 80- 110 nm has been noticed (Fig. 4.17 (a)) w.r.to 5000 hours aged material. It is well appreciated that the presence of γ' precipitates in the matrix of an aged alloy of this material plays a crucial role in imparting strength at higher temperatures [99]. It has been concluded from the TEM investigations that the morphology of γ' precipitates hardly changes during the aging treatments. However, there are indications that it only grows in size due to thermal aging, but to a limited extent. It could also be appreciated that even this marginal change in the precipitate size may have a significant influence on the deformation characteristics of this material. The results have been validated by the SAED pattern, as shown in Fig. 4.17 (b). The elemental mapping in Fig. 6.13 has confirmed the elemental composition of γ' to be Ni-rich $\text{Ni}_3(\text{Al}, \text{Ti})$. From the mapping, it is also confirmed that the block-shaped precipitate designated as 'B' is rich in Ti and N. The precipitates of this type are primary precipitates and do not grow much over aging. From the EDS analysis in Fig. 4.8 (c) it is confirmed that precipitates are rich in Ti and could of the type $\text{Ti}(\text{C}, \text{N})$.

Not only γ' has evolved during the journey of aging, but also the carbides have sufficiently grown enough due to aging treatment. TEM results of thermally aged specimens for 10000 hours has also shown the M_{23}C_6 precipitates of size 70-80 nm as shown in Fig. 4.18 (a). SAED pattern along the [011] zone axis as shown in Fig. 4.18 (b), confirms the presence of Cr-rich M_{23}C_6 . The elemental composition (by wt pct) around the M_{23}C_6 is shown in Table 4.1.

It is also interesting to note the along with γ' and carbides another precipitate was also seen under TEM and was confirmed to be Ni_3Si shown in Fig. 4.18. Bright-field TEM image shown in Fig. 4.18 (a) of the alloy aged for 10000 hours shows some

coarser precipitates of the size 110-120 nm. From the SAED analysis, it can be inferred that the precipitates are rich in Si. Tokunaga et al. [93] have reported a similar observation of an intermetallic of Ni-Si system in Ni-Si-B ternary alloys. Crack-tip dislocations and fracture behaviour of Ni₃Si and Ni₃Al system have been reported by Yoo and group [100]. Very few reports have been published in this direction stating Ni₃Si presence in superalloys, we though found out Ni₃Si and precipitates have been confirmed from SAED pattern as shown in Fig. 4.18(b), a suitable explanation for its origin its role in Alloy 617 performances can only be said in due course of time with the availability of more TEM results.

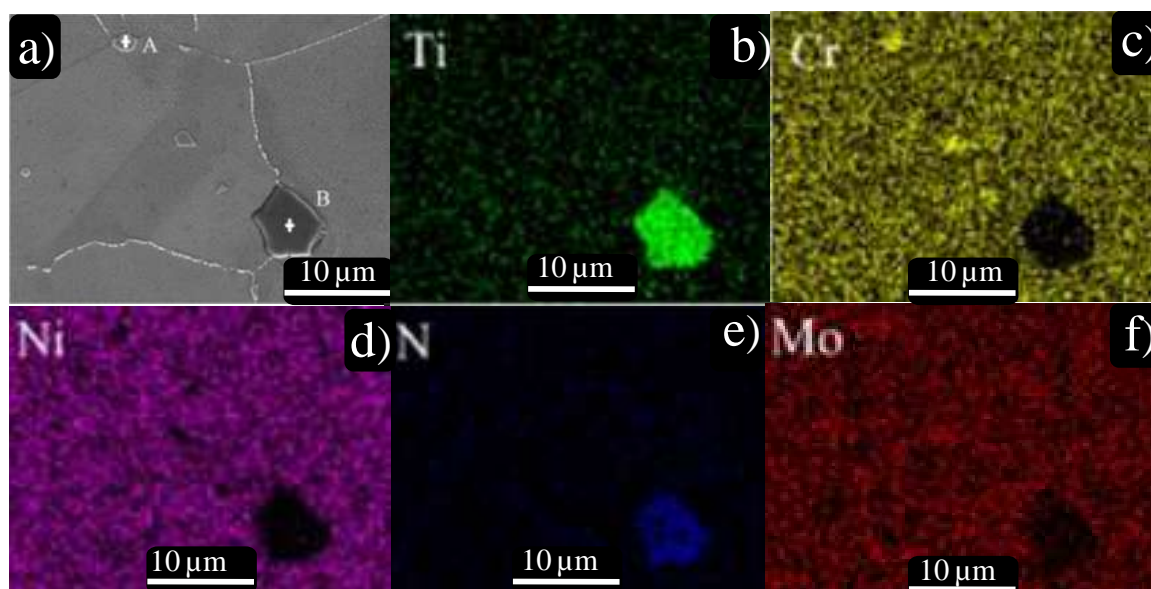


Fig. 6.13 — (a) SEM image of 10000 hours aged alloy; (b-f) SEM 2D element maps of the elements extracted from EDX spectra.

SEM images of 20000 hours aged sample after room-temperature Charpy impact test are shown in Fig. 6.7. After aging for 20000 hours, the fractographs of the aged alloy indicate predominantly intergranular cracking and failure occurred via grain boundary embrittlement. The fractographs were further analyzed in proximity to crack. This is attributed to the voluminous precipitation of carbide decorating the grain boundary and its coarsening due to aging makes the condition worse. Fig. 4.12 (b)

shows extensive carbides precipitation in proximity to the grains and on the grain boundaries that not only weakens the grain boundaries, but also serves as an initiation site for crack propagation during the Charpy impact test. In the microstructure of 5000 hours, aged condition microcracks and microvoids which have started to take place now have matured and are distinctly seen. A glance at the fractograph reveals that point of initiation of microcracks and microvoids are mostly the triple points in the microstructures which are now heavily occupied by carbides and have embrittled. The investigation regarding the crack initiation in the vicinity of the crack has always brought the presence of Cr-rich carbides. The corresponding EDS spectrum of Cr_{23}C_6 is shown in Fig. 4.12 (b).

Elemental mapping analysis of 20000 hours aged alloy is shown in Fig.6.14. It can be seen from the element mapping that the elements have distributed themselves uniformly in the matrix. By this time it is easy to interpret from the element mapping of this material that 20000 hours aged alloy contains Cr-rich and Mo-rich precipitates. The presence of uniform Ti in the elemental map confirms that the primary precipitates $\text{Ti}(\text{C}, \text{N})$ has not grown much in size over the aging duration.

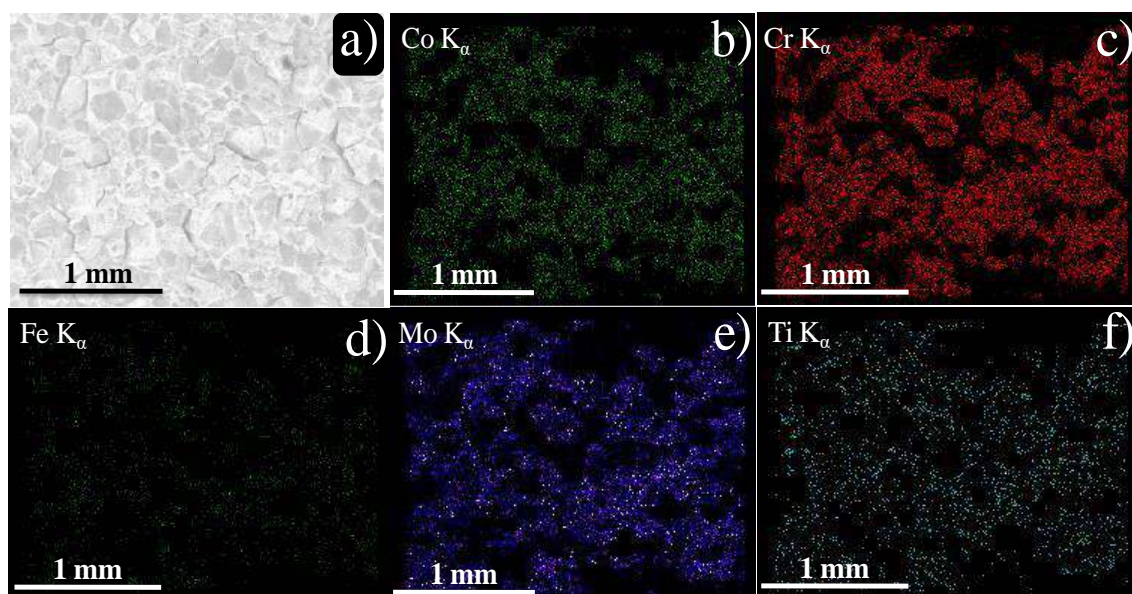


Fig. 6.14 — (a) SEM image of 20000 hours aged alloy; (b-f) SEM 2D element maps of the elements extracted from EDX spectra.

From the above observation of elemental analysis for the as-received and aged Alloy 617 it can be inferred that different precipitates forms at and the interior of the grains ultimately giving rise to the hardening of the matrix and the embrittlement of the materials. The substantial presence of $M_{23}C_6$ as observed in the SEM and TEM micrographs, preferentially at the grain boundaries has been further vindicated from the elemental analysis of the aged specimens. Though the presence of carbonitride has been shown in Fig. 6.13, its presence is minimal as compared to $M_{23}C_6$. Thus the influence of this to embrittlement could be minor as compared to the influence of $M_{23}C_6$ as seen from the 20000 hours in Fig. 6.14. This observation corroborates well with the earlier inference on the strong influence of preferential grain boundary redistribution and coarsening of $M_{23}C_6$ carbides after prolong aging treatments leading to grain boundary embrittlement.

Coherency strengthening is anticipated when there exists a difference between lattice parameters of the matrix and precipitate thus generating a strain field to be set up surrounding the precipitate [148]. Coherent/incoherent precipitates are expected to alter the mechanical properties to a greater extent [149, 150]. From the earned wisdom, it is known that material with high toughness tends to offer less fracture energy. The material with, initially coherent precipitates increase its hardness owing to an increased strain field in the matrix. Due to prolong aging the coherency is destroyed and the material hardness is lost. Increasing the hardness and the yield strength by precipitation makes the alloy more brittle and decreases the impact toughness since less plastic work can be done before strain in the plastic zone is sufficient to fracture the test specimen. The specimen with the lowest impact toughness corresponds to the highest values of hardness.

6.7 Estimation of *J*-R Curve from Charpy V-notch Impact Energy

6.7.1 Introduction

When a material exhibits completely ductile behaviour its resistance to crack extension is usually represented in the form of an elastic-plastic crack growth resistance curve (R curve). In essence the R curve is a plot of the variation in crack growth resistance, generally expressed in terms of crack tip opening displacement (CTOD) or J , during the process of stable crack extension [151]. Dynamic J -R curves are a design requirement to guard against fracture under accidental loading conditions. The determination of these curves from an instrumented impact testing [142] of Charpy V-notch specimens is very useful due to small specimen size, ease of testing, and sufficiency of the simple pendulum testing machine.

6.7.2 Experimental Procedure

Charpy V-notch specimens have been fabricated from as-received and all aged conditions of Alloy 617. The schematic representation of a standard Charpy V-notch specimen is given in Fig 6.1. Impact testing of these Charpy V-notch specimens has been carried out at room temperature at an initial impact velocity of 5.12 m/s. The capacity of the pendulum testing machine is 358 J (shown in Fig. 3.12). A total of three tests has been carried out for each condition of the material. The Charpy energy (KV) for each test and the average Charpy energy for each condition are given in Table 6.2. The graph of which is already drawn in Fig. 6.2 and section 6.3 of this chapter.

Table 6.2 Charpy energy from impact tests of as-received and aged condition of Alloy 617.

| Sr. No. | Material condition | Charpy Energy (J) | Avg. Charpy Energy (J) |
|---------|--------------------|-------------------|------------------------|
| 1. | As-received | 265 | 285 |
| | | 274 | |
| | | 328 | |
| 2. | 1000 h | 123 | 130 |
| | | 130 | |
| | | 136 | |
| 3. | 5000 h | 93 | 98 |
| | | 95 | |
| | | 107 | |
| 4. | 10000 h | 77 | 77 |
| | | 78 | |
| | | 79 | |
| 5. | 20000 h | 45 | 46 |
| | | 46 | |
| | | 47 | |

6.7.3 Methodology for Estimation of J -R curve from Charpy V-notch Impact Energy

The J -R curve is defined for fracture mechanics specimens having a sharp fatigue pre-crack. In this case, the J -integral determines the crack-tip stress and strain fields. Hence, the determination of the J -R curve from a blunt V-notch has to be logically deduced from the equations defined for a sharp fatigue pre-cracked fracture mechanics specimen. Another point to be mentioned is that standard formulae for J -R curve determination require load-displacement triplets along with the entire test. While all these are available in a quasi-static test, the current crack length is not available in a dynamic impact test. Hence, the J -R curve equation has to be deduced for an impact tested pre-cracked Charpy specimen from available results from the load-displacement trace like total Charpy energy, peak load Charpy energy, etc. This has been deduced by brilliant equations given by Schindler, and the curve is well known as Schindler's curve [152-154] and applied successfully to characterize the effect of cold work on various metals and alloys for instance: P9 steel in [155].

The J - R curve can be divided into two phases. In Phase I, before the peak load, the J -resistance curve is J -controlled. Subsequently, crack growth is governed by a constant crack tip opening angle (CTOA). The latter can be obtained from the energy consumed in the tearing phase between maximum force and complete fracture. The J - R curve in phase 1 is given below:

$$J(\Delta a) = C * (\Delta a)^p \dots \dots \dots \Delta a < \Delta a_m \quad (6.1)$$

where Δa crack extension, C and p is are material-dependent constant.

CTOA is mathematically related to the slope of the J - R curve in the first part of the tearing process. From this condition, C , p , and Δa_m can be obtained. Δa_m is the crack extension at maximum load.

$$C = \left(\frac{2}{p}\right)^p * \frac{na_0}{B(W-a_0)^{1+p}} * W_t^p * W_{mp}^{1-p} \quad (6.2)$$

$$p = \frac{3}{4} * \left(1 + \frac{W_{mp}}{W_t}\right)^{-1} \quad (6.3)$$

$$\Delta a_m = (W_{mp} * p * b_0) / (2 * W_t) \quad (6.4)$$

where C is non dimensional constant, a_0 is the initial crack length, B is specimen thickness, W is specimen width, b_0 is the ligament length, W_t is total fracture energy, W_{mp} is plastic part of W_m

$$\eta = 13.81 * \frac{a}{W} - 25.12 * \frac{a^2}{W} \text{ for } 0 < a/W < 0.275 \quad (6.5)$$

The condition at maximum load can be given as follows:

$$\frac{dF}{d\Delta a} (\Delta a = \Delta a_m) = 0 \quad (6.6)$$

where F is force, Δa crack extension and Δa_m crack extension at maximum load.

$$J \propto \left(\frac{F}{F_0}\right)^{1+1/n} \quad (6.7)$$

n is hardening exponent according to the material law

$$\sigma = A * \varepsilon^n \quad (6.8)$$

F_0 is plastic limit load, which depends on the actual ligament width $b = b_0 - \Delta a$

according to

$$F_o \propto (b_0 - \Delta a)^2 \quad (6.9)$$

From equations 1, 7 & 9, the following equation for Δa_m can be obtained

$$\Delta a_m = \frac{n * p * b_0}{2} \quad (6.10)$$

Comparing equations 10 & 4, one obtains

$$W_m \approx W_{mp} = n * W_t \quad (6.11)$$

The hardening exponent n is approximately equal to the uniform fracture strain in a tensile test.

$$n \approx A_g \quad (6.12)$$

Where A_g is uniform fracture strain.

$$J(\Delta a) = \left(\frac{2}{p}\right)^p * \frac{\eta(a_0)}{B(W-a_0)^{1+p}} * W_t^p * A_g^{1-p} * \Delta a^p \quad (6.13)$$

$$p = \frac{3}{4} * (1 + A_g)^{-1} \quad (6.14)$$

Equation. 13 enables determination of J -R curve just the total fracture energy and the uniform fracture strain. Inputting $W = B = 10$ and $b_0 = 2$ mm for the Charpy specimen gives $\eta = 1.76$ thus, equation 13 simplifies to:

$$J(\Delta a) = 11.44 * KV * (A_g)^{1/3} * \Delta a^{2/3} \quad (6.15)$$

where J is J integral, KV is Charpy fracture energy; A_g is uniform fracture strain and Δa crack extension.

The blunting line can be given as:

$$J = s_1 * \Delta a = 3.75 * R_m * \Delta a \quad (6.16)$$

where J is J integral, R_m is ultimate tensile strength and, Δa crack extension.

J at crack initiation can be obtained as an engineering evaluation in three different ways. J_0 is obtained by the intersection of the linear extrapolation of the J -R curve from the range $\Delta a > \Delta a_m$ to the intersection with the blunting line. $J_{0.2}$ is the value

of J at $\Delta a = 0.2$. $J_{0.2t}$ is the J value at a distance of 0.2 mm from the intersection with the blunting line. From these definitions the three quantities are obtained as follows:

$$J_0 = \frac{7.33 * KV * A_g}{1 - 1.47 \frac{KV}{R_m}} \quad (6.17)$$

$$J_{0.2} = 3.92 * KV * (A_g)^{1/3} \quad (6.18)$$

$$J_{0.2t} = 11.44 * KV * (A_g)^{1/3} * \left[\left(\frac{3.05 * KV}{R_m} \right)^3 * A_g + 0.2 \right]^{2/3} \quad (6.19)$$

6.7.4 Interpretation of J -R Curve

J -R curves have been calculated according to equation 6.15 for the as-received and aged condition of Alloy 617. The average Charpy energy for each condition of the material was used to estimate the J -R curve. The average Charpy energy, uniform plastic strain from the tensile test (A_g), and crack extension at peak load (Δa_m) are given in Table 6.3. The J -R curve is given in Fig 6.15. There is a drastic reduction in fracture toughness from the as-received condition to the material aged for 1000 hours owing due to the voluminous precipitations in this alloy. Further aging time results in a progressive reduction of fracture toughness, but to a much smaller degree. The reason for the drastic difference in the as-received and the aged alloy incurred due to the propensity of this material for precipitations. Though this material is a solid solution strengthened material, it often gets its strengthening share from precipitates too. These J -R curves as derived from equation 1 are based on the assumption that the validity holds only up to crack extension at maximum load. It is to be noted that the curves of the as-received material is very steep while all the aged conditions show much shallower J -R curves.

The 3 measures of engineering estimation of crack initiation J calculated according to equations 6.17, 6.18 & 6.19 are given in Table 6.2. The requirement of

having an engineering estimation is due to the difficulty in exactly identifying crack initiation which occurs after prior crack tip blunting.

J_0 , $J_{0.2}$, and $J_{0.2t}$ are given in Table 6.2. It can be seen that $J_{0.2}$ is the conservative value for as-received material while J_0 is conservative for all the aged conditions. Also, as can be made out from the J -R curve all the 3 measures of crack initiation J are within maximum allowable crack extension (peak load). Thus the $J_{0.2}$ and J_0 obtained are valid for as-received and aged conditions respectively.

Table 6.3 KV, A_g , Δa_m , UTS, and crack initiation J values for as-received and aged conditions of Alloy 617

| Material condition | KV (J) | A_g | Δa_m (mm) | UTS (MPa) | J_0 (kJ/ m ²) | $J_{0.2}$ (kJ/ m ²) | $J_{0.2t}$ (kJ/ m ²) |
|--------------------|--------|-------|-------------------|-----------|-----------------------------|---------------------------------|----------------------------------|
| As-received | 285.17 | 0.39 | 0.85 | 1251.4 | 1248.86 | 824.33 | 1154.4 |
| 1000 h | 127.33 | 0.28 | 0.66 | 1543.2 | 305.19 | 330.73 | 334.22 |
| 5000 h | 98.16 | 0.26 | 0.63 | 1721.0 | 209.38 | 248.75 | 248.71 |
| 10000 h | 77.6 | 0.27 | 0.64 | 1481.7 | 169.71 | 198.76 | 198.56 |
| 20000 h | 46.0 | 0.24 | 0.58 | 1496.8 | 84.84 | 112.63 | 112.13 |

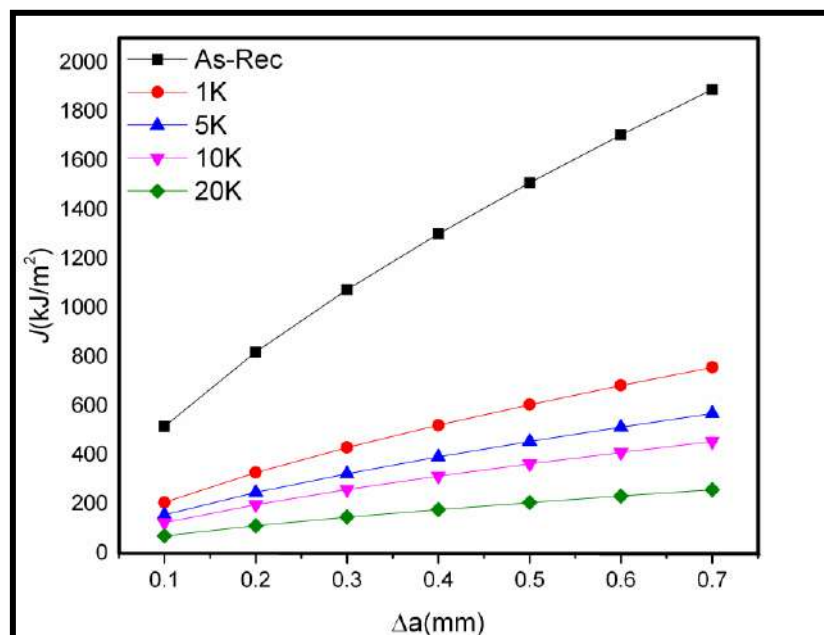


Fig. 6.15 — J -R curves for as-received and aged conditions of Alloy 617.

6.7.5 Validation of *J*-R Curve from Instrumented Charpy Impact Testing System

To begin with, *J*-R curve validation assisted by instrumented Charpy test, a small description regarding the instrumentation will be useful to look upon detailed in section 3.6.4. The instrumented Charpy system is an extension of Charpy impact machine and more sophisticated technique working on the principle of displaying the change in kinetic energy from a vertically dropped accelerated mass on the specimen [156]. With the progress in the instrumentation, the load-time data changed to load-displacement data from the drop weight instrumentation system. The load-displacement has removed the complexities of compliance corrections. The standard agreement between acceptable fracture toughness obtained from the Charpy V-notch specimen through instrumented drop weight systems is detailed elsewhere [156, 157]. The load-displacement curve for the as-received and aged material with an applied velocity of 5 m/s is shown in Fig 6.16 (a-f).

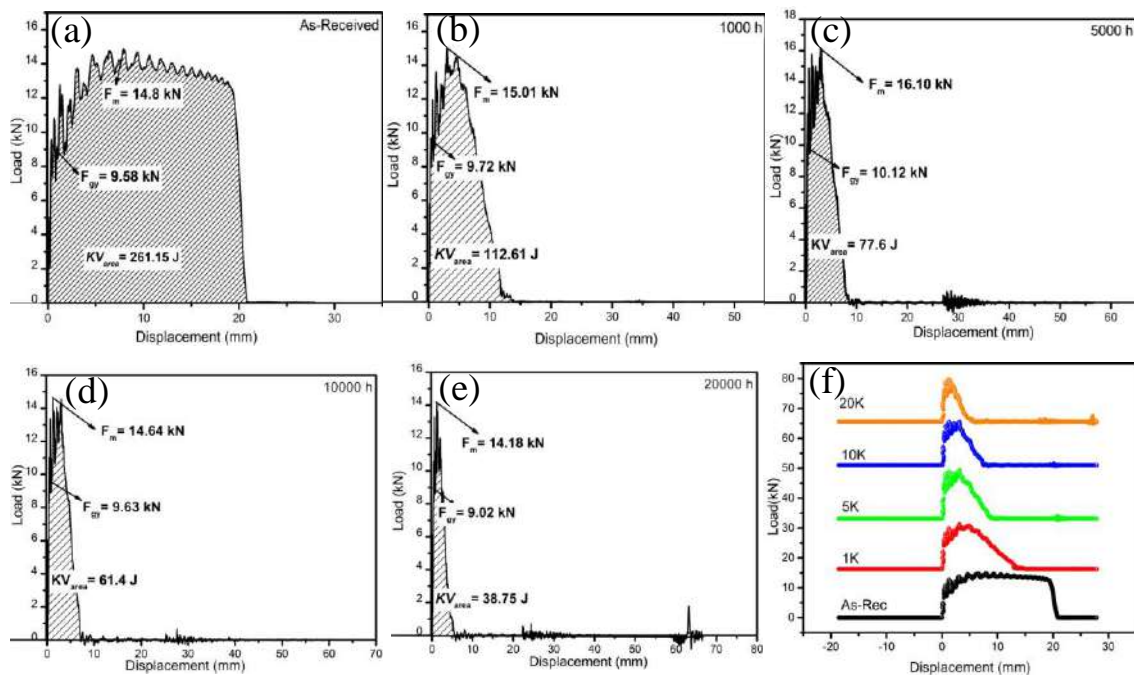


Fig. 6.16 —Load-displacement curves for as-received and aged condition of Alloy 617 obtained from instrumented Charpy impact testing system.

Though the mathematical formulation has been achieved with acceptable values of the fracture toughness earlier via Schindler's curve, here validation from actual quasi-static tests achieved from the instrumented Charpy is detailed. The procedure to obtain actual J -R curves from the instrumented Charpy has been in trend recently, and hence very few documents have been published in this direction [158]. An effort has been made to extract precise data from the load-displacement curve and is documented in Table 6.3. These data have been used to plot the J -R curve identical to the previous curve as in Fig. 6.15. The as-obtained J -R curve is shown in Fig. 6.17. The graph shown in Fig. 6.17 indicates that fracture energy follows a clear unusual trend in the Alloy 617, which is also supported by the yield force (F_{gy}) and maximum force (F_m) data shown in Table 6.4.

Table 6.4 Results of instrumented testing system for Alloy 617 in its as-received and aged conditions.

| Material conditions | KV (J) | F_{gy} (kN) | F_m (kN) | J_0 (kJ/ m ²) | $J_{0.2}$ (kJ/ m ²) | $J_{0.2t}$ (kJ/ m ²) |
|---------------------|--------|---------------|------------|-----------------------------|---------------------------------|----------------------------------|
| As-received | 261.15 | 9.58 | 14.8 | 1097.1 | 754.9 | 990.72 |
| 1000 h | 112.61 | 9.72 | 15.01 | 265.67 | 292.5 | 294.22 |
| 5000 h | 77.6 | 10.12 | 16.10 | 162.41 | 196.65 | 196.15 |
| 10000 h | 61.4 | 9.63 | 14.64 | 131.99 | 157.27 | 156.82 |
| 20000 h | 38.75 | 9.02 | 14.18 | 70.94 | 94.88 | 94.43 |

A wealth of information can be extracted from Table 6.3. The KV (J) and F_{gy} (kN) values show an unusual behavior of alloy in the as-received and also in aged conditions. A precursory look at the table suggests that KV value show a gradually decreasing trend while F_{gy} shows an increasing trend till 5000 hours and then a decline in the value for remaining conditions. Yield strength has shown a rise due to its dependence over obstacle densities [159]. In as-received conditions the dislocation-dislocation interaction is small due to less or fewer precipitates formed after the annealed condition. Having already discussed that this material shows a higher propensity towards precipitations and precipitations does occur immediately after aging

is a strong responsible factor for an increase in the F_{gy} values. After 5000 hours of aging a situation arises where precipitates have reached a substantial size and it is time to get dissolve in the matrix creating a favorable time for the evolution of new precipitates as evident from the TEM image analysis shown in chapter 4 section 4.5. As evident from the published data for the other materials associations with precipitation during artificial aging, that after certain particular size of the precipitates evolved during the aging, the precipitates tend to emancipate dislocation easily due to their athermal obstacles for dislocations [159].

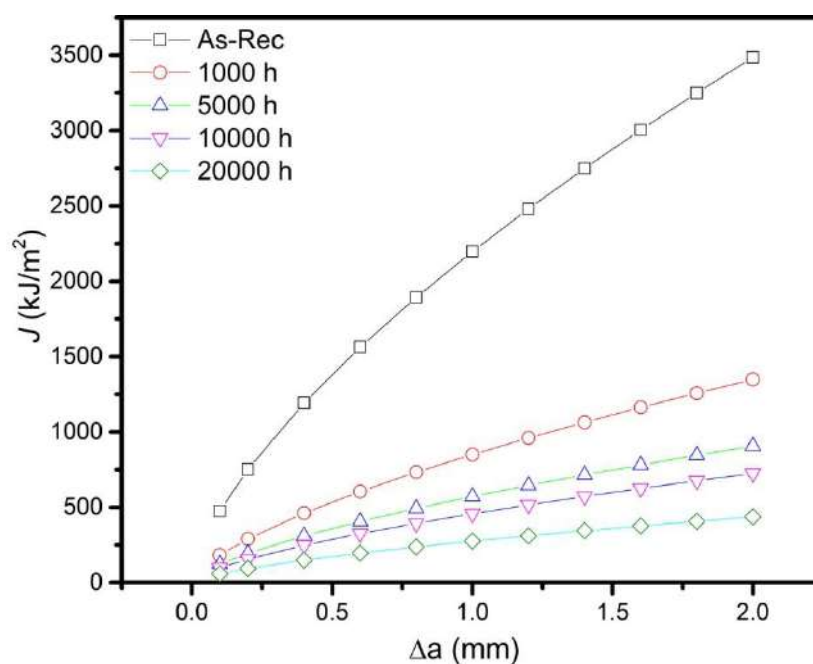


Fig. 6.17 — J - R curves for as-received and aged condition of Alloy 617 obtained from instrumented Charpy impact testing system.

6.8 Summary

The analysis of our experimental results confirms that the impact energy of the material Alloy 617 has been severely degraded due to aging. The fractographic observations also reveal a change of the fracture mode from predominantly ductile nature to predominantly intergranular cracking as the aging time increases from 1000 to 20000 hours. It is well known that the impact energy at room temperature of any material, as determined by conventional Charpy test, consists of two components: (a) energy

required for crack initiation and (b) energy required for crack propagation. Both of these components to fracture energy are significantly influenced by the inherent microstructural features. Where the crack initiation energy is generally affected by nature, size, and shape of the precipitates which are being evolved during the aging at high-temperature for this material, the crack propagation energy are often controlled by the grain size distribution and the grain boundary strength. Further, the strength of the matrix often plays a crucial role, as it is generally argued that a stronger matrix keeps a propagating crack sharper, thus demanding less energy to propagate. The inverse behavior of strength and toughness in conventional structural materials corroborates with this idea. Further, where the γ' has been precipitated randomly (within the grain and also in boundaries), the $M_{23}C_6$ has been precipitated mainly in the grain boundaries. From these observations, this can be argued that the γ' is basically contributing to increase the strength of the matrix, which in turn is leading to the lower fracture energy of the material by making the crack propagation process easier. Contrary to this, the role of $M_{23}C_6$ is more towards the crack initiation energy. It is well known that the crystal structure of the $M_{23}C_6$ is different from that of the FCC matrix of Alloy 617. So these precipitates will act as a barrier to the dislocation motion, which is a precursor for any crack initiation process. Further, the effect of these carbides on crack initiation would be enhanced as they became coarser during aging and their preferential segregation to the grain boundaries. Eventually, this has made the grain boundary an easy source of crack initiation and, thus, promoting the intergranular fracture in this material.

Dynamic J -R curves have been obtained from Charpy V-notch impact tests for as-received and aged condition of Alloy 617. The J -R curve of Alloy 617 shows a drastic decrease after the aging time of 1000 hours. Further aging durations result in a progressive decrease of J -R curve but to a much smaller degree. Valid crack initiation J

values have been obtained for both as-received and all aged conditions of Alloy 617 and they show the same trend as the J -R curve.

Brief Summary of Thesis and Scope for Future Work

This chapter provides salient features and noteworthy conclusions derived from the results of the study carried out on Alloy 617, the material developed for advanced ultra-supercritical thermal power plant. The aging-induced microstructural evolution and its influence on various mechanical properties have been summarized in this chapter. Apart from this, we have also bridged the existing gap on various opinions prevailing relating to the microstructural evolutions and coarsening behavior of γ' , and suggestions are provided for additional work to be continued in the near future.

7.1 Summary

The work carried out in this thesis reports a detailed study on Alloy 617, currently one of the potential high-temperature candidate material across the country and the globe. The outcome of the current work can be seen as the torchbearer to designers of the advanced ultra-supercritical thermal power plant. Having accomplished the task and to conclude the final chapter of the thesis, this chapter will try to brief the journey taken along this mission, and few unmet issues are kept in the priority list to be carried out in the near future.

A brief introduction about the challenges of menacing global warming across the globe, concern over raising the operating temperatures of the current thermal power plant, and challenges pertaining to the future high-temperature material is outlined in chapter 1. The motivation and objective of the study on the deformation and fracture behavior of Alloy 617 are briefed in this chapter.

An exhaustive literature review about the materials developed for high-temperature applications and specific attention has been given to Alloy 617 as a potential candidate material for advanced ultra-supercritical thermal power plants, properties, and the challenges to improve it further are also outlined in chapter 2.

Chapter 3 features the experimental techniques used in this thesis for material characterization with their basic principle of operation and the major components of the instruments. The technical specifications with schematic or real images of the available facilities at IGCAR are also shown.

A detailed microstructural characterization of Alloy 617 accomplished both in as-received and the aged condition has been the subject matter of chapter 4. From the light microscope characterization results, it has been found that the overall grain size distribution during the entire aging duration remains almost constant. The duplex nature of grain size distribution has also been less prominent in the aged material. The notable feature of this alloy is its propensity to release precipitates even for the aging duration of 1000 hours. The aging-induced precipitates can be categorized into two major types, namely $M_{23}C_6$ and γ' i.e. $Ni_3(Ti, Al)$ with traces of Ni_3Si . TEM investigation of this material has brought out invaluable information regarding aging-induced microstructural changes in the material. As-received material shows only Mo-rich and Cr-rich precipitates and no sign of γ' phase. Aging caused an evolution of γ' precipitates but with morphology rarely changed over the entire span of aging. Though a slight coarsening can be seen over periods of aging, but the change is insignificant. A significant finding of this thesis is Ni_3Si precipitates which were never reported in earlier investigations on this material. Though in the present capacity, we have limited proof of its origin and its influence on the material property is yet to be evolved during our further intensive HRTEM investigations.

The detailed studies of the effect of thermal aging on the hardness, tensile behaviour, and instantaneous work hardening of Alloy 617 and their correlation with microstructure are discussed in Chapter 5. The thermal aging of Alloy 617 is accompanied by precipitation of γ' precipitates, which strongly influences the hardness and tensile properties of this alloy after different aging durations. The absence of annealing twins in the aged specimens indicates toward an aging-induced increase of stacking fault energy. This alloy exhibits anomalous work hardening characteristics for the different aged conditions. There has been a sudden rise in the work hardening from as-received to 1000, 5000, and then a sudden drop at 10000 hours. The anomalous decrease in yield stress between 5000 and 10000 hours aging duration is attributed to the ease of dislocation movement in this regime owing to the combined effect of coarsening of γ' precipitates and the rise in stacking fault energy. Alloy 617 exhibits three distinct stages of work hardening in the plot of θ vs. σ for all the four heat-treated conditions. The three stages of work hardening are observed for all aged specimens. An initial transient stage (TS), where θ decreases rapidly, the stage II is more prominent in as-received and 1000 hours and remains almost constant for other conditions of aging conditions and a stage III where θ gradually decreases.

The influence of aging on fracture resistance of Alloy 617 and the prediction of the J -R curve has been the subject matter of Chapter 6. The analysis of our experimental results confirms that the impact energy of the material Alloy 617 has been severely degraded due to aging. The fractographic observations also reveal a change of the fracture mode from predominantly ductile nature to predominantly intergranular cracking as the aging time increases from 1000 to 20000 hours. Further, where the γ' has been precipitated randomly (within the grain and also in boundaries) the $M_{23}C_6$ has been precipitated mainly in the grain boundaries. From these observations this can be argued that the γ' is basically contributing to increase the strength of the matrix, which

in turn is leading to the lower fracture energy of the material by making the crack propagation process easier. Contrary to this, the role of $M_{23}C_6$ is more towards the crack initiation energy. It is well known that the crystal structure of the $M_{23}C_6$ is different from that of the FCC matrix of Alloy 617. So these precipitates will act as a barrier to the dislocation motion, which is a precursor for any crack initiation process. Further, the effect of these carbides on crack initiation would be enhanced as they became coarser during aging and their preferential segregation to the grain boundaries. This, in turn, has made the grain boundary an easy source of crack initiation and, thus, promoting the intergranular fracture in this material. Dynamic J -R curves have been obtained from Charpy V-notch impact tests for as-received and aged conditions of Alloy 617. The J -R curve of Alloy 617 shows a drastic decrease after aging time of 1000 hours. Further aging durations result in progressive decrease of J -R curve, but to a much smaller degree. Valid crack initiation J values have been obtained for both as-received and all aged conditions of Alloy 617. They show the same trend as the J -R curve. Efforts in the direction to evaluate the fracture strength by Instrumented Charpy test have also been given ample space in this chapter. These findings well corroborate the material performance and data obtained from the various instruments.

7.2 Scope for Future Work

For the extension of the thesis in the near future few notable areas has been chosen after the suggestions of doctoral committee members and reviewers and the key areas are:

Though the formation of Ni_3Si has been reported in chapter 4 of the thesis and has been confirmed with sufficient proofs from the SAED pattern associated with the EDS spectrum confirming the precipitates to be rich in Ni and Si. A detailed analysis regarding origin, formation and its impact on fracture resistance is a matter of interest

to us in the near future. An intensive HRTEM analysis added with J-MatPro analysis can lead us to better understand the functionality of Ni_3Si in our material Alloy 617.

Other aspects that can be kept in the list of future work in the direction of the thesis is a prolonged duration of aging, longer duration aging can give a better insight into the material relating the microstructural evolution and its influence on various mechanical properties viz: hardness, tensile and Charpy impact energy analysis.

Calculation of stacking fault energy is still an important task ahead of us to be looked upon. Knowing the fact that FCC material for the high-temperature application, especially superalloys have low stacking fault energy (SFE), its variation with aging time duration can be an excellent area to be worked upon. A wealth of information can be obtained by displaying Alloy 617 to varying temperatures, which can be a new arsenal to designers.

The assistance of the Finite element method in terms of correlating the sizes of the voids with stress triaxiality can add more information to the material.

References

- [1] D. Butler, Architecture: Architects of a low-energy future, *Nature News* 452(7187) (2008) 520-523.
- [2] D. Tytko, P.-P. Choi, J. Klöwer, A. Kostka, G. Inden, D. Raabe, Microstructural evolution of a Ni-based superalloy (617B) at 700 C studied by electron microscopy and atom probe tomography, *Acta metall.* 60(4) (2012) 1731-1740.
- [3] C.L. Cássio, I.C.P. Sebastião, The Carnot cycle and the teaching of thermodynamics: a historical approach, *Phys. Educ.* 51(5) (2016) 055013.
- [4] J. Butler, Carnot's Cycle and the Efficiency of Heat Engines, *Nature* 116 (1925) 607-608.
- [5] A. Khadse, M. Qayyumi, S. Mahajani, P. Aghalayam, Underground coal gasification: A new clean coal utilization technique for India, *Energy* 32(11) (2007) 2061-2071.
- [6] A.-V. Ruzette, L. Leibler, Block copolymers in tomorrow's plastics, *Nat. Mater.* 4(1) (2005) 19.
- [7] A.N. Singh, R.D. Thakre, J.C. More, P.K. Sharma, Y. Agrawal, Block Copolymer Nanostructures and Their Applications: A Review, *Polym. Plast. Technol. Eng.* 54(10) (2015) 1077--1095.
- [8] I. Barnes, Upgrading Efficiency of World's Coal Fleet to Reduce CO₂ Emissions. 2016 (accessed 19/02/2016.2017).
- [9] A. Zolochovsky, A. Galishin, S. Sklepus, G.Z. Voyiadjis, Analysis of creep deformation and creep damage in thin-walled branched shells from materials with different behavior in tension and compression, *Int. J. Solids Struct.* 44(16) (2007) 5075-5100.
- [10] T.-K. Yeh, H.-P. Chang, M.-Y. Wang, T. Yuan, J.-J. Kai, Corrosion of Alloy 617 in high-temperature gas environments, *Nucl. Eng. Des.* 271 (2014) 257-261.

- [11] P. Ganesan, G.D. Smith, D.H. Yates, Corrosion Resistance of INCONEL Alloy 617 in Simulated Gas Turbine Environments, Cologne, Germany, 1992, p. V005T12A004.
- [12] J. Bugge, S. Kjær, R. Blum, High-efficiency coal-fired power plants development and perspectives, *Energy* 31(10) (2006) 1437-1445.
- [13] P. Ennis, A. Czyrska-Filemonowicz, Recent advances in creep-resistant steels for power plant applications, *Sadhana* 28(3-4) (2003) 709-730.
- [14] C.M. Rae, R.C. Reed, The precipitation of topologically close-packed phases in rhenium-containing superalloys, *Acta metall.* 49(19) (2001) 4113-4125.
- [15] T.S. Jo, S.-H. Kim, D.-G. Kim, J.Y. Park, Y. Do Kim, Thermal degradation behavior of inconel 617 alloy, *Met. Mater. Int.* 14(6) (2008) 739.
- [16] P. Caron, T. Khan, Evolution of Ni-based superalloys for single crystal gas turbine blade applications, *Aerosp. Sci. Technol.* 3(8) (1999) 513-523.
- [17] R. Viswanathan, Advances in Materials Technology for Fossil Power Plants: Proceedings from the Fifth International Conference, October 3-5, 2007, Marco Island, Florida, USA, ASM International 2008.
- [18] A. Schnaas, H. Grabke, High-temperature corrosion and creep of Ni-Cr-Fe alloys in carburizing and oxidizing environments, *Oxid. Met.* 12(5) (1978) 387-404.
- [19] J. Chapovaloff, G. Girardin, D. Kaczorowski, K. Wolski, M. Pijolat, High temperature corrosion of the nickel-base alloy Inconel 617 in helium containing small amounts of impurities, (2007).
- [20] C. Jang, D. Lee, D. Kim, Oxidation behaviour of an Alloy 617 in very high-temperature air and helium environments, *Int. J. Pres. Ves. Pip.* 85(6) (2008) 368-377.
- [21] R. Viswanathan, J. Henry, J. Tanzosh, G. Stanko, J. Shingledecker, B. Vitalis, R. Purgert, US program on materials technology for ultra-supercritical coal power plants, *J. Mater. Eng. Perform.* 14(3) (2005) 281-292.

- [22] W. Mankins, J. Hosier, T. Bassford, Microstructure and phase stability of Inconel alloy 617, *Metallurgical Transactions* 5(12) (1974) 2579-2590.
- [23] O.F. Kimball, G.Y. Lai, G.H. Reynolds, Effects of thermal aging on the microstructure and mechanical properties of a commercial Ni-Cr-Co-Mo alloy (inconel 617), *Metall. Trans. A* 7(12) (1976) 1951-1952.
- [24] K. Maile, Qualification of Ni-based alloys for advanced ultra supercritical plants, *Procedia Eng.* 55 (2013) 214-220.
- [25] G.E. Dieter, *Mechanical Metallurgy*. 3rd, Edition Mc Graw Hill, NY (1986) 287-288.
- [26] F. Vogel, N. Wanderka, Z. Balogh, M. Ibrahim, P. Stender, G. Schmitz, J. Banhart, Mapping the evolution of hierarchical microstructures in a Ni-based superalloy, *Nat. Commun.* 4 (2013) 2955.
- [27] J. Radavich, W. Coutts, Effect of temperature exposure on the microstructure of 4.5 Al-3.5 Ti Nickel-base alloy, *Trans. ASM* 54 (1961) 591-597.
- [28] J.F. Radavich, W.H. Coutts Jr, *METALLOGRAPHY OF THE SUPERALLOYS*, Micro-Met Labs., West Lafayette, Ind., 1971.
- [29] G. Kegg, J. Silcock, The shape of M₂₃C₆ particles, *Scripta metall.* 6(11) (1972) 1083-1086.
- [30] H.-J. Christ, U. Künecke, K. Meyer, H. Sockel, High temperature corrosion of the nickel-based alloy Inconel 617 in helium containing small amounts of impurities, *Mat. Sci. Eng.* 87 (1987) 161-168.
- [31] L. Fan, L. Liu, Z. Yu, M. Cao, Y. Li, F. Wang, Corrosion Behavior of Ti60 Alloy under a Solid NaCl Deposit in Wet Oxygen Flow at 600 °C, *Sci. Rep.* 6 (2016) 29019.
- [32] H. Kokawa, M. Shimada, Y.S. Sato, Grain-boundary structure and precipitation in sensitized austenitic stainless steel, *JOM* 52(7) (2000) 34-37.

- [33] M.A. Streicher, General and Intergranular Corrosion of Austenitic Stainless Steels in Acids Effect of Cations in the Acids and the Influence of Heat Treatment and Grain Size of the Steel, *J. Electrochem. Soc.* 106(3) (1959) 161-180.
- [34] J. Klöwer, R. Husemann, M. Bader, Development of nickel alloys based on alloy 617 for components in 700 C power plants, *Procedia Eng.* 55 (2013) 226-231.
- [35] F. Abe, Research and Development of Heat-Resistant Materials for Advanced USC Power Plants with Steam Temperatures of 700 °C and Above, *Eng.* 1(2) (2015) 211-224.
- [36] S. CHETAL, T. JAYAKUMAR, A. BHADURI, Materials Research and Opportunities in Thermal (Coal-based) Power Sector Including Advanced Ultra Super Critical Power Plants, *Proc Indian Natn Sci Acad*, 2015, pp. 739-754.
- [37] T. Lillo, J. Cole, M. Frary, S. Schlegel, Influence of grain boundary character on creep void formation in alloy 617, *Metall. Mater. Trans. A* 40(12) (2009) 2803-2811.
- [38] W. Ren, R. Swindeman, A Review on Current Status of Alloys 617 and 230 for Gen IV Nuclear Reactor Internals and Heat Exchangers, *J. Pressure Vessel Technol.* 131(4) (2009) 044002-044002-15.
- [39] J. Wang, L. Zhou, L. Sheng, J. Guo, The microstructure evolution and its effect on the mechanical properties of a hot-corrosion resistant Ni-based superalloy during long-term thermal exposure, *Mater. Des.* 39 (2012) 55-62.
- [40] C. Jang, S.H. Kim, I. Sah, D. Kim, Creep behavior of Alloy 617 in high temperature air and helium environments—effect of oxidation damage, *J. Mech. Sci. Technol.* 30(10) (2016) 4433-4438.
- [41] S. Jahan, E. Jespersen, S. Mukherjee, M. Kovacevic, A. Bonini, C. Calderon, C. Cazabat, Y. Hsu, C. Lengfelder, S. Lucic, Human development report 2015: Work for human development, UNDP: New York, NY, USA (2015).

- [42] T. Sumner, Scientists confirm ‘greenhouse’ effect of human’s CO₂, Science News for Students (2015).
- [43] F.A. Gifford Jr, AN OUTLINE OF THEORIES OF DIFFUSION IN THE LOWER LAYERS OF THE ATMOSPHERE, Environmental Science Services Administration, Oak Ridge, Tenn.), 1968.
- [44] H. Riebeek, Global warming: Feature articles, (2010).
- [45] L. Antilla, Climate of scepticism: US newspaper coverage of the science of climate change, Global Environ. Chang. 15(4) (2005) 338-352.
- [46] U. Olausson, Global warming—global responsibility? Media frames of collective action and scientific certainty, Public Understanding of Science (2009).
- [47] S. Allan, Media, risk and science, Order 9 (2002) 235.
- [48] R. Viswanathan, R. Purgert, U. Rao, Materials for Advanced Power Engineering 2002, Proceedings Part II, Forschungszentrum Julich GmbH (2002) 1109-1129.
- [49] J. Shingledecker, J. Phillips, US Department of Energy and Ohio Coal Development Office Advanced Ultra-Supercritical Materials Project for Boilers and Steam Turbines—Summary of Results, EPRI report (1022770) (2011).
- [50] R. Blum, R. Vanstone, Materials development for boilers and steam turbines operating at 700 DGC, PARSONS 2003: Sixth International Charles Parsons Turbine Conference, 2003, pp. 489-510.
- [51] N. Bhatt, M. Batrani, J. Mohan, V. Gopalakrishnan, M. Verma, Indian AUSC Steam Turbine Program—Current Status and Future Program, Int. J. Eng. Res. Technol., IJERT, 2015.
- [52] J. Hosier, D. Tillack, INCONEL alloy 617: a new high-temperature alloy, Metals Eng. Quart 12(3) (1972) 51-55.

- [53] H. Kirchhöfer, F. Schubert, H. Nickel, Precipitation behavior of Ni-Cr-22 Fe-18 Mo (Hastelloy-X) and Ni-Cr-22 Co-12 Mo (Inconel-617) after isothermal aging, Nucl. Technol. 66(1) (1984) 139-148.
- [54] S. Kihara, J.B. Newkirk, A. Ohtomo, Y. Saiga, Morphological changes of carbides during creep and their effects on the creep properties of Inconel 617 at 1000 C, Metall. Trans. A 11(6) (1980) 1019-1031.
- [55] R.K. Nanstad, M.A. Sokolov, X. Chen, Fracture Toughness of 9Cr-1 MoV and Thermally Aged Alloy 617 for Advanced Reactor Applications, Energy Technology 2012, John Wiley & Sons, Inc.2012, pp. 341-356.
- [56] K. Krompholz, E. Grosser, K. Ewert, Determination of J - integral R - curves for Hastelloy X and inconel 617 up to 1223 K using the potential drop technique, Materialwissenschaft und Werkstofftechnik 13(7) (1982) 236-244.
- [57] T. Murakumo, T. Kobayashi, Y. Koizumi, H. Harada, Creep behaviour of Ni-base single-crystal superalloys with various γ' volume fraction, Acta metall. 52(12) (2004) 3737-3744.
- [58] H. Harada, M. Yamazaki, Y. Koizumi, N. Sakuma, N. Furuya, H. Kamiya, High temperature alloys for gas turbines 1982, Proc. of a Conference, Liege, 1982, p. 721.
- [59] X. Wang, J. Liu, T. Jin, X. Sun, Z. Hu, J. Do, B. Choi, I. Kim, C. Jo, Effects of Temperature and Stress on Microstructural Evolution during Creep Deformation of Ru - free and Ru - containing Single Crystal Superalloys, Adv. Eng. Mater. 17(7) (2015) 1034-1044.
- [60] J. Benz, T. Lillo, R. Wright, Aging of Alloy 617 at 650 and 750 C, Report INL/EXT-12-27974, 2013.
- [61] Y. Guo, B. Wang, S. Hou, Aging precipitation behavior and mechanical properties of Inconel 617 superalloy, Acta Metall. Sin.-Engl. 26(3) (2013) 307-312.

- [62] S. Schlegel, S. Hopkins, E. Young, J. Cole, T. Lillo, M. Frary, Precipitate redistribution during creep of alloy 617, *Metall. Mater. Trans. A* 40(12) (2009) 2812.
- [63] H. Roth, C. Davis, R. Thomson, Modeling solid solution strengthening in nickel alloys, *Metall. Mater. Trans. A* 28(6) (1997) 1329-1335.
- [64] J. Rösler, M. Götting, D. Del Genovese, B. Böttger, R. Kopp, M. Wolske, F. Schubert, H.J. Penkalla, T.s. Seliga, A. Thoma, Wrought Ni - Base Superalloys for Steam Turbine Applications beyond 700° C, *Adv. Eng. Mater.* 5(7) (2003) 469-483.
- [65] T. Murakumo, Y. Koizumi, K. Kobayashi, H. Harada, Creep strength of Ni-base single-crystal superalloys on the γ/γ' -tie-line, *Superalloys* (2004) 155-62.
- [66] R. Bowman, *Superalloys: A primer and history*, 9th International Symposium on superalloys, 2000.
- [67] C.-C. Hsieh, W. Wu, Overview of Intermetallic Sigma () Phase Precipitation in Stainless Steels, *ISRN Metallurgy* 2012 (2012) 16.
- [68] L.B. Moura, R.F. Guimarães, H.F.G.d. Abreu, H.C.d. Miranda, S.S.M. Tavares, Naphthenic corrosion resistance, mechanical properties and microstructure evolution of experimental Cr-Mo steels with high Mo content, *Mat. Res.* 15 (2012) 277-284.
- [69] L.B. Moura, H.F.G. de Abreu, Y.S. Negreiros, Computational thermodynamic analysis of secondary phases in super ferritic stainless steels, *J. Mater. Res. Technol.* 2(3) (2013) 282-287.
- [70] H. Numakura, T. Ikeda, M. Koiwa, A. Almazouzi, Self-diffusion mechanism in Ni-based L12 type intermetallic compounds, *Philos. Mag.* 77(4) (1998) 887-909.
- [71] Q. Wu, H. Song, R.W. Swindeman, J.P. Shingledecker, V.K. Vasudevan, Microstructure of Long-Term Aged IN617 Ni-Base Superalloy, *Metall. Mater. Trans. A* 39(11) (2008) 2569-2585.
- [72] R.F. Decker, *Strengthening mechanisms in nickel-base superalloys*, International Nickel, New York, 1969.

- [73] ASTM E8/E8M-16a, Standard Test Methods for Tension Testing of Metallic Materials, ASTM International, West Conshohocken, PA, 2016.
- [74] ASTM E-23-16b, Standard Test Methods for Notched Bar Impact Testing of Metallic Materials, ASTM International, West Conshohocken, PA, 2016.
- [75] J. Goldstein, D.E. Newbury, P. Echlin, D.C. Joy, A.D. Romig Jr, C.E. Lyman, C. Fiori, E. Lifshin, Scanning electron microscopy and X-ray microanalysis: a text for biologists, materials scientists, and geologists, Springer Science & Business Media 2012.
- [76] D.B. Williams, C.B. Carter, Transmission electron microscopy: a textbook for materials science. 2009, Springer.
- [77] J. Edwards, Hardness Testing, Characterization of Materials, John Wiley & Sons, Inc. 2002.
- [78] L. Prandtl, Über die härte plastischer körper, Nachrichten von der Gesellschaft der Wissenschaften zu Göttingen, Mathematisch-Physikalische Klasse 1920 (1920) 74-85.
- [79] L. Toth, H.-P. Rossmanith, T. Siewert, Historical background and development of the Charpy test, European Structural Integrity Society 30 (2002) 3-19.
- [80] D. François, A. Pineau, From Charpy to present impact testing, Elsevier 2002.
- [81] F. Weinberg, Grain boundaries in metals, Prog. Metal Phys. 8 (1959) 105-146.
- [82] T. Horiuchi, N. Satoh, Relationship between Duplex Grain Structure and Grain-boundary Precipitates in Ni₂M-stabilized Alloy, e-J. Adv. Maint. 5(3) (2013) 165-174.
- [83] D. Collins, B. Conduit, H. Stone, M. Hardy, G. Conduit, R. Mitchell, Grain growth behaviour during near- γ' solvus thermal exposures in a polycrystalline nickel-base superalloy, Acta metall. 61(9) (2013) 3378-3391.
- [84] K. Hrutkay, Evolution of Microstructure of Haynes 230 and Inconel 617 Under Mechanical Testing At High Temperatures, Nuclear Engineering, University of South Carolina, 2013.

- [85] H. Hong, I. Kim, B. Choi, Y. Yoo, C. Jo, On the mechanism of serrated grain boundary formation in Ni-based superalloys with low γ' volume fraction, *Superalloys* (2012) 53-61.
- [86] M. Henry, Y. Yoo, D. Yoon, J. Choi, The dendritic growth of γ' precipitates and grain, *Metall. Trans. A* 24(8) (1993) 1733-1743.
- [87] R. Mitchell, H. Li, Z. Huang, On the formation of serrated grain boundaries and fan type structures in an advanced polycrystalline nickel-base superalloy, *J. Mater. Process. Tech.* 209(2) (2009) 1011-1017.
- [88] A.K. Koul, R. Thamburaj, Serrated grain boundary formation potential of Ni-based superalloys and its implications, *Metall. Trans. A* 16(1) (1985) 17-26.
- [89] S.F. Di Martino, R.G. Faulkner, S.C. Hogg, S. Vujic, O. Tassa, Characterisation of microstructure and creep properties of alloy 617 for high-temperature applications, *Mater. Sci. Eng. A* 619 (2014) 77-86.
- [90] Z. Shi, X. Wang, S. Liu, J. Li, Low cycle fatigue properties and microstructure evolution at 760°C of a single crystal superalloy, *Pro. Nat. Sci.-Mater.* 25(1) (2015) 78-83.
- [91] X.-C. Chen, C.-B. Shi, H.-J. Guo, F. Wang, H. Ren, D. Feng, Investigation of Oxide Inclusions and Primary Carbonitrides in Inconel 718 Superalloy Refined through Electroslag Remelting Process, *Metall. Mater. Trans. B* 43(6) (2012) 1596-1607.
- [92] W. Xu, Z. Li, H. Yuan, G. Zhang, Effect of second phase on grain growth of spray formed superalloy GH742y, *Rare Metals* 30 (2011) 392-395.
- [93] T. Tokunaga, K. Nishio, H. Ohtani, M. Hasebe, Phase equilibria in the Ni-Si-B system, *Mater. Trans.* 44(9) (2003) 1651-1654.
- [94] J.R. Davis, *ASM specialty handbook: heat-resistant materials*, Asm International 1997.

- [95] C.M. Kuo, Y.T. Yang, H.Y. Bor, C.N. Wei, C.C. Tai, Aging effects on the microstructure and creep behavior of Inconel 718 superalloy, *Mater. Sci. Eng. A* 510-511 (2009) 289-294.
- [96] A.N. Singh, A. Moitra, P. Bhaskar, G. Sasikala, A. Dasgupta, A.K. Bhaduri, Study of Aging-Induced Degradation of Fracture Resistance of Alloy 617 Toward High-Temperature Applications, *Metall. Mater. Trans. A* 48(7) (2017) 3269-3278.
- [97] A.N. Singh, A. Moitra, P. Bhaskar, A. Dasgupta, G. Sasikala, A.K. Bhaduri, A Study of Tensile Flow and Work-Hardening Behavior of Alloy 617, *J. Mater. Eng. Perform.* (2018).
- [98] R. Krishna, H.V. Atkinson, S.V. Hainsworth, S.P. Gill, Gamma Prime Precipitation, Dislocation Densities, and TiN in Creep-Exposed Inconel 617 Alloy, *Metall. Mater. Trans. A* 47(1) (2016) 178-193.
- [99] T. Smith, B. Esser, N. Antolin, A. Carlsson, R. Williams, A. Wessman, T. Hanlon, H. Fraser, W. Windl, D. McComb, Phase transformation strengthening of high-temperature superalloys, *Nat. Commun.* 7 (2016).
- [100] M.H. Yoo, C.L. Fu, J.A. Horton, Crack-tip dislocations and fracture behavior in Ni₃Al and Ni₃Si, *Mater. Sci. Eng. A* 176(1) (1994) 431-437.
- [101] K. Mo, G. Lovicu, H.-M. Tung, X. Chen, J.F. Stubbins, High Temperature Aging and Corrosion Study on Alloy 617 and Alloy 230, *J. Eng. Gas. Turb. Power.* 133(5) (2010) 052908-052908-9.
- [102] X. Liu, K. Mo, Y. Miao, K.-C. Lan, G. Zhang, W.-Y. Chen, C. Tomchik, R. Seibert, J. Terry, J.F. Stubbins, Investigation of thermal aging effects on the tensile properties of Alloy 617 by in-situ synchrotron wide-angle X-ray scattering, *Mater. Sci. Eng. A* 651 (2016) 55-62.
- [103] G.E. Dieter, D.J. Bacon, *Mechanical metallurgy*, McGraw-Hill New York 1986.

- [104] F. Pettinari, J. Douin, G. Saada, P. Caron, A. Coujou, N. Clement, Stacking fault energy in short-range ordered γ -phases of Ni-based superalloys, *Mater. Sci. Eng. A* 325(1-2) (2002) 511-519.
- [105] C. Cui, C. Tian, Y. Zhou, T. Jin, X. Sun, Dynamic strain aging in Ni base alloys with different stacking fault energy, *Superalloys 2012*, TMS Seven Springs (PA, USA)2012, pp. 715-722.
- [106] C. Wang, C.-Y. Wang, Density functional theory study of Ni/Ni₃Al interface alloying with Re and Ru, *Surf. Sci.* 602(14) (2008) 2604-2609.
- [107] L. Tan, K. Sridharan, T.R. Allen, Effect of thermomechanical processing on grain boundary character distribution of a Ni-based superalloy, *J. Nucl. Mater.* 371(1-3) (2007) 171-175.
- [108] A.K. Roy, V. Marthandam, Mechanism of yield strength anomaly of Alloy 617, *Mater. Sci. Eng. A* 517(1) (2009) 276-280.
- [109] C. Wang, Y. Guo, J. Guo, L. Zhou, Microstructural changes and their effect on tensile properties of a Ni-Fe based alloy during long-term thermal exposure, *Mater. Sci. Eng. A* 670 (2016) 178-187.
- [110] J.H. Hollomon, Tensile deformation, *AIME TRANS* 12(4) (1945) 1-22.
- [111] P. Ludwik, *Elemente der Technologischen Mechanik*. Verlag von Julius Springer, Berlin, 1909, p. 32.
- [112] H.W. Swift, Plastic instability under plane stress, *J. Mech. Phys. Solids* 1(1) (1952) 1-18.
- [113] D. Ludwigson, Modified stress-strain relation for FCC metals and alloys, *Metall. Trans.* 2(10) (1971) 2825-2828.
- [114] E. Voce, A practical strain-hardening function, *Metall.* 51(307) (1955) 219-226.
- [115] E. Voce, The relationship between stress and strain for homogeneous deformation, *J Inst Met* 74 (1948) 537-562.

- [116] Y. Bard, Comparison of gradient methods for the solution of nonlinear parameter estimation problems, *SIAM J. Numer. Anal.* 7(1) (1970) 157-186.
- [117] K.M. Brown, J.E. Dennis, Derivative free analogues of the Levenberg-Marquardt and Gauss algorithms for nonlinear least squares approximation, *Numer. Math.* 18(4) (1971) 289-297.
- [118] M.L. McHugh, The Chi-square test of independence, *Biochem. Medica* 23(2) (2013) 143-149.
- [119] A. Lavakumar, C.V.S. Murthy, D.V.V. Satyanarayana, R. Chakravorty, N.E. Prasad, Strain hardening behaviour of a Nickel based superalloy SUPERCAST 247A, *Int. J. Sci. Eng. Res.* 4(8) (2013) 1914-1920.
- [120] J. Christopher, B. Choudhary, E.I. Samuel, V. Srinivasan, M. Mathew, Tensile flow and work hardening behaviour of 9Cr–1Mo ferritic steel in the frame work of Voce relationship, *Mater. Sci. Eng. A* 528(21) (2011) 6589-6595.
- [121] P. Singh, V. Singh, Influence of ageing treatment on work hardening behaviour of a Ni-base superalloy, *Scripta Mater.* 34(12) (1996) 1861-1865.
- [122] B. Choudhary, D.P.R. Palaparti, E.I. Samuel, Analysis of tensile stress-strain and work-hardening behavior in 9Cr-1Mo ferritic steel, *Metall. Mater. Trans. A* (2012) 1-12.
- [123] K. Praveen, G. Sastry, V. Singh, Work-hardening behavior of the Ni-Fe based superalloy IN718, *Metall. Mater. Trans. A* 39(1) (2008) 65-78.
- [124] A. Soussan, S. Degallaix, T. Magnin, Work-hardening behaviour of nitrogen-alloyed austenitic stainless steels, *Mater. Sci. Eng. A* 142(2) (1991) 169-176.
- [125] R. Reed-Hill, W. Cribb, S. Monteiro, Concerning the analysis of tensile stress-strain data using $\log d\sigma/d\epsilon$ versus $\log \sigma$ diagrams, *Metall. Mater. Trans. B* 4(11) (1973) 2665-2667.

- [126] U. Kocks, R. Cook, R. Mulford, Strain aging and strain hardening in Ni · C alloys, *Acta Metall.* 33(4) (1985) 623-638.
- [127] E. El-Danaf, S.R. Kalidindi, R.D. Doherty, Influence of grain size and stacking-fault energy on deformation twinning in fcc metals, *Metall. Mater. Trans. A* 30(5) (1999) 1223-1233.
- [128] A.W. Thompson, Work hardening in tension and fatigue, AIME, New York (1977) 89-126.
- [129] E. Orowan, Problems of plastic gliding, *Proceedings of the Physical Society* 52(1) (1940) 8.
- [130] M. Farooq, Strengthening and degradation mechanisms in austenitic stainless steels at elevated temperature, KTH Royal Institute of Technology, Stockholm, 2013, pp. ix, 56.
- [131] M. Zain-ul-abdein, D. Nélias, Effect of coherent and incoherent precipitates upon the stress and strain fields of 6xxx aluminium alloys: a numerical analysis, *Int. J. Mech. Mater. Des.* 12(2) (2016) 255-271.
- [132] G. Marchese, G. Basile, E. Bassini, A. Aversa, M. Lombardi, D. Ugues, P. Fino, S. Biamino, Study of the Microstructure and Cracking Mechanisms of Hastelloy X Produced by Laser Powder Bed Fusion, *Materials* 11(1) (2018) 106.
- [133] N.J. Harrison, I. Todd, K. Mumtaz, Reduction of micro-cracking in nickel superalloys processed by Selective Laser Melting: A fundamental alloy design approach, *Acta metall.* 94 (2015) 59-68.
- [134] E. Welsch, D. Ponge, S.H. Haghighat, S. Sandlöbes, P. Choi, M. Herbig, S. Zaefferer, D. Raabe, Strain hardening by dynamic slip band refinement in a high-Mn lightweight steel, *Acta metall.* 116 (2016) 188-199.

- [135] L. Bo, Q.-l. Pan, C.-p. Chen, Z.-m. Yin, Effect of aging time on precipitation behavior, mechanical and corrosion properties of a novel Al-Zn-Mg-Sc-Zr alloy, *T. Nonferr. Metal Soc.* 26(9) (2016) 2263-2275.
- [136] V.M. Nangare, V. Nandedkar, Effect of Aging Time and Aging Temperature on Mechanical Properties of 333 Aluminum alloy by Neural Network and Response Surface Methodology, *Mater. Today Proc.* 4(2) (2017) 1874-1882.
- [137] C. Beachem, A new model for hydrogen-assisted cracking (hydrogen “embrittlement”), *Metall. Mater. Trans. B* 3(2) (1972) 441-455.
- [138] I. Robertson, H. Birnbaum, An HVEM study of hydrogen effects on the deformation and fracture of nickel, *Acta Metall.* 34(3) (1986) 353-366.
- [139] R. Oriani, Whitney award lecture—1987: hydrogen—the versatile embrittler, *Corros.* 43(7) (1987) 390-397.
- [140] K. Mo, G. Lovicu, H.-M. Tung, X. Chen, J.F. Stubbins, High temperature aging and corrosion study on alloy 617 and alloy 230, *J. Eng. Gas Turb. Power* 133(5) (2011) 052908.
- [141] S. Panin, P. Maruschak, I. Vlasov, D. Moiseenko, F. Berto, R. Bishchak, A. Vinogradov, The role of notch tip shape and radius on deformation mechanisms of 12Cr1MoV steel under impact loading. Part 1. Energy parameters of fracture, Fatigue. *Fract. Eng. M.* 40(4) (2017) 586-596.
- [142] K. Toshiro, Y. Isamu, N. Mitsuo, Evaluation of dynamic fracture toughness parameters by instrumented Charpy impact test, *Eng. Fract. Mech.* 24(5) (1986) 773-782.
- [143] A.N. Singh, A. Moitra, P. Bhaskar, G. Sasikala, A. Dasgupta, A.K. Bhaduri, Effect of thermal aging on microstructure, hardness, tensile and impact properties of Alloy 617, *Mater. Sci. Eng. A* 710 (2018) 47-56.

- [144] M. Sundararaman, The Role of Refractory Metal Additions in Precipitation Processes in Superalloys, *Min. Proc. Ext. Met. Rev.* 22(2) (2001) 681-700.
- [145] J. Yang, Y. He, C. Qin, W. Zhao, S. Chen, Z. Gao, Microstructure evolution in a Ni–Mo–Cr superalloy subjected to simulated heat-affected zone thermal cycle with high peak temperature, *Mater. Des.* 86 (2015) 230-236.
- [146] W.D. Callister Jr, D.G. Rethwisch, *Fundamentals of materials science and engineering: an integrated approach*, John Wiley & Sons 2012.
- [147] A. Baldan, Review Progress in Ostwald ripening theories and their applications to nickel-base superalloys Part I: Ostwald ripening theories, *J. Mater. Sci.* 37(11) (2002) 2171-2202.
- [148] A. Goodfellow, Strengthening mechanisms in polycrystalline nickel-based superalloys, *Mater. Sci. Technol.* 34(15) (2018) 1793-1808.
- [149] S.N. Gurugubelli, The effect of ageing on impact toughness and microstructure of 2024 Al–Cu–Mg alloy, *World Acad. Sci., Eng. Technol* 62 (2012) 648-650.
- [150] R.E. Smallman, A.H.W. Ngan, Chapter 13 - Precipitation Hardening, in: R.E. Smallman, A.H.W. Ngan (Eds.), *Modern Physical Metallurgy* (Eighth Edition), Butterworth-Heinemann, Oxford, 2014, pp. 499-527.
- [151] R.L. Jones, J.R. Gordon, N.V. Challenger, A STUDY OF SPECIMEN SIZE ON J - R CURVE BEHAVIOUR, *Fatigue. Fract. Eng. M.* 14(7) (1991) 777-788.
- [152] H.J. Schindler, Estimation of the dynamic JR-curve from a single impact bending test.
- [153] T.A. Siewert, M.P. Manahan, *Pendulum impact testing: a century of progress*, ASTM, 2000.
- [154] H. Schindler, P. Bertschinger, S. Vodenicharov, *Scaling of Charpy Fracture Energy with Specimen Size*, ECF14, Cracow 2002.

- [155] S. Sathyanarayanan, G. Sasikala, S.K. Ray, Evaluation of dynamic fracture toughness of cold worked 9Cr–1Mo steel, *Int. J. Pres. Ves. Pip.* 81(5) (2004) 419-425.
- [156] W.L. Server, Instrumented Charpy test review and application to structural integrity, European Structural Integrity Society, Elsevier 2002, pp. 205-212.
- [157] S. ASTM, ASTM E2298-18, Standard Test Method for Instrumented Impact Testing of Metallic Materials, ASTM International, West Conshohocken, PA, 2018, www.astm.org, 2015, p. 9.
- [158] Ž. Alar, D. Mandić, A. Dugorepec, M. Sakoman, Application of Instrumented Charpy Method in Characterisation of Materials, *Interdisciplinary Description of Complex Systems: INDECS* 13(3) (2015) 479-487.
- [159] W. Poole, D. Lloyd, J. Embury, The effect of natural ageing on the evolution of yield strength during artificial ageing for Al-Mg-Si-Cu alloys, *Mater. Sci. Eng. A* 234 (1997) 306-309.